High resolution tidal models for the Norwegian coast

Birgit Kjoss Lynge

Thesis submitted for the degree of Ph.D.

Department of Mathematics
University of Oslo

February 2011

Series of dissertations submitted to the
Faculty of Mathematics and Natural Sciences, University of Oslo
No. 1076

ISSN 1501-7710

Cover: Inger Sandved Anfinsen.
Printed in Norway: AIT Oslo AS.

Produced in co-operation with Unipub.
The thesis is produced by Unipub merely in connection with the
thesis defence. Kindly direct all inquiries regarding the thesis to the copyright
holder or the unit which grants the doctorate.

I must down to the seas again, for the call of the running tide
Is a wild call and a clear call that may not be denied

From *Sea-Fever* by John Masefield

Preface

This thesis is submitted in partial fulfillment of the degree of *philosophiae doctor* (Ph.D.) at the University of Oslo. The work done for the thesis has mainly been performed during the period from November 2007 to February 2011.

The work with the Ph.D has been part of the research project *Nonlinear wind waves, their modifications by tidal currents, and application to Norwegian waters*. The project is funded by the Research Council of Norway and headed by Professor Karsten Trulsen. One year of my work with the thesis has been funded by this project. The remaining funding has come from the Norwegian Hydrographic Service where I am employed. The work presented in the thesis has been carried out in collaboration with my main supervisor Bjørn Gjevik, my co-supervisor Jarle Berntsen, and Ph.D-student Karina B. Hjelmervik. Also colleagues at the Norwegian Hydrographic Service has contributed to the work with the thesis. The thesis consist of four papers. At the time of writing two of the papers are published. One of the papers are planed published in close future, and the last one is a technical report. My contributions to the papers will be listed in the Introduction.

Stavanger, February 2011
Birgit Kjoss Lynge

Acknowledgments

During the last three years I have had the privilege to work with my Ph.D. thesis at the Department of Mathematics (University of Oslo) in close cooperation with my supervisor Professor Bjørn Gjevik. I would like to thank him for his invaluable help and support. He has always had time for my questions and discussions, and with his deep insight and great enthusiasm he has inspired and navigated me safely through my thesis. Without his contacts and cooperation with the Norwegian Hydrographic Service during many years in advance there would have been no thesis.

I would also like to express my gratitude to my co-supervisor Professor Jarle Berntsen at the University in Bergen for his solid guidance, and for invaluable help and support with the three dimensional σ-coordinate model. I am also very grateful for the good cooperation and constructive iterations to the paper on relative dispersion included in this thesis.

Further I would like to thank my colleagues at the University of Oslo (UiO). In particular I would like to thank Karina B. Hjelmervik for good cooperation and support, and Odin Gramstad, Huiming Zeng, and Farah Ali for support and discussions during courses and lunch breaks.

My gratitude also goes to the Norwegian Hydrographic Service (NHS) who together with UiO made it possible for me to complete this work. I would like to thank my colleagues in NHS, and in particular thanks to Noralf Slotsvik for never giving up the idea of doing tidal modeling in NHS. His believe in the future of tidal modeling as a tool to make current information available for navigational purposes made the work with this thesis possible. I would also in particular like to thank Tor Tørresen and Daniel Hareide for insight and guidance in the *world of tides* and for cooperation with field measurements and analyses applied in this thesis.

I am also grateful to the Institute of Marine Research for letting us participate on a survey in the Lofoten area with the research vessel G.O. Sars in March 2009. I learned a lot from the survey and made valuable current measurements for my thesis. A particular thanks to the crew on G.O. Sars, and to Henrik Søiland, Kjell Arne Mork, and Asgeir Steinsland for help and instructions of instruments.

I would also like to thank all my friends who have followed me through and cheered me. Finally I would like to thank my parents and my family who always have encouraged me for education and studies and for their support and believe in me. In particular thanks to my husband and best friend Øystein who encourage me, gives me of his goodness and love, and is my everyday support.

Contents

Introduction

Tidal currents, particularly along the western and northern sections of the Norwegian coast, constitute by far the most important part of the total current variability. In narrow sounds and inlets to large fjord basins the tidal current can be very strong. Current speed up to 5 -10 ms^{-1} (10 -20 knots) are for example reported in the famous Saltstraumen near Bodø in the northern Norway. Strong currents are also observed in Moskstraumen outside the Lofoten headland. The latter is an unique case because the strong current appear off a headland surrounded by the open ocean (Gjevik *et al.*, 1997). The area is exposed to high ocean waves and their interactions with the tidal current is known to generate extremely dangerous wave conditions.

The Norwegian coast contains numerous shallow and narrow sounds where strong tidal current may occur. Extreme current conditions may occur during storm surges when the surge driven current interacts with the tide. Since the coastal ship traffic and the fishing fleet often have to cross exposed areas with strong tidal currents it represent a considerable safety hazard. Therefore it is important to be able to predict and monitor current and waves in the sailing lanes along the Norwegian coast. The strong tidal currents also have a crucial effect on the drift and dispersion and pollutants in coastal waters. From an environmental point of view a better knowledge of the dynamics of the tidal currents and spatial structures of the velocity field is therefore beneficial for several purposes.

Mappings of tidal current in Norwegian coastal areas were executed by the Norwegian Hydrographic Service (NHS) during the 70‘s and 90‘s, but the field campaigns were ended due to economical reasons. The measurements were executed at fixed locations far apart, and thereby do not reveal the small scale horizontal structures of the current field. Mapping of the current in narrow sailing lanes has been of interest for decades, and were also made along the Norwegian coast by the Germans during the second World War (Fig. 1).

Mapping the current field by numerical models reveals the horizontal structures of the flow field. Current fields predicted with a reasonable accuracy may improve the safety of sailing in coastal areas and reduce risk for ship collisions and groundings. Mapping of tidal current for navigational purposes has recently been demonstrated (Gjevik *et al.*, 2006). The paper demonstrate how predicted high resolution tidal current fields can be displayed in real time on modern electronic navigational charts, and thereby become a useful tool for navigators. The paper is included in this thesis. Another example on an application for displaying tidal current for navigational purposes is given in (Hjelmervik *et al.*, 2009). The Royal Norwegian Navy has used simulated tidal current data for exercises in the area of Tjeldsundet in northern Norway. Model simulations of the currents are important information during exercise and also vital information in preparation of safe maritime operations.

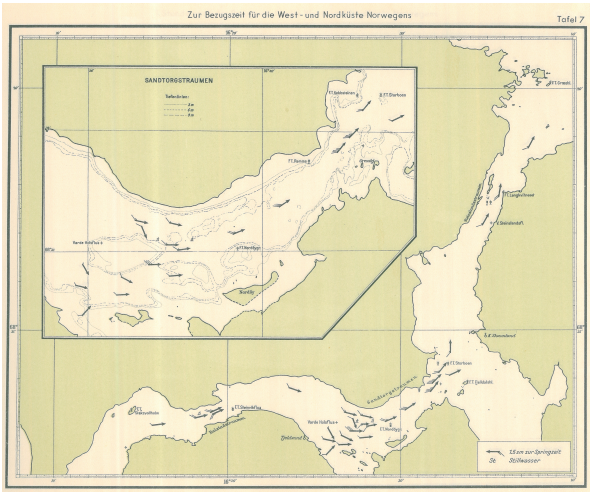

Figure 1: *During the second World War the Germans made tidal current maps for the western and northern coast of Norway. The figure shows tidal current through the Tjeldsund channel and Sandtorgstraumen at time of high water (Marineobservatorium, 1943).*

Tidal modeling

Tides is a unique oceanographic phenomenon in the sense that the tidal motion can be predicted with a high degree of accuracy long time ahead. The art of tidal prediction is based on the knowledge of the harmonic constants of the tidal oscillations and the astronomical arguments, i.e. the position of the Sun and the Moon. The harmonic constants can be determined by harmonic analysis of long records of sea level or current obtained either by field observations or by numerical modeling (Foreman, 1978).

For prediction of the deep ocean tides several global tidal models have been developed, see e.g. Schwiderski (1980), Le Provost *et al.* (1994), and Andersen (1995). Andersen *et al.* (1995) gives a comparison of the "state of the art" within ocean tide models, and an accuracy assessment of ocean tide models is found in Schum *et al.* (1997). In the late 1970s the most accurate ocean tide model was that of Schwiderski (1980), who constructed a hydrodynamic interpolation scheme for the assimilation of the tidal constant data set derived from the global collection of tide gauge data. Satellite altimetry from e.g. Geosat, TOPEX/POSEIDON, and ERS 1 enabled the study of the deep ocean tides with data assimilation from altimetry data to improve accuracy of the models. The TOPEX/POSEIDON satellite mission was, among other purposes, designed specifically to enable development of new global models. More recent and upgraded versions of global tidal models are found in e.g. Ray (1999) and Lefevre *et al.* (2002).

Tidal modeling in coastal waters is a well known subject worldwide and basic techniques are well established (Davies *et al.*, 1997*a*,*b*, and references therein). The increase in computer power and available high resolution bottom topography enable us to make tidal prediction with high horizontal resolution with improved accuracy. This means that today the tidal current can be simulated by numerical models with the necessary resolution to provide useful information for navigation and marine operations in narrow coastal waters with complex bottom topography and coastlines (Moe *et al.*, 2002, 2003, Gjevik *et al.*, 2006, Hjelmervik *et al.*, 2005, 2009).

For accurate model prediction a detailed depth matrix with high spatial resolution is required in shallow areas with complex bottom topography and a irregular coastal geometry. For the experiments carried out for this thesis the Norwegian Hydrographic Service (NHS) provides us

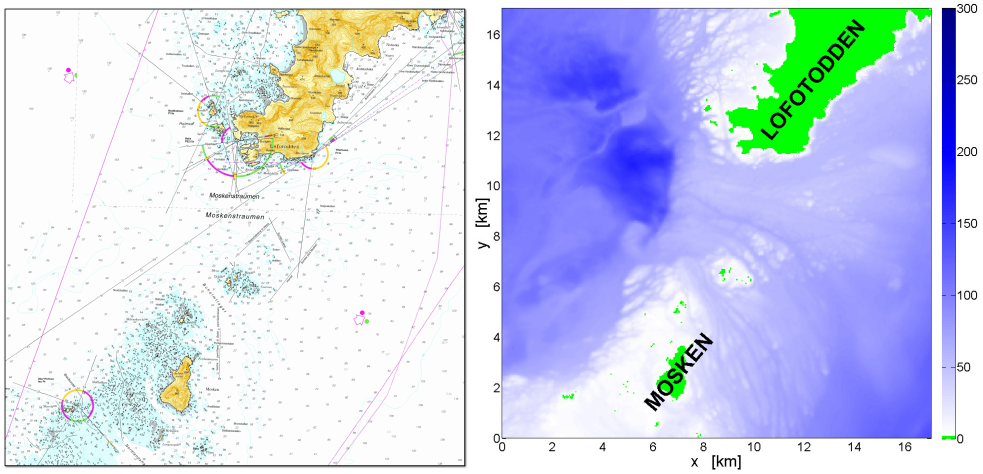

Figure 2: *Left: The navigational sea map for the area off the Lofoten headland in northern Norway. The island Mosken surrounded by numerous small islands and skerries is shown in the lower left corner. Right: The corresponding depth matrix with 50 m spatial resolution.*

with high resolution bottom topography with 50 m horizontal grid resolution. With a horizontal resolution of 50 m we are able to resolve much of the fine scale details of the topography, but in some areas we are still not able to resolve all the small scale details of the topography which can be of importance for the structures of the flow field. Fig. 2 shows the sea map from the area off the Lofoten headland and the corresponding depth matrix with 50 m equidistant horizontal resolution. The figures show that the main features of the bottom topography are resolved by the depth matrix, but the numerous small islands west and north of Mosken, and some skerries and shallow rocks remain unresolved in the depth matrix.

Numerical models for predictions of ocean and coastal flow have been studied extensively and different techniques and methods are developed. For dicretization of the hydrodynamic equations the finite difference and finite volume methods have been widely used. The finite difference method has its advantage in simple code structure and computational efficiency, but has its limitation in accurately fitting irregular coastal geometry. The finite volume method has its advantage in geometric flexibility. A comparison of a finite volume approach for coastal ocean circulation with finite difference models is recently given in Chen *et al.* (2007) were an unstructured grid was applied for the finite volume model. Unstructured grid has also recently been used in Davies *et al.* (2010) where the parameterising of small-scale processes in oceanographic models and the extent to which small-scale effects influence the larger scale is discussed.

For this thesis two numerical models using the finite difference method have been applied for tidal simulations, i.e. the depth integrate model developed at the University of Oslo (UiO) (Gjevik *et al.*, 1997; Moe *et al.*, 2002; Hjelmervik *et al.*, 2005) and the Bergen Ocean Model (BOM) (Berntsen, 2004; Berntsen *et al.*, 2008, 2009). The tidal models are described in details in the papers.

Contributions to the thesis

The main body of this thesis consists of four separate research contributions. Accurate model prediction of the tidal current for navigational purposes has been the main motivation. Another motivation is to provide information about the spatial structures of the tidal flow field for environmental purposes such as i.e. fish farming, dispersion and transports of oil spill, and dispersion of sea lice and pollutants. The two tidal models have been applied in shallow areas with complex bottom topography and with strong current with complex current fields. In the following I will summarize the motivation behind the different parts, the outline for the different parts, and my contributions.

Paper I – Implementation of high resolution tidal current fields in electronic navigational chart systems

The first paper (Gjevik *et al.*, 2006) published in Marine Geodesy, presents a system for displaying tidal currents in real time in an electronic chart display and information system (ECDIS). An application example of the implementation was given for Trondheimsleia, a part of the main sailing route along the western coast of Norway. The demonstrator was developed by UiO and NHS in cooperation with C-Map Norway (now Jeppesen Norway AS). The depth integrated tidal model (UiO) discretized on a 50 and 100 m horizontal grid was used for predictions of the tidal flow. Sea level and current measurements were deployed for validation of the numerical model. The depth matrix for the central part of the model domain was calculated from data from multibeam bathymetric surveys. Data for the depth matrix was processed and provided from the NHS.

The relative new technology of electronic chart systems enable us to distribute important information for navigational purposes to improve safety for the sailing lanes. In the ECDIS it is possible to include time variable navigational objects representing the dynamic variability of the elements surrounding the ships. These objects are known under the term Marine Information Objects (MIOs). Tidal information can be one example on a MIO. The main motivation for this paper was to make a demonstrator to make tidal current information available for navigational purposes for one of the main sailing lanes for the ship traffic along the Norwegian coast. The paper has been a motivation for the further contributions to this thesis on studies and experiments of tidal and storm surge modeling.

For this paper I have contributed to the writing of sec. 4 and 6 together with Daniel Hareide with inputs from J.H. Skailand and H.B. Urheim. I have mainly been writing sec. 6 about ECDIS, MIOs, and implementation of tidal current in ECDIS, and contributed to sec. 4 about the depth matrix. I have also contributed to the sea level measurements used for validation of the numerical model. I took part in the field work where five temporary tide gauges where deployed at five different locations in Trondheimsleia, and I participated to the analyses of the time series of the sea level measurements. Details about the measurements and results from the harmonic analyses of the data are reported in Hareide & Lynge (2002).

Paper II – Strom surge and tidal interaction in the Tjeldsund channel, northern Norway

In the second paper (Lynge *et al.*, 2011) we study the combined effect of tidal current and storm surge current in the narrow and shallow Tjeldsund channel in northern Norway. The tide-surge interaction mechanism during two storm surge events in December 2004 has been studied. For the experiments the depth integrated UiO model was applied on a 50 m equidistant horizontal grid. Elevation of tide and surge was specified at the open boundaries at the northern and southern entrances of the Tjeldsund channel as driving force for the model. During the storm surge events the large scale external surge introduced an additional sea level difference between the northern and southern entrance of the channel of up to 1 m. This lead to a storm surge current that was found to intensify or reduce the tidal current and also reverse the direction of the current. The external sea level south and north of the channel is assumed to be the main driving force for the flow through the channel, and the local wind stress of minor importance, hence the local wind stress has been neglected in our experiments. The interaction is assumed negligible at the ends of the channel, i.e. at the open boundaries which are located in deep fjords.

To investigate the interaction mechanism in the channel time series of the mean current through a cross-section of the channel have been studied, and harmonic analyses of the tidal current and tide+surge current have been performed at six locations in the channel to study the modification of the tidal constituent M_2 and its over-harmonics due to the tide-surge interaction. The harmonic analyses where performed on relatively short time-series including a transient storm surge of duration about 24 hours. Harmonic analysis of the estimated storm surge signal used as boundary forcing shows that higher harmonics remain in the surge signal. Since the storm surge signal introduced in this way contains over-harmonics this may influence the calculations. A different approach to investigate the interaction mechanism in the channel would be to investigate a steady state situation similar to Jones & Davies (2008). This could be done by applying a constant sea level difference (corresponding to a storm surge) between the southern and northern entrance of the Tjeldsund channel in addition to sea level difference due to tide. For this thesis there was no time left to add this approach to the paper, but it will be carried out before publication of the paper.

Model simulations for this paper have been carried out in cooperation with K.B. Hjelmervik. The harmonic analyses of the simulated time series of the storm surge events are made by me. For this paper I was mainly responsible for the part concerning tide-surge interaction, while K.B. Hjelmervik was responsible for the part concerning tidal currents, summarized in sec. 3. I have contributed to much of the writing, especially sec. 4 to 7, by close iterations with Professor Bjørn Gjevik. For validation of the tidal model sea level measurements were made at two temporary tide gauges, and current recordings were carried out at three locations in the Tjeldsund channel. Analyses of the sea level and current measurements are reported in Lynge & Hareide (2005). I have also contributed to the generation of the depth matrix provided by the NHS. Preliminary results from the paper were presented in a poster session in the EGU conference in Vienna 23 April 2009.

Paper III – ADCP measurements off the Lofoten headland and comparison with high resolution tidal current models

The third part of the thesis (Lynge, 2011) reports a unique set of Acoustic Doppler Current Profiler (ADCP) measurements taken in the area off the Lofoten headland, northern Norway. The ADCP measurements were carefully planned from preliminary model simulations to reveal horizontal structures of the flow field. The measurements were made along 12 sections for a period of 8.5 hours during a survey carried out with the research vessel G.O. Sars (Institute of Marine Research (IMR), Bergen, Norway) March 2009. The depth mean current of the 1 minute averages from the current recordings are described in details. Also four cross sections of the ADCP measurements are presented to study the vertical structures of the flow field.

Model simulations have been carried out for the area off the Lofoten headland with two different tidal models, i.e. the depth integrated UiO model and the three-dimensional σ-coordinate model (BOM) with a horizontal grid resolution of 50 and 100 m. The ADCP measurements are valuable for validation of the models, though several sections are required for a better and more detailed validation of the models. A detailed comparison between the flow field revealed by the measurements and the simulated flow fields is given in the report. The tidal models have also been compared to each other in order to study the consistency of the model predictions. The two tidal current models are found to reveal the main features of the flow field as revealed in the measurements. For the small-scale dynamics of the flow field the simulated flow fields reveal some discrepancy between the two models, and also in comparison with the measurements.

Together with my supervisor Professor Bjørn Gjevik I was happy to participate on the survey with G.O. Sars March 2009. With good instructions from the technician on board and staff at IMR, I contributed to the data collection during the survey. After the survey I was responsible for processing and visualization of the data. Parts of the work presented in the report have been presented at "Geodesi og Hydrografidagene 2010" arranged by *GeoForum* in Norway.

Paper IV – Numerical studies of dispersion due to tidal flow through Moskstraumen, northern Norway

In the fourth paper of the thesis (Lynge *et al.*, 2010, published in Ocean Dynamics) the effect of horizontal grid resolution on the horizontal relative dispersion of particle pairs has been investigated on a short time scale by numerical studies. Accurate model prediction of relative dispersion of particle pairs in complex current fields can be of considerable value for several practical purposes, i.e. oil spill, dispersion of sea lice and pollutants. Of special interest has been to investigate what horizontal resolution is required to predict dispersion accurately on a short time scale when small-scale flow features are important.

In many areas in coastal waters, flow and dispersion is driven by the barotropic tide. The tidal effects on dispersion and transports are hence of particular interest. Our experiments have been carried out for the Moskstraumen Maelstrom outside Lofoten on the northern coast of Norway. The area of Moskstraumen exhibits strong tidal current with sharp horizontal current shear zones.

The three-dimensional σ-coordinate model (BOM) has been applied to simulate the tidal flow through Moskstraumen. Simulations have been carried out with spatial resolution of 50,

100, 200, 400 and 800 m in order to investigate the sensitivity of dispersion to horizontal grid size Δx and Δy. Simulations were carried out with both homogenous and stratified conditions. Lagrangian tracers were passively advected with the flow over one tidal M_2 cycle, and Lyapunov exponents and power law exponents were calculated to analyse the separation statistics.

Model simulations for this paper have been carried out in cooperation with Professor Jarle Berntsen, were I contributed to preparation of the model simulations with test simulations and preparing boundary conditions and depth matrices to the different grid resolutions applied. Calculations and analysis have been carried out by me with guidance of Professor Jarle Berntsen, and most figures are made by me. For the paper I have contributed to most of the writing, by close iterations with Professor Jarle Berntsen and Professor Bjørn Gjevik. The paper has been presented at the JONSMOD meeting 2010 in Delft.

Unfortunately we have found two misprints in the published paper. On page 910 in the right column it should be "As a driving force, tidal elevation represented by the main semi-diurnal constituent M_2,...", not diurnal as printed. On page 913 in Eq. 13 it should be $r^2_{i,j}$(t) on the left hand side.

References

ANDERSEN, O. B. 1995 Global ocean tides from ERS 1 and TOPEX/POSEIDON altimetry. *Journal of Geophysical Research* **100 NO.C12**, 25249–25259.

ANDERSEN, O. B., WOODWORTH, P. L. & FLATHER, R. A. 1995 Intercomparison of recent ocean tide models. *Journal of Geophysical Research* **100 NO.C12**, 25261–25282.

BERNTSEN, J. 2004 Users guide for a modesplit σ-coordinate numerical ocen model. version 4.1. *Tech. Rep.*. Technical Report 135, Department of Applied Mathematics, University of Bergen, Johs. Bruns gt.12, N-5008 Bergen, Norway. p.54.

BERNTSEN, J., XING, J. X. & DAVIES, A. M. 2008 Numerical studies of internal waves at a sill: Sensitivity to horizontal grid size and subgrid scale closure. *Continental Shelf Research* **28** (10-11), 1376–1393.

BERNTSEN, J., XING, J. X. & DAVIES, A. M. 2009 Numerical studies of flow over a sill: sensitivity of the non-hydrostatic effects to the grid size. *Ocean Dynamics* **59** (6), 1043–1059.

CHEN, C., HUANG, H., BEARDSLEY, R.C. & LIU, H. 2007 A finite volume numerical approach for coastal ocean circulation studies: Comparison with finite difference models. *Journal of Geophysical Research* **112, C03018**, 1–34.

DAVIES, A. M., JONES, E. & XING, J. 2010 Modelling the influence of small scale effects upon the large scale: an oceanographic challenge. *Ocean Dynamics* **60**, 921–932.

DAVIES, A. M., JONES, J. E. & XING, J. 1997*a* Review of recent developments in tidal hydrodynamic modeling. 1: Spectral models. *Journal of Hydraulic Engineering* **123** (4), 278–292.

DAVIES, A. M., JONES, J. E. & XING, J. 1997*b* Review of recent developments in tidal hydrodynamic modeling. 2: Turbulence energy models. *Journal of Hydraulic Engineering* **123** (4), 293–302.

FOREMAN, M. G.G. 1978 Manual for tidal current analysis and prediction, pacific marine science report 78-6,. *Tech. Rep.*. Institute of Ocean Sciences, Patricia Bay Sidney British Columbia.

GJEVIK, B., HAREIDE, D., LYNGE, B. K., OMMUNDSEN, A., SKAILAND, J. & URHEIM, H. 2006 Implementation of high resolution tidal current fields in electronic charts systems. *Journal of Marine Geodesy* **29** (1), 1–17.

GJEVIK, B., MOE, H. & OMMUNDSEN, A. 1997 Sources of the Maelstrom. *Nature* **388** (6645), 837–838.

HAREIDE, D. & LYNGE, B. K. 2002 Water level observations from Trondheimsleia and Frohavet. December 2001-february 2002. *Tech. Rep.*. Report GEO 02-2, Norwegian Hydrographic Service, Stavanger, Norway. 18pp.

HJELMERVIK, K.B, LYNGE, B.K, OMMUNDSEN, A. & GJEVIK, B. 2009 Modelling of tides and storm surges in the Tjeldsund channel in northern Norway. *In PhD Thesis Hjelmervik: Wave-current interactions in coastal tidal currents. Faculty of Mathermatics and Natural Sciences, University of Oslo, Norway* .

HJELMERVIK, K., OMMUNDSEN, A.. & GJEVIK, B. 2005 Implementation of non-linear advection terms in a high resolution tidal model. *Tech. Rep.*. Preprint Series, No. 1, Dept. Math. University of Oslo, Norway, ISSN 0809-4403.

JONES, J. E. & DAVIES, A. M. 2008 On the modification of tides in shallow water regions by wind effects. *Journal of Geophysical Research-oceans* **113** (C5), C05014, doi:10.1029/2007JC004310.

LE PROVOST, C., GENCO, M. L., LYARD, F., VINCENT, P. & CANCEIL, P. 1994 Spectroscopy of the world ocean tides from finite element hydrodynamic model. *Journal of Geophysical Research* **99 NO.C12**, 24777–24797.

LEFEVRE, F., LYARD, F. H., LE PROVOST, C. & SCHARMA, E. J. O. 2002 Fes99: A global tide finite element solution assimilating tide gauge and altimetric information. *Journal of Atmospheric and Oceanic Technology* **19**, 1345–1356.

LYNGE, B. K. 2011 ADCP measurements off the Lofoten headland and comparison with high resolution tidal models. *In PhD Thesis Lynge: High resolution tidal models for the Norwegian coast. Faculty of Mathematics and Natural Sciences, University of Oslo, Norway* p. pp36.

LYNGE, B. K., BERNTSEN, J. & GJEVIK, B. 2010 Numerical studies of dispersion due to tidal flow through Moskstraumen, northern Norway. *Ocean Dynamics* **60**, 907–920.

LYNGE, B. K. & HAREIDE, D. 2005 Current and sea level observations from Tjeldsundet. November 2004 –April 2005. *Tech. Rep.*. Report DAF 05-3, Norwegian Hydrographic Service, Stavanger, Norway.

LYNGE, B. K., HJELMERVIK, K. B. & GJEVIK, B. 2011 Storm surge and tidal interaction in the Tjeldsund channel, northern Norway. *In PhD thesis Lynge: High resolution tidal models. Faculty of Mathematics and Natural Sciences, University of Oslo, Norway,* p. pp26.

MARINEOBSERVATORIUM, WILHELMSHAVEN 1943 Karten der geseitenströme für die West- und Nordküste Norwegens. Heft 1: Tjeldsund (Vorläufige ausgabe). *Tech. Rep.*. Marineobservatorium Wilhelmshaven.

MOE, H., GJEVIK, B. & OMMUNDSEN, A. 2003 A high resolution tidal model for the coast of Møre and Trøndelag, western Norway. *Norwegian Journal of Geography* **57** (3), 65–82.

MOE, H., OMMUNDSEN, A. & GJEVIK, B. 2002 A high resolution tidal model for the area around The Lofoten Islands, northern Norway. *Continental Shelf Research* **22** (3), 485–504.

RAY, R. 1999 A global ocean tide model from Topex/Poseidon altimetry: Got99.2. *Tech. Rep.*. NASA Tech Memo 209478, 58 pages.

SCHUM, C. K., WOODWORTH, P. L., ANDERSEN, O. B., EGBERT, G. D., FRANCIS, O., KING, C., KLOSKO, S. M., LE PROVOST, C., LI, X., MOLINES, J-M., PARKE, M. E., RAY, R. D., SCHLAX, M. G., STAMMER, D., TIERNEY, C. C., VINCENT, P. & WUNSCH, C. I. 1997 Accuracy assessment of recent ocean tide models. *Journal of Geophysical Research* **102 NO.C11**, 25173–25194.

SCHWIDERSKI, E. W. 1980 On charting global ocean tides. *Reviews of Geophysics* **18** (1), 243–268.

Papers

Paper I **Gjevik et al.** 2006
Implementation of high resolution tidal current fields in electronic navigational chart systems
Marine Geodesy **29**, 1-17.

Paper II **Lynge, B.K. & Hjelmervik, K. & Gjevik, B.** 2011
Storm surge and tidal interaction in the Tjeldsund channel, northern Norway

Paper III **Lynge, B.K.** 2011
ADCP measurements off the Lofoten headland and comparison with high resolution tidal current models

Paper IV **Lynge, B.K. & Berntsen, J. & Gjevik, B.** 2010
Numerical studies of dispersion due to tidal flow through Moskstraumen, northern Norway
Ocean Dynamics **60**, 907-920.

Paper I

Implementation of high resolution tidal current fields in electronic navigational chart systems

Paper II

Storm surge and tidal interaction in the Tjeldsund channel, northern Norway

Storm surge and tidal interaction in the Tjeldsund channel, northern Norway

B. K. Lynge[1,2] K. Hjelmervik[1,3] B. Gjevik[1]

Abstract

A high resolution depth integrated tidal and storm surge model with horizontal grid resolution down to 50 meters has been implemented for the Tjeldsund channel in northern Norway. The model has been used to simulate tides and tide-surge interaction. Two typically storm surge events in December 2004 have been examined in detail. The tide surge interaction is found to influence the generation of higher harmonics and the formation of eddies in the current field.

1 Introduction

The non-linear interaction between tides and storm surges has been studied extensively by e.g. Prandle and Wolf (1978); Johns et al. (1985); Tang et al. (1996); Bobanovic et al. (2006); Horsburgh and Wilson (2007); Jones and Davies (2007, 2008), and references therein. The focus has mostly been on how the interaction affects the elevation of the surge and the timing of high water relative to the phase of the tide. The non-linear quadratic bottom friction, used in most shallow water models, is found to play an crucial role for the tide-surge interaction, but the coupling between the surge and the tide through the non-linear momentum terms is also important. The latter mechanism is particularly important for the non-linear modification of the current field by generation of higher harmonics and short periodic current oscillations by shear flow instability. In shallow water regions the tide-surge interaction may both influence the surge and modify the tide at the time of the surge (Jones and Davies, 2008).

In the present study we shall study the tide-surge interaction in the narrow and relatively shallow Tjeldsund channel which connects two large and deeper fjord systems Vestfjorden and Vågsfjorden in the Lofoten area in northern Norway (Figs. 1-2). The channel is an important sailing lane for coastal traffic also including large vessels. The tidal range is about 4 m at Narvik at the head of Vestfjorden and 3 m at Harstad in Vågsfjorden. The tides in this area have previously been modeled with a regional model with 500 meters horizontal grid resolution (Gjevik et al., 1997; Moe et al., 2002). More recently Hjelmervik et al. (2005, 2009) used a high resolution model with horizontal grid resolution down to 25 m to simulate the tidal flow in the Tjeldsund channel. In the latter paper some aspects of the tide and surge interaction were also discussed.

[1]Department of Mathematics, University of Oslo, P.O.Box 1053, Blindern, 0316 Oslo, Norway.

[2]The Norwegian Hydrographic Service, P.O.Box 60, 4001 Stavanger, Norway.

[3]Department of Maritime Tehnology and Innovation, Vestfold University College, P.O.Box 2243, 3103 Tønsberg, Norway

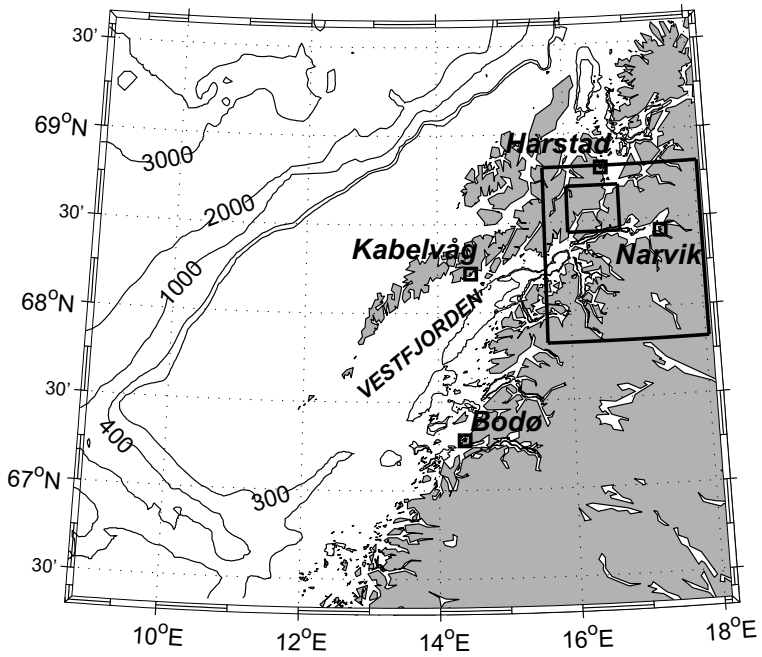

Figure 1: Location of the model domains (rectangles) on the northern coast of Norway. Enlargement of the inner domain is shown in Fig. 2. Depth contours in meters.

During a storm situation, with low atmospheric pressure and strong southwesterly wind, the sea level in the inner part of Vestfjorden often rises up to 1 m due to the atmospheric forcing. The large scale external surge in the fjords can in such situations lead to a sea level differences up to 1 m between the ends of the Tjeldsund channel. This can introduce a current through the channel of the order 1 ms^{-1}, which is of comparable strength to the tidal current. The current associated with strong storm surge events is mainly driven by external surge in the deep fjords north and south of the channel. The local wind stress on the water masses within the channel contributes less to the current due to the sheltering effect by the high and irregular mountains in the area.

The surge current may intensify or reduce the tidal current depending on the phase of the tide relative to the timing of the peak surge driven current. In narrow and shallow parts of the channel the current can also be strong enough to produce non-linear interaction between the surge and the tide with the generation of higher harmonics, flow separation with eddies at bends in the channel, and short periodic current oscillation due to shear flow instability. In contrast to the situation in most estuaries the maximum tidal current in the Tjeldsund channel occurs nearly at the time of high and low water respectively. To our knowledge this particular tide-surge interaction problem in a narrow channel have not been reported previously. The focus will be on well mixed conditions which usually occur during autumn and winter. Hence we will use the depth integrated shallow water

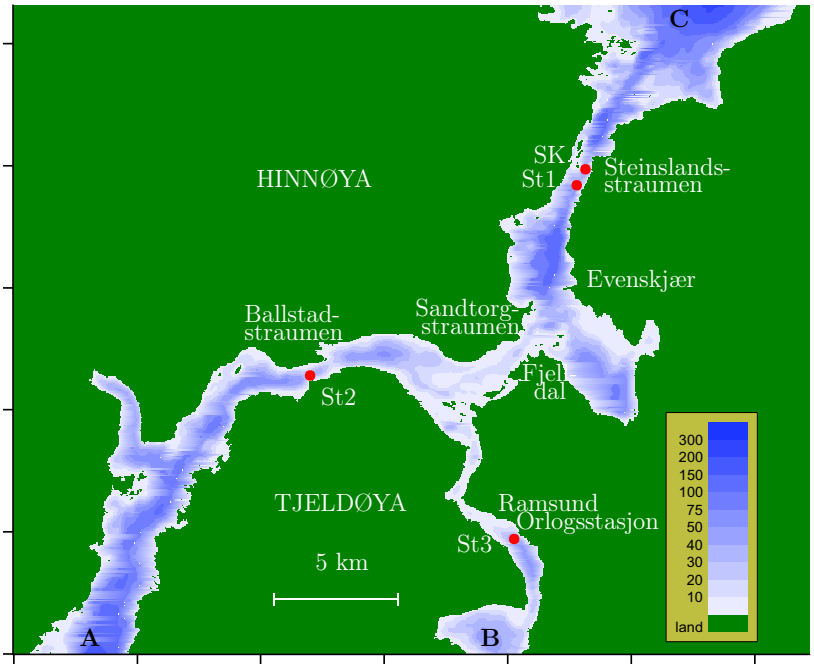

Figure 2: The inner model domain for the Tjeldsund channel with the Ramsund branch to the right. Bottom topography is shown by colour shading with depth in meters on the scale. Location of the stations with current measurements marked St1–St3 and SK. Distance between ticks on the axis is 5 km.

equations which have been applied extensively for modeling tides and storm surges in shelf and coastal areas (Davies et al., 1997a,b, and references therein).

The challenges with numerical modeling of the tidal and storm surge current in the Lofoten area are many. First of all, the complex bottom topography and coastline require a very fine spatial grid resolution. Secondly, in order to capture the formation of narrow jets and small scale eddies it is essential that the numerical scheme maintains the correct balance between advection and dissipation terms in the equations of motion.

In narrow channels and sailing lanes with busy traffic as in Tjeldsund, the current represents a considerable safety hazard. Currents of 1 ms^{-1} may introduce forces on large ships of the same order of magnitude as gale force winds. This may make it difficult to manoeuvre large ships in the channel, with the risk of being carried off the recommended sailing lane. Wave-current interaction may also introduce additional complications for safe sailing (Hjelmervik and Trulsen, 2009). If the current field can be predicted with a reasonable accuracy, this may improve the safety of sailing and reduce the risk for ship collisions and groundings. Accurate predictions of currents may also prove valuable during clean-up operations after oil-spill disasters and search, rescue and surveillance operations during ship accidents.

Recently it has been demonstrated how predicted high resolution tidal current fields can be displayed in real time on modern electronic navigational charts, and thereby become a useful tool for navigators (Gjevik et al., 2006).

2 Numerical model

The depth-integrated shallow water equations in a Cartesian coordinate system (x, y, z) with the x- and y-axis horizontal in the level of the undisturbed surface, are given by:

$$\frac{\partial \eta}{\partial t} = -\frac{\partial U}{\partial x} - \frac{\partial V}{\partial y} \tag{1}$$

$$\frac{\partial U}{\partial t} + \frac{\partial}{\partial x}\left(\frac{U^2}{H}\right) + \frac{\partial}{\partial y}\left(\frac{UV}{H}\right) - fV = -gH\frac{\partial \eta}{\partial x} + F^x + A^x \tag{2}$$

$$\frac{\partial V}{\partial t} + \frac{\partial}{\partial x}\left(\frac{UV}{H}\right) + \frac{\partial}{\partial y}\left(\frac{V^2}{H}\right) + fU = -gH\frac{\partial \eta}{\partial y} + F^y + A^y \tag{3}$$

where t is the time, (U, V) are the components of volume flux vector per unit length in the horizontal plane, η the vertical displacement of the sea surface from the mean sea level, $H = H_0 + \eta$ the total depth, H_0 the mean depth, g the acceleration of gravity, and f the Coriolis parameter. The bottom friction terms, F^x and F^y, are given by:

$$F^{x,y} = -c_D \frac{(U, V)}{H}\frac{\sqrt{U^2 + V^2}}{H} \tag{4}$$

where c_D is the drag coefficient of the quadratic bottom shear stress. The horizontal eddy viscosity terms, A^x and A^y, are parameterized by a simple Large Eddy Simulation (LES) model:

$$A^{x,y} = \nu\frac{\partial^2}{\partial x^2}(U, V) + \nu\frac{\partial^2}{\partial y^2}(U, V) \tag{5}$$

or

$$A^{x,y} = \frac{\partial}{\partial x}\left(\nu\frac{\partial}{\partial x}(U, V)\right) + \frac{\partial}{\partial y}\left(\nu\frac{\partial}{\partial y}(U, V)\right), \tag{6}$$

where ν is the eddy viscosity coefficient of the horizontal shear stress. For most of the simulations Eq. 6 has been used for calculations of the horizontal eddy viscosity. Tests have also been run with the expression in Eq. 5. The eddy viscosity coefficient is expressed according to Smagorinsky (1963), by:

$$\nu = ql^2\left[\left(\frac{\partial \overline{u}}{\partial x}\right)^2 + \frac{1}{2}\left(\frac{\partial \overline{u}}{\partial y} + \frac{\partial \overline{v}}{\partial x}\right)^2 + \left(\frac{\partial \overline{v}}{\partial y}\right)^2\right]^{\frac{1}{2}} \tag{7}$$

where q is a constant, l is a length scale which is set equal to the grid size, and $(\overline{u}, \overline{v})$ denote the components of the depth mean current velocity defined to the first order by:

$$\overline{u} = \frac{U}{H}, \qquad \overline{v} = \frac{V}{H}$$

With q=0.5, a grid size of 100 meters, and a current speed of the order 1 ms^{-1}, Eq. 7 leads to an eddy viscosity coefficient of the order $50\,\mathrm{m}^2\mathrm{s}^{-1}$.

The model equations 1–3 are discretized on a quadratic C-grid (Mesinger and Arakawa, 1976) with a finite difference numerical scheme centered in space and forwarded in time. The advection terms are estimated with an extrapolation routine for the grid points near

the coastal boundaries in order to avoid one-sided differences. Further details on how the numerical scheme is designed and its performance for this particular application, can be found in Hjelmervik et al. (2005).

The CFL-stability criterion satisfied by the numerical time step, Δt, is:

$$\Delta t \leq \frac{\Delta x}{2\sqrt{2gH_{max}}}$$

where H_{max} is the maximum depth of the model domain.

2.1 Model setup and boundary conditions

The numerical model has been set up for two rectangular domains depicted in Figs. 1 and 2. The larger domain cover the inner part of Vestfjorden with adjacent fjord systems south and west of the Tjeldsund channel. North of the channel the southern part of Vågsfjorden is covered up to Harstad. The total extent of the domain is 96×103 km. The inner model domain (small rectangle, Fig. 1) covers only the Tjeldsund channel with the Ramsund branch. The inner domain has two open boundaries towards Vestfjorden and one open boundary towards Vågsfjorden on the northern end of the channel. The south-westerly corner of the domain has coordinates X= 541250 and Y = 7593800 (given to WGS84-UTM zone 33) and the domain covers 39×27 km in the x, y directions, respectively. The coordinate axis (x, y) are orientated west-east and south-north respectively.

High resolution bottom topography based mainly on multibeam bathymetric data from Norwegian Hydrographic Service (NHS) is used to generate the bottom matrices. Depths are related to Mean Sea Level (MSL) which differs from Chart Datum (CD) as used in nautical charts, and depths are mapped to datum WGS84-UTM zone 33. Model simulations with a horizontal grid resolution $\Delta x = \Delta y$ ranging from 25 to 100 meters have been performed, 25 and 50 m for the inner domain, and 100 m for the larger domain. The results presented in this paper are from the inner domain, and a horizontal equidistant grid with resolution 50 m was applied.

The area of interest is the narrow and shallow areas of the Tjeldsund channel and the Ramsund branch, and by using the small domain we are able to refine the resolution for this area. Comparison between simulations for the two domains shows only small deviations, and justify the use of the smaller domain for our purpose (Hjelmervik et al., 2009).

As driving force surface elevation is specified at the open boundaries. Experiments have been carried out with three different boundary forcing, that is; surface elevation from tide only forcing, surface elevation from storm surge, and finally the total sea level (tide + storm surge). Tidal predictions and constituents and observed sea level were obtained from sea level data from the permanent NHS recording stations at Narvik and Harstad located in the vicinity of the model area (Fig. 1). Since both Narvik and Harstad are located in broad and relatively deep fjords we have neglected the tide surge interaction and obtained the storm surge by simply subtracting the predicted tide from the observed see level signal (see also Jones and Davies, 2008). At the two southern open boundaries in Tjeldsund (A) and Ramsund (B) respectively (see Fig. 2) we have extrapolated sea level data westward from Narvik. Amplitude is reduced with a factor 0.97 and 0.99 respectively compared to the data from Narvik. At the northern boundary (C) we have extrapolated southward from Harstad, and the amplitude is increased with a factor 1.01 compared to the data from Harstad. In view of the small differences in phases between Narvik and Harstad and the

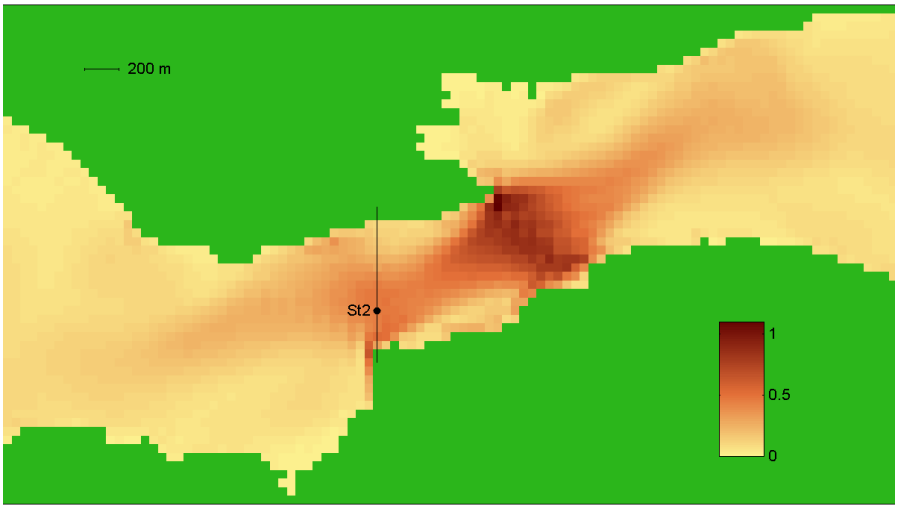

Figure 3: The tidal current level in Ballstadstraumen displayed by contour plot of the M_2 major current axis. Colour scale in ms^{-1}. The cross section for volume flux calculations and the station for current records are marked.

respective open boundaries no corrections have been made to the phases. Hence along the boundaries which are located in deep water we have neglected the tide-surge interaction. That a linear decomposition of the tide and the surge is possible in deep water was also anticipated by Jones and Davies (2008). This enable us to study the tide-surge interaction in the narrow and shallow Tjeldsund channel. Local wind-stress has been neglected in our experiments. This conjecture is based on the assumption that the external sea level south and north of the Tjeldsund channel is the main driving force for the flow through the channel, and that the local wind-stress in the channel is of minor importance.

At the open boundaries the flow relaxation scheme (*FRS*) (Martinsen and Engedahl, 1987) has been used to impose the boundary conditions. Surface elevation is updated in every time step according to

$$\phi = (1 - \alpha)\phi_{int} + \alpha\phi_{ext}, \tag{8}$$

where ϕ_{int} contains the unrelaxed values computed by the model, and ϕ_{ext} is a specified external value. The relaxation parameter varies smoothly from 1 at the open boundary to 0 at the innermost cell of the boundary zone. The rationale behind this scheme is to soften the transition from an exterior solution to an interior solution by use of a grid zone where the two solutions dominate at each ends respectively. The width of the zone is taken to be ten grid cells.

All simulations started from rest (U, V and η equal zero) with increasing boundary forcing in time according to a ramping function, $(1 - \exp(-\sigma t))$. A value of $\sigma = 4.6 \times 10^{-5} s^{-1}$ has been used. This implies full driving effect of the boundary conditions after about 12 hours.

Among the challenges for simulations with non-linear advection terms for this complicated coastline configuration and bathymetry is to obtain stable solutions by adjusting the horizontal eddy viscosity. In order to check the sensitivity of the solutions to different

values of eddy diffusivity parameters, a series of separate simulations have been done for the semi-diurnal M_2-component. Based on the results of Hjelmervik et al. (2005), we have chosen $q = 0.5$ for grid size $\Delta x = 50$ m. The large value of $c_D = 0.0075$ is also in accordance with other high resolution models as for example Sutherland et al. (2005).

A 24 hours spin up time is found to be sufficient to obtain an acceptable steady state. After 48 hours, complete fields for current and elevation data are stored every hour. Data for surface elevation, current strength and direction from selected stations (grid nodes) were stored with 180 s sampling for later processing.

3 Tidal simulations

Tidal simulations have earlier been carried out for the entire domain, covered by the map in Fig. 1, with 500 m horizontal grid resolution (Moe et al., 2002). Results from these simulations have been used to obtain interpolated boundary conditions for the domain marked with the largest rectangle in Fig. 1 (Hjelmervik et al., 2009)

The depth integrated model has been run for the four major tidal constituents, i.e. the three major semi-diurnal components M_2, S_2, and N_2, and the major diurnal component K_1, for the two rectangular domains marked in Fig. 1. The modeled current fields displayed the characteristic features of the tidal current in the Tjeldsund and Ramsund channels. The three areas with the strongest currents are localized at Ballstad, Sandtorg, and Steinsland, see Fig. 2. The horizontal variation in the current field at Ballstad is shown in Fig. 3.

For a period from November 2004 to March 2005 current measurements where executed at two locations in the Tjeldsund channel, at Steinsland and Ballstad (St1 and St2 respectively in Fig. 2). See sec. 6 for more details on the field measurements. A detailed comparison between modeled and observed tidal parameters is given in Hjelmervik et al. (2009), also including current records from 1985 station SK (Fig. 2). Maximum current speed through various sections of the channel where found to occur around time of high and low water, in agreement with observations, see Fig. 4.

Detailed plots of the current fields reveal a system of eddies which are controlled to a large extent by the bathymetry and the bottom friction. The effects of the over-harmonic tidal components were also examined, mainly M_3, M_4, and M_6, with periods 8.28, 6.21, and 4.14 hours, respectively. While the sea level amplitude of the over-harmonics are small and less then 3 percent of the M_2 amplitude, the over-harmonics are much more pronounced in the simulated current data, i.e. 5-14 percent of the M_2 amplitude in the mean current in the cross-sections at Ballstad, Sandtorg and Steinsland. The amplitude of the over-harmonics varies considerably over relatively short distances, and are to a large extent associated with eddies, either topographically trapped or slowly propagating (Hjelmervik et al., 2009).

4 Storm surge events

In the period November 2004 - April 2005, current sensors deployed in the Tjeldsund and Ramsund channels captured several storm surge events. The storm surges introduced additional sea level differences up to 50 cm between the southern and the northern entrances of the channel which modified the tidal current pattern. The residual sea level (observed sea level minus predicted tide) from Harstad in the north and Narvik in south are shown in Fig. 6 together with the residual sea level difference between Narvik and Harstad. Since

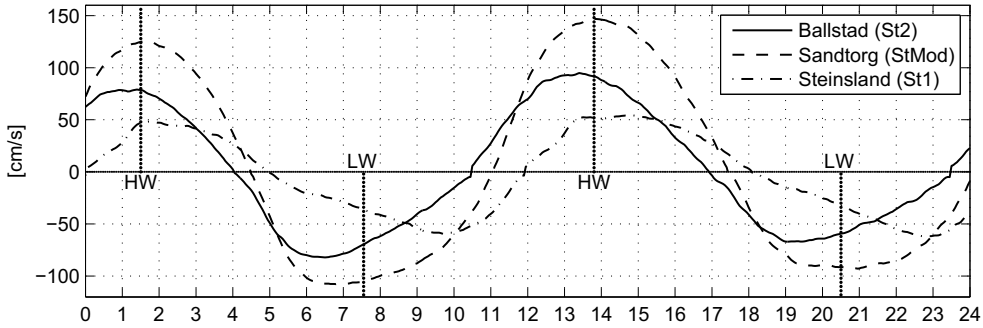

Figure 4: Modeled tidal current speed relative to local high and low water on 15 December 2004 (24 hours UT) at Ballstad (station St2), Sandtorg (StMod), and Steinsland (station St1) (Fig. 2). Positive value for north-east and negative for south-west.

both Narvik and Harstad are located in relatively deep fjords, the effect of non-linear interaction between the surge and the tide is believed to be negligable for these stations (see sec. 2.1). We have examined in detail two cases which represent typical strong storm surge events in the area.

Case I, 12-16 December 2004: Surface weather map from 15 December 00:00 UT shows a 960 hPa deep depression with center west of Lofoten, at N 70^o, E 5^o (Fig. 5). It caused strong southwesterly winds in Vestfjorden. The combined effect of wind and low air pressure induced a higher sea level in Vestfjorden and the inner extension called Ofotfjorden. The storm surge event occurred shortly after new moon 12 December, i.e. during a spring tide with stronger tidal currents. In Narvik the storm surge reached its maximum (104 cm, predicted tide subtracted) at 02:10 UT on 15 December, shortly after the time of high tide at 01:30 UT. Residual sea level was high for about 10 hours before maximum occurred. In Harstad the storm surge reached maximum (67 cm) at 04:30 UT at ebbing tide. The difference in residual sea level between Narvik and Harstad was about 30-40 cm for about 10 hours reaching a maximum 48 cm at 02:10 UT 15 December, with residual sea level higher in Narvik than in Harstad. At 06:30 UT 15 December the residual sea level difference reversed changing to minus 36 cm at 09:20 UT. The residual sea level difference stayed at about minus 25 cm for about 10 hours.

Case II, 20-24 December 2004: The weather situation was similar to Case I and the surface weather maps from 23 December, 00:00 UT shows an unusual deep depression (935 hPa) with centre west of Lofoten at N 73^o, E 5^o. The southwesterly wind and low air pressure lead to high sea level in Vestfjorden. The storm surge event occurred shortly after half-moon 18 December and hence during neap tide. The storm surge reached maximum (91 cm) in Narvik 14:10 UT 22 December just before ebb at 15:00 UT and remained quite high for about 8 hours. In Harstad the storm surge reached its maximum (50 cm) at 17:10 UT about 4 hours before high tide at 21:15 UT 22 December. Residual sea level stayed at the same level about one tidal period (12.5 hours) during high and low tide. The difference in residual sea level between Narvik and Harstad attained its maximum (49 cm) at 14:10 UT 22 December (highest in Narvik) and the maximum reverse difference (44 cm) occurred at 02:30 UT 23 December.

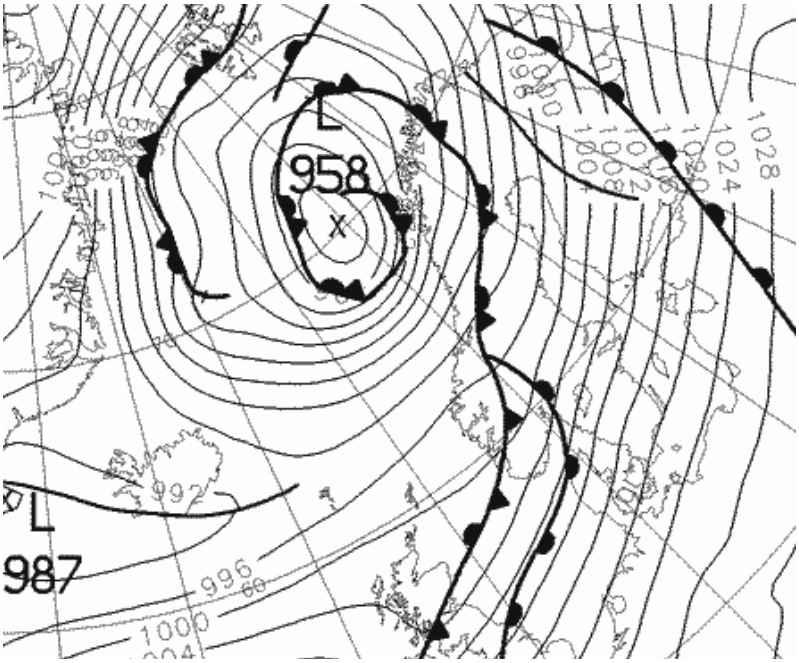

Figure 5: Surface weather map from 15 Dec 2004 00:00 UT (From UK Met Office archive).

5 Tide-surge interaction mechanism

In order to investigate the interaction between the tidal current and the additional current induced by the storm surge, the model has been run for the inner domain (Fig. 1) for 8 M_2 tidal periods (after a 24 hour spin up) on a 50 m grid. Experiments have been carried out with three different boundary forcing (see sec. 2.1) for the two storm surge events in December 2004 described in sec. 4. For the simulations presented here, the tidal forcing is represented only by the major semi-diurnal tidal constituent M_2. This was done in order to be able to study the interaction mechanism more closely by harmonic analyses of the relatively short simulated current time series with length comparable to the duration of the surge. A similar approach, studying only the effect of M_2, was advocated by Jones and Davies (2008). Time series of the storm surge have been obtained, like described in sec. 2.1 by subtracting the tidal prediction from the observed sea level. The tidal elevation from the M_2 constituent and the storm surge were added to represent the total sea level during the storm surge event. Our focus will be on the non-linear tide-surge interaction in the shallow Tjeldsund channel and we have assumed that the interaction is negligible at the ends of the channel i.e. at the open boundaries which are located in deep fjords (see sec. 2.1). In these experiments Eq. 6 was used for calculations of the horizontal eddy viscosity.

We consentrate the investigation of the interaction mechanism for an area in the shallow Ballstadstraumen, see Fig. 2, where the tidal simulations show strong current, flow separation, and topographically trapped eddies. The mean current through the cross-section, shown in Figs. 3 and 7, has been used as an integrated measure of the current conditions

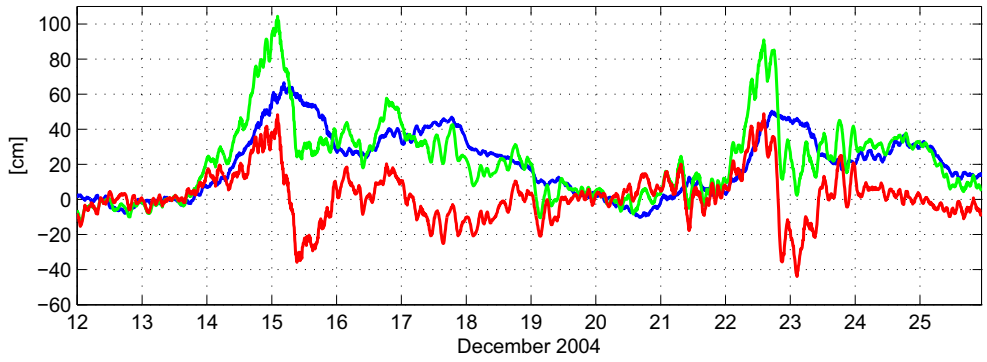

Figure 6: Residual sea level (observed sea level minus predicted tide) from Narvik (green) and Harstad (blue) and residual difference (Narvik minus Harstad) (blue) for the period 12 -26 December 2004.

in the channel. In the following discussion we use the term tidal current for the current obtained by only M_2 boundary forcing, total current for the combined effect of storm surge and M_2-tide, and storm surge current for the current obtained by only storm surge forcing at the boundaries.

The storm surge events introduce a difference between the sea level at the northern and southern entrance of the channel of up to 0.7 m. This intensifies or reduces the tidal current according to the time of the surge relative to the phase of the tide. The total volume fluxes through cross-sections of the channel are found to be nearly proportional to the sea level difference between the northern and southern entrances. This is clearly seen by comparing the storm surge difference between the northern and southern entrance and the modeled storm surge current in the cross-section at Ballstad (upper and lower panels Figs. 8 and 9). We note that the storm surge current in both cases is persistent in the same direction for up to 24 hours i.e. longer than the semi-diurnal tidal oscillation. The total current is at its strongest when maximum tidal current and maximum storm surge current are in phase and contributes in the same direction. That is when maximum difference in tidal elevation between the northern and southern entrances coincide with the corresponding maximum difference in the storm surge. This situation occurred during Case I early on 15 December (Fig. 8) when the eastward storm surge current and the eastward tidal current reached maximum at about the same time. Fig. 10 shows the tidal current in Ballstadstraumen at 02:00 UT 15 December while Fig. 11, from the same site, shows how the storm surge and the tidal current add up to an intensified current. This also affects the topographically trapped eddies respectively on the northern and southern sides of the channel. A similar situation occurred during Case II early on 23 December when the westward storm surge current and the westward tidal current reach maximum at about the same time (Fig. 9).

The total current is reduced or reversed when the tidal current and storm surge current contribute in opposite directions. An example is seen in Case I, at the second ebb tide 14 December, when the eastward storm surge current dominates the westward tidal current and prevents the reversal of the current (Fig. 8). The same situation occurred in Case II the 22 December at the second ebb tide where the eastward storm surge current dominates over the westward tidal current. Therefore the total current continues in eastward direction

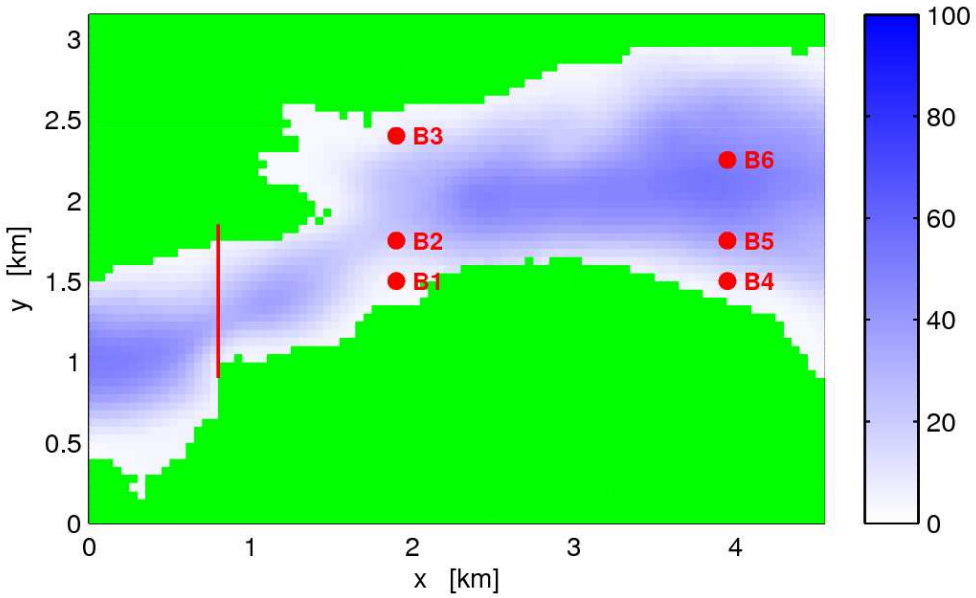

Figure 7: Bathymetry of the Ballstadstraumen area with cross-section for mean current flux calculations and the locations B1-B6 used for harmonic analyses. Colour bar for depth in meters.

during the ebb tide (Fig. 9). Figs. 12 and 13 show respectively the tidal current and the total current at 13:00 UT 22 December in Ballstadstraumen, where the storm surge opposes the tidal current and reversing the direction of the total current and leading to a reduction of the speed.

In order to investigate how the current conditions changes when the storm surge occurs at other phases of the tidal cycle we have modified Case II. The observed storm surge at Narvik and Harstad were artificially phase shifted 5 hours so that the maximum surge in Narvik coincide with the first high tide in Narvik 22 December 2004. The phase shifting enhances the interaction between the surge and the tide, and the total current through the cross-section at Ballstadstraumen reaches about 10 cms^{-1} higher than in Case II. This shows that maximum current speed can become larger than in the two cases in December 2004 depending on in which phase of the tidal cycle the storm surge occurs.

5.1 Non-linear interaction

The non-linear interaction between the tidal current and the storm surge current can be studied by comparing the difference between the total current (simulated by $M_2 +$ storm surge forcing at the open boundaries) and the tidal current, with the simulated storm surge current (lower panels, Figs. 8 and 9). When the tidal and the storm surge currents contribute in the same direction, the difference between the total current and the tidal current (black curve) is smaller than the storm surge current (red curve). Contrary, the difference is larger when they contribute in opposite directions. This means that the storm surge current and the tidal current do not simply add, particularly when the tides and the

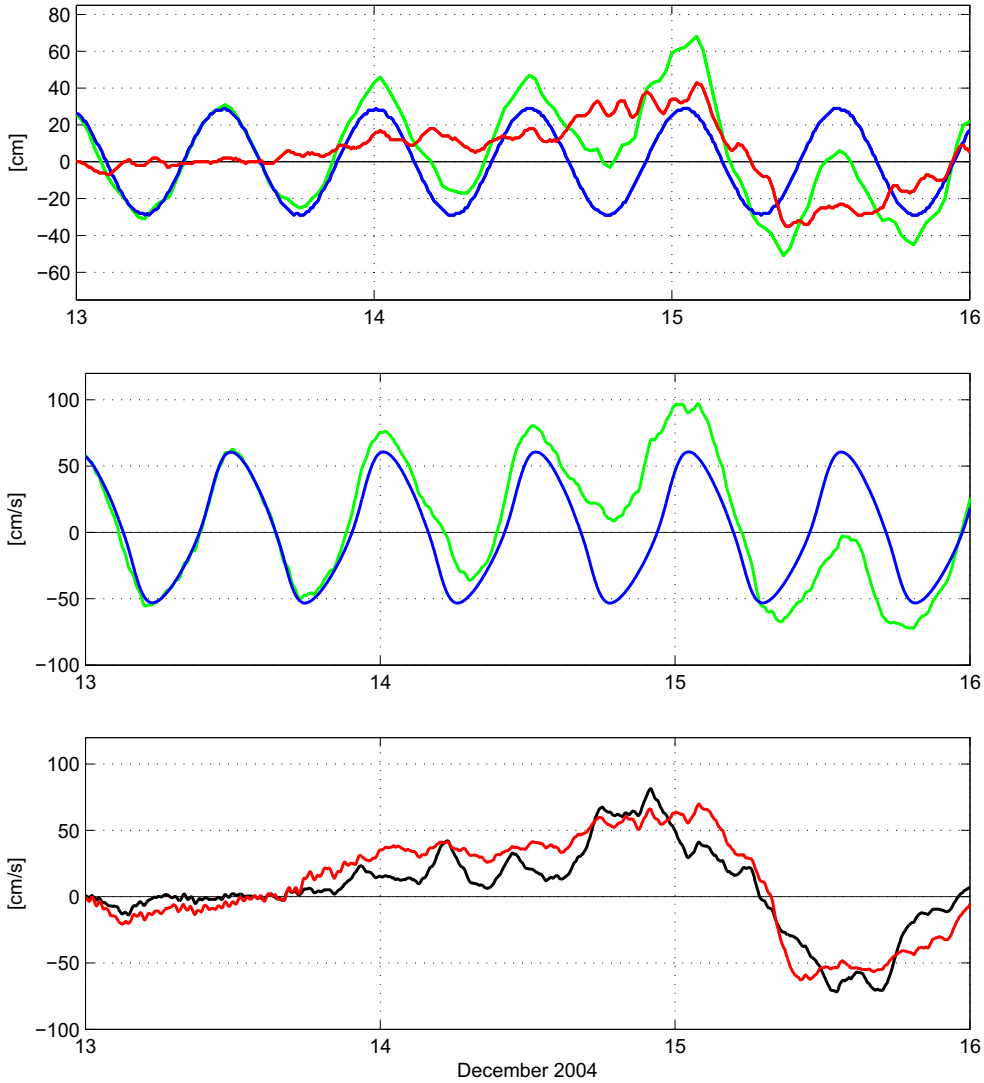

Figure 8: Case I: 13-15 December 2004. Upper panel: Sea level difference between Narvik and Harstad, predicted M_2 tide (blue), storm surge (red), and tide + surge (green) Middle panel: Modeled mean current through the cross-section at Ballstadstraumen. Tidal M_2 current only (blue), tide + storm surge current (green). Lower panel: Modeled mean storm surge current through the cross-section at Ballstadstraumen (red), and the difference between the modeled tide + storm surge current and modeled tidal M_2 current (black), which is the difference between the green and the blue line in middle panel. Positive values indicate eastward direction.

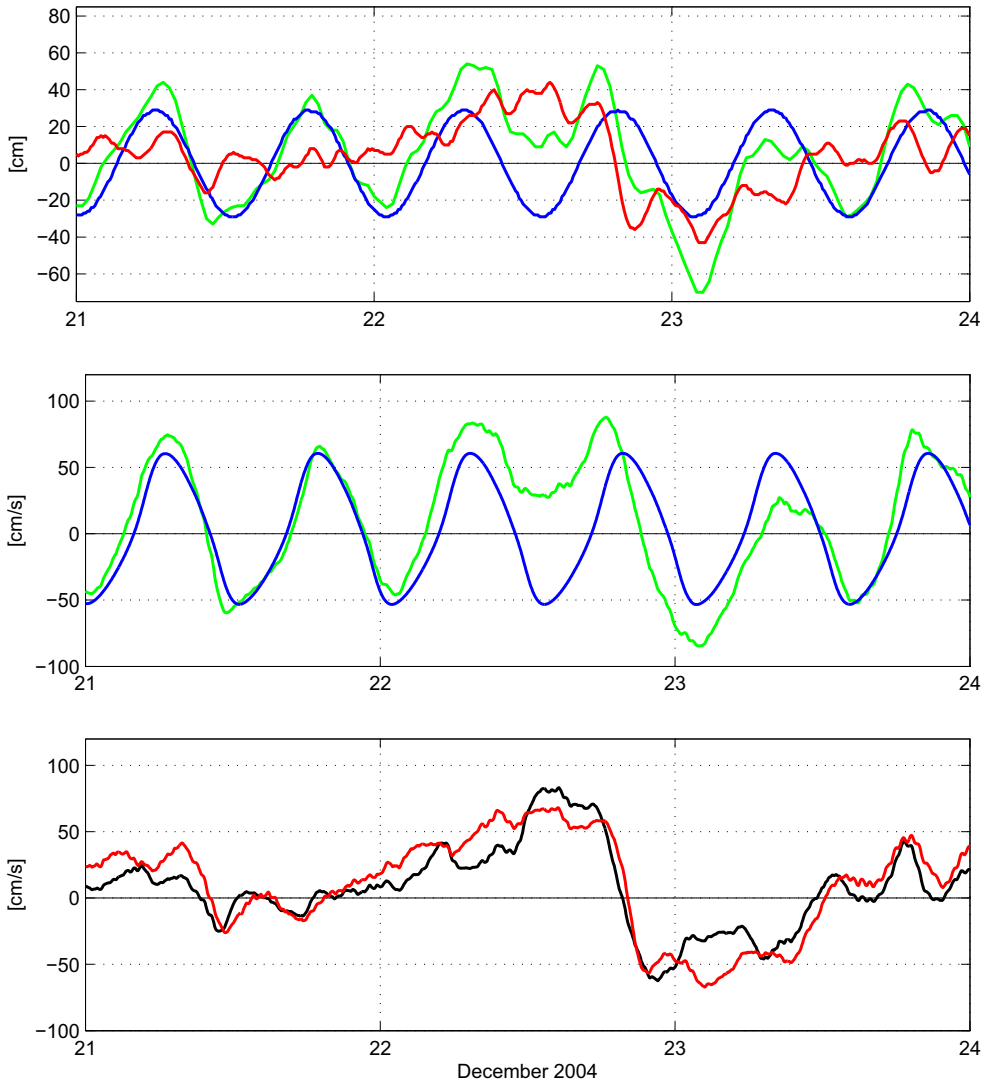

Figure 9: Case II: 22-24 December 2004. Legend as in fig. 8.

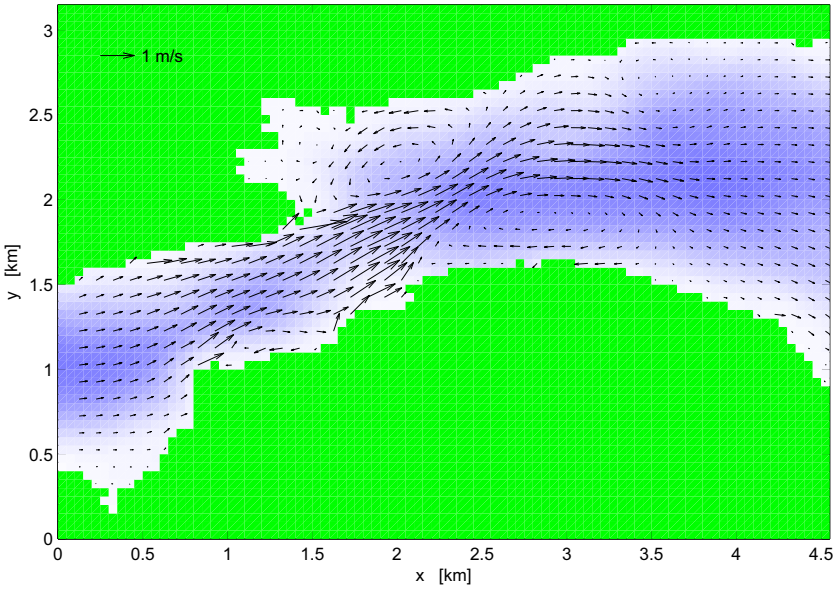

Figure 10: Case I: The M_2 tidal current in Ballstad 15 December 2004 02:00 UT.

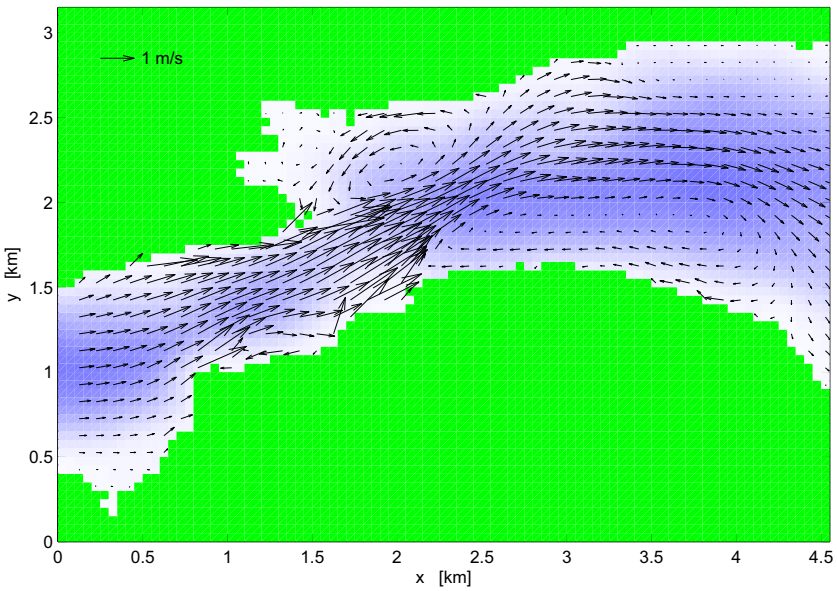

Figure 11: Case I: The total current (M_2-tide + surge) in Ballstad 15 December 2004 02:00 UT.

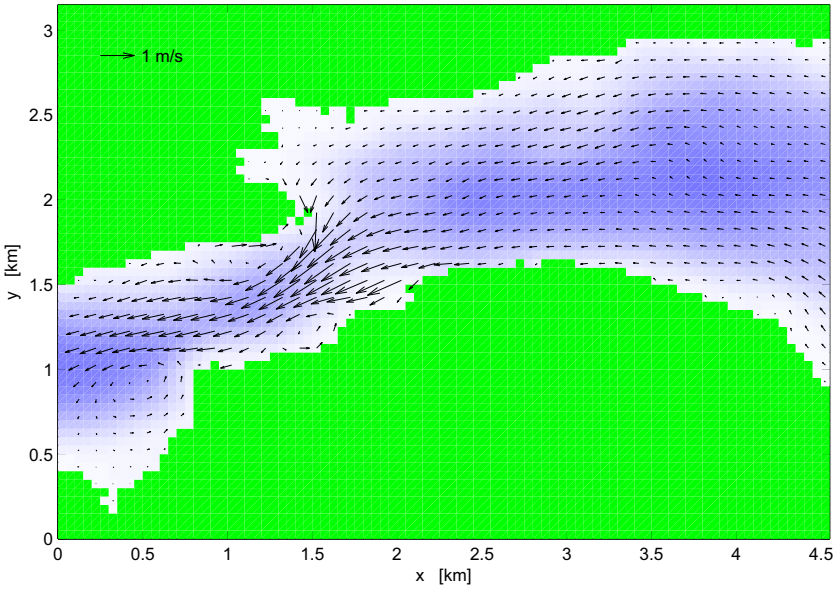

Figure 12: Case II: The M_2 tidal current in Ballstad 22 December 2004 13:00 UT.

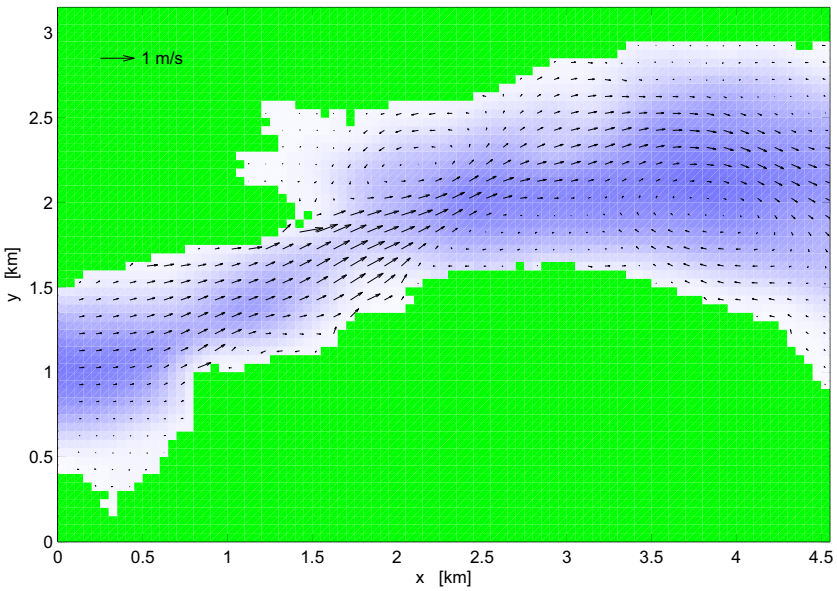

Figure 13: Case II: The total current (M_2-tide + surge) in Ballstad 22 December 2004 13:00 UT.

storm surge contribute in the same direction and the total current is at its strongest. In this case the effect of the interaction can reduce the storm surge current with up to 50 percent (see case I, 15 December Fig. 8 and case II, 22 and 23 December Fig. 9).

Studies of the dynamical interaction between tide and storm surge have earlier been carried out mainly for sea level elevation (Prandle and Wolf, 1978; Tang et al., 1996). They demonstrated that the non-linear interaction mechanism is predominantly due to the quadratic bottom friction. To study the dynamics of the mean current through a cross-section in Ballstadstraumen (marked in Fig. 7), simulations with and without the non-linear advective terms in Eq. 2 and 3 have been performed. The results from simulations without the non-linear advective terms show only small deviations from the simulations with non-linear advective terms. Similar results are found for other cross-sections in the Tjeldsund channel. The major source of non-linear interaction as manifested in the *mean* total current through a cross-section of the channel is hence mainly due to the non-linear bottom friction (Eq. 4).

When the storm surge contributes to an intensified current the bottom shear stress also increases and results in an increased bottom friction which act on the current to slow it down. This can explain that the difference between the total current and the tidal current (black curve) is smaller than the sole storm surge current (red curve) (lower panel, Figs. 8 and 9). When the storm surge and the tidal current contribute in opposite directions the current is reduced or reversed resulting in a less energetic current, and hence also the effect of the bottom friction is reduced. In this case the difference between the simulated total current and the simulated tidal current is larger than the simulated storm surge current due to the reduced effect of the bottom friction. A test has also been performed with increased drag coefficient c_D. By doubling c_D the current speed is reduced by about 20 %.

Although the non-linear advective terms have minor influence on the *mean* current through cross-sections as discussed above, these terms are essential for modeling of flow separation and shear flow instability. The two eddies seen in Ballstadstraumen in Figs. 10 and 11, one on the northern and the other (weaker) on the southern side, do not appear in simulations without the non-linear advective terms, see Figs. 14 and 15. It is interesting to discuss how the non-linear tide-surge interaction influences the strength of the eddies and formation of higher harmonics.

The formation of the two eddies which appear in Ballstrastraumen during eastward current in the simulations with non-linear advective terms (Figs. 10 and 11) is affected by the storm surge events. The eddy on the northern side is significantly enhanced in simulations when the tidal and storm surge currents both are in eastward direction (Fig. 11). The center of the eddy on the southern side of the channel moves eastward with the eastward current. The extension of the eddy depends on the strength of the current and duration of the eastward current. Since the period of eastward current is prolonged by the storm surge (see Fig. 8) the eddy on the southern side is extended and the center of the eddy moved eastward during the eastward storm surge current on December 15 (Fig. 11).

5.2 The modification of the tide due to non-linear interaction

In order to get more insight in how the tide-surge interaction modifies the tide at the time of the surge (see Jones and Davies, 2008) we have used harmonic analysis to study the modification of the M_2-component and its main over-harmonics M_4 and M_6. Time series of the modeled current at the six locations B1 - B6 (marked in Fig. 7) have been analysed by

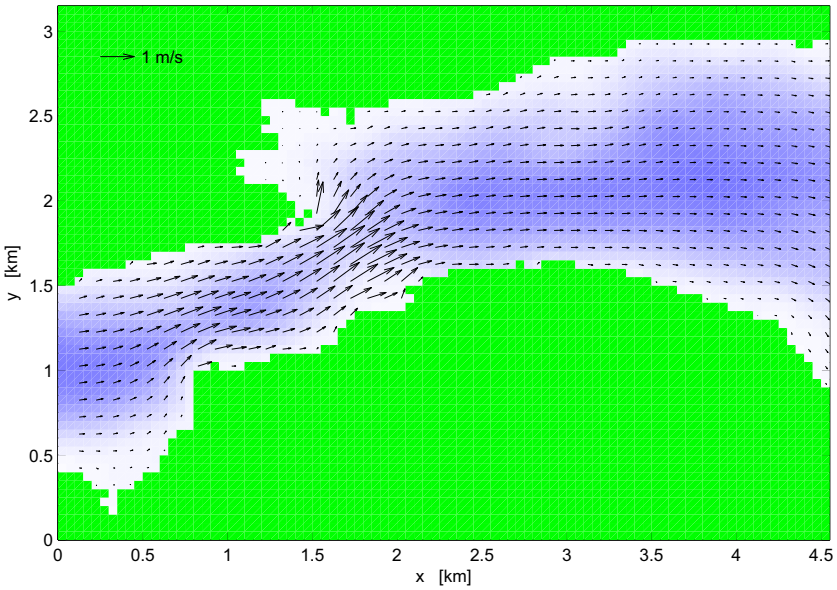

Figure 14: Case I: The M_2 tidal current in Ballstad 15 December 2004 02:00 UT. Simulations without non-linear advective terms.

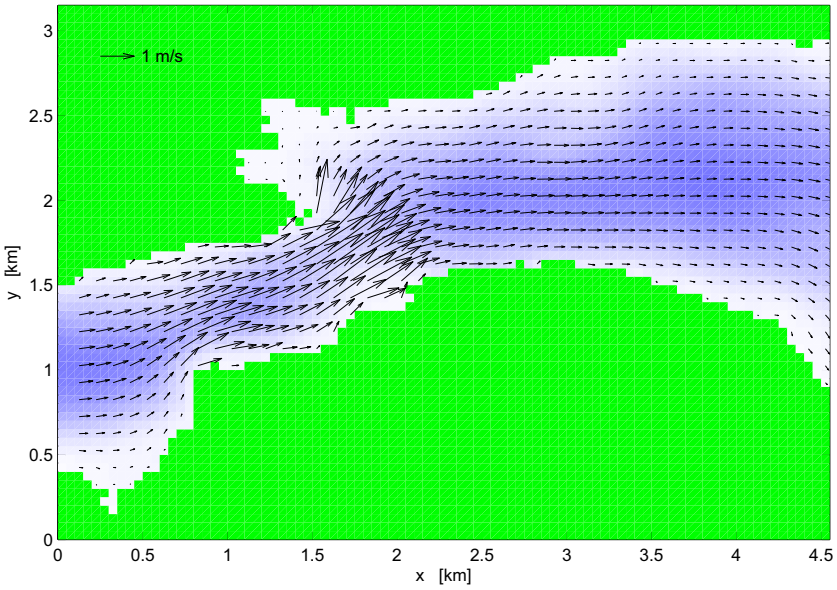

Figure 15: Case I: The total current (M_2-tide + surge) in Ballstad 15 December 2004 02:00 UT. Simulations without non-linear advective terms.

Table 1: Major and minor axis for the M_2 current ellipse and the main higher harmonics for 6 locations in Ballstadstraumen (B1-B6). The harmonic analyses are for a time interval of 3 M_2 cycles starting the 13 December at 18:00 UT. The orientation of the major axis (Θ) is relative east.

		Tide only			Total (Tide+Surge)		
Location Depth	Constituent	Major [cms^{-1}]	Minor [cms^{-1}]	Θ [deg]	Major [cms^{-1}]	Minor [cms^{-1}]	Θ [deg]
B1	M_2	92.4	-0.7	31.5	86.2	-1.8	34.9
6 m	M_4	5.0	-1.5	93.7	13.7	2.8	30.6
	M_6	10.1	0.6	27.7	2.6	-0.9	20.9
% of signal			99.8			83.3	
B2	M_2	78.3	-1.4	24.0	76.7	-2.1	25.3
22 m	M_4	8.2	-1.9	28.2	12.8	1.0	25.7
	M_6	9.8	1.1	20.9	2.7	-0.5	15.4
% of signal			99.6			83.9	
B3	M_2	15.8	0.5	33.7	22.7	1.9	31.6
8 m	M_4	10.9	2.0	28.9	8.9	1.4	28.1
	M_6	4.9	1.3	22.3	4.0	0.9	33.7
% of signal			97.1			61.5	
B4	M_2	15.5	-0.3	168.4	18.3	-1.3	165.6
12 m	M_4	3.3	-0.5	156.7	4.8	-1.2	170.7
	M_6	1.2	0.6	175.5	1.7	-0.2	169.7
% of signal			99.5			82.9	
B5	M_2	17.9	-0.4	166.2	16.4	-3.7	166.0
35 m	M_4	2.7	1.9	108.8	6.0	-1.0	178.3
	M_6	2.6	0.7	6.3	1.2	-0.5	39.1
% of signal			99.6			85.9	
B6	M_2	17.9	1.0	175.8	23.4	-2.9	165.4
47 m	M_4	1.6	-1.4	86.2	3.1	-0.4	111.6
	M_6	2.8	-1.1	97.6	1.7	0.2	128.7
% of signal			99.1			72.6	

T-Tide (Pawlowicz et al., 2002) for time intervals of 3 and 8 M_2 cycles. The time intervals have been chosen to cover the storm surge events. The analyses have been performed for simulations with boundary forcing from M_2-tide only and the combined effect of M_2-tide and storm surge, and for simulations both with and without the non-linear advective terms. Tables 1 and 2 give the major and minor axis of the current ellipse and the orientation, Θ, of the major axis for M_2 and the corresponding over-harmonic M_4 and M_6 recognized in the tidal current and the total current (tide+surge). To cover the period of eastward storm surge current (see Fig. 8), a time interval of 3 M_2 cycles starting 13 December 2004 at 18:00 UT (Case I) is chosen for the analyses presented in tables 1 and 2. The tables clearly show that the interaction between the tidal current and the storm surge current affects and change M_2 and the corresponding over-harmonics. We see that especially the over-harmonic components vary considerably from the tide only solution to the storm surge interacted solution. In addition there is a spatial variation in how much the tidal constituents are modified due to the storm surge.

For the locations in table 1 only about 60-80 % of the total current from the combined tide and storm surge forcing is recognized as tidal signal. At B1 and B2 the major axis of the M_2 component was reduced in the total current by the interaction with the storm surge current. At B1 (6 m depth) the major axis of M_2 was reduced with 6.2 cms^{-1} and at location B2 (22 m depth) a reduction of 1.6 cms^{-1} was found. B6 is located at deeper water in the middle of the channel (47 m). An increase in the M_2 component of 5.5 cms^{-1} was found at B6, while at B1 and B2, which are located in shallower water where the current is more energetic, the major axis of M_2 decreased. B3 is situated in the topographically trapped eddy on the northern side of the channel. The major axis of M_2 in the total current at B3 increased with 6.9 cms^{-1} in interaction with the storm surge current. The simulations without the non-linear advective terms show a decrease in M_2 in the total current for the three locations B1, B2 and B3 presented in table 2. In these simulations the two large eddies located respectively north and south of the main current jet do not appear (see Figs. 14 and 15), and hence the current has an eastward direction for locations B1-B3. The results discussed above show a spatial variation in interaction depending on the strength of the current and the depth at the location. There is a large difference in the modification of M_2 from B1 and B2 located in the narrowest and shallowest part of the channel to B3, within the eddy on the northern side of Ballstadstraumen, and B6 located in the deeper part of the channel. The quadratic bottom friction (Eq. 4) depends on the magnitude of the current and the depth, and the results discussed above suggest that the variation of bottom friction across the channel is an important factor for the interaction mechanism and the modification of the M_2 component in the total current.

The over-harmonic component M_4 increased in the total current for most of the locations. The increase was largest at shallow locations with strong current, e.g. location B1 (6 m depth) and B2 (22 m depth). At location B1 M_4 increased from 5.0 to 13.7 cms^{-1}, see table 1. There is also a considerable change in direction (Θ) of the major axis of M_4 of 57 deg at location B1. While there was an increase in M_4 for five of the six locations in table 1 there was a small decrease in M_4 at the location B3 (8 m) located in the eddy on the northern side of the channel. At location B5 within the eddy at the southern side of the channel there was an increase in M_4 and also a change in the orientation of the M_4 major axis of 69.5 deg (error estimate of 8.9 deg) which can be associated with the eastward motion and expansion of the eddy during the storm surge as discussed above. As found for the tidal M_2 constituent, a spatial variation of the effect of the tide-surge interaction

Table 2: Major and minor axis for the M_2 current ellipse and the main higher harmonics for 3 locations in Ballstadstraumen (B1-B3) for simulations without the non-linear advective terms. The harmonic analyses are for a time interval of 3 M_2 cycles starting the 13 December at 18:00 UT. The orientation of the major axis (Θ) is relative east.

		Tide only			Total (Tide+Surge)		
Location Depth	Constituent	Major [cms^{-1}]	Minor [cms^{-1}]	Θ [deg]	Major [cms^{-1}]	Minor [cms^{-1}]	Θ [deg]
B1	M_2	68.3	0.1	32.9	57.7	0.0	33.6
6 m	M_4	-	-	-	10.9	0.3	30.7
	M_6	5.1	0.2	24.8	1.6	0.0	37.3
% of signal			100.0			80.2	
B2	M_2	72.8	-0.2	24.6	61.7	-0.2	25.3
22 m	M_4	-	-	-	12.2	0.3	23.0
	M_6	6.8	0.3	21.1	1.8	0.1	27.5
% of signal			100.0			78.4	
B3	M_2	19.1	-0.6	21.8	16.9	-0.5	21.6
8 m	M_4	-	-	-	2.9	0.0	22.6
	M_6	1.4	0.0	23.6	0.3	0.0	14.8
% of signal			100.0			87.1	

was also found for the M_4 constituent. Spatial variations in the over-harmonics due to tide-surge interaction are also reported by Jones and Davies (2008).

The over-harmonic M_4 is not present in the simulation with tide only forcing without non-linear advective terms, but increases to about 10 cms^{-1} in the most energetic part of the current (i.e. locations B1 and B2) in simulations with tide+surge forcing (table 2). The absence of the M_4 component in the simulation with tide only forcing and without the non-linear advective terms confirms that the M_4 component is generated from the M_2 tide by non-linear interaction and that that the non-linear advective terms are essential, as pointed out by Jones and Davies (2008). Since the total current contains M_4 also in simulations without the non-linear advective terms, this suggest that there is some energy in the M_4 frequency band in the storm surge signal. Harmonic analysis of the estimated surge used as boundary input shows that indeed the surge signal contains some energy in the near M_4 band. Therefore the calculated M_4 amplitude is not only an effect of non-linear interaction. In order to avoid this an approach using a steady state surge as proposed by Jones and Davies (2008) would be preferable (see sec. 7).

The M_6 component decreases at all locations except B4 by the tide-surge interaction, at the latter there is a small increase (table 1). At B1 M_6 is reduced with 7.5 cms^{-1} from the tidal only to the total current, and at B2 a reduction of 7.1 cms^{-1} was found. A diurnal K_1 component was also recognized in both the storm surge current and the total current, an effect of the diurnal variation of the storm surge.

The error estimates from T-tide are quite small for the time series from simulations with tide only forcing, and larger for the time series from the total current. The error

estimate in the major axis for M_2 and the over-harmonic components was found to be 0.1-0.3 cms^{-1} for the tidal current and 0.6-1.8 cms^{-1} for the total current. The error estimate in the orientation of the major axis (Θ) varies for the different tidal constituents, smallest error for M_2 with 0.1-0.6 deg for the tidal current and 0.9-3.6 deg for the total current. The M_4 component contains an error estimate in Θ of 0.6-4.5 deg for most locations (17.5 deg at B6) for the tidal current, and 5.3-8.9 deg (13.2 deg at B6) for the total current. The over-harmonic M_6 contains the largest error estimates with 0.9-3.6 deg for the tidal current, and 11.9-33.7 deg (69.1 deg at B5) for the total current.

The harmonic analyses performed for a period of 8 M_2 cycles gives some different results in modification of the tidal current components by the tide-surge interaction than the analyses performed for a period of 3 M_2 cycles. For example the over-harmonic M_4 is less increased in analyses of time series of 8 M_2 cycles than for those of 3 M_2 cycles presented in table 1 at the shallow locations B1 and B2. The modification of M_2 is also different, and the largest difference is found at location B3 where the tide-surge interaction gives an increase of M_2 of 0.5 cms^{-1} for analyses of 8 M_2 cycles while an increase of 6.9 cms^{-1} for 3 M_2 cycles. The storm surge event that occur during 13-15 December 2004 introduce a storm surge current with an eastward direction in the beginning of the period and with a westward direction at the end of the period. To study the modification of the tidal current due to the tide-surge interaction of the storm surge current, the period of storm surge induced current in one direction should be analysed. Analyses of a longer period will give the mean effect of the storm surge current in both directions and hence give different result of the modification of the tidal current. We wanted to analyse the effect of eastward storm surge current and choose to present the analyses of the relative short time series from 13 Dec 2004 at 18:00 UT to 15 Dec 2004 07:15 (i.e. 3 M_2 cycles) with interaction of eastward storm surge current to the tidal current.

6 Comparison with field measurements

From November 2004 to March 2005 current measurements were executed with acoustic current meters (Aquadopp, from Nortek AS) by The Norwegian Defense Research Establishment at two locations, Steinslandsstraumen and Ballstadstraumen. The two stations are marked by St1 and St2 in Fig. 2, respectively. Measurements were made at two levels, 23 and 40 meters below surface at Steinslandstraumen and 22 and 30 meters below surface at Ballstadstraumen. In periods with strong currents, the pressure records, especially from Ballstadstraumen, indicate that the upper part of the rig has been bent down. The current data show a considerable amount of high frequency current oscillations both in strength and direction (station St2 is shown in Figs. 16 and 17). The periods of these oscillations are about 1 hour and shorter, and can not be related to any over-harmonic tidal oscillations. These short periodic oscillations represent a considerable amount of energy and partly contaminate the tidal oscillations. Whether these oscillations are physical or artificial due to the deflection of the rig has not been possible to determine. Earlier current measurements at station SK do not show the same amount of high frequency oscillations and the observed tidal current from station SK agrees much better with model predictions (see sec. 3).

Model simulations with observed sea level imposed at the open boundaries, extrapolated as described in sec. 2.1, have been performed for the period of the storm surge events (Case I and Case II) in order to compare model simulations with the current measurements. Figs. 16 and 17 show the simulated current and the observed current at station St2 in

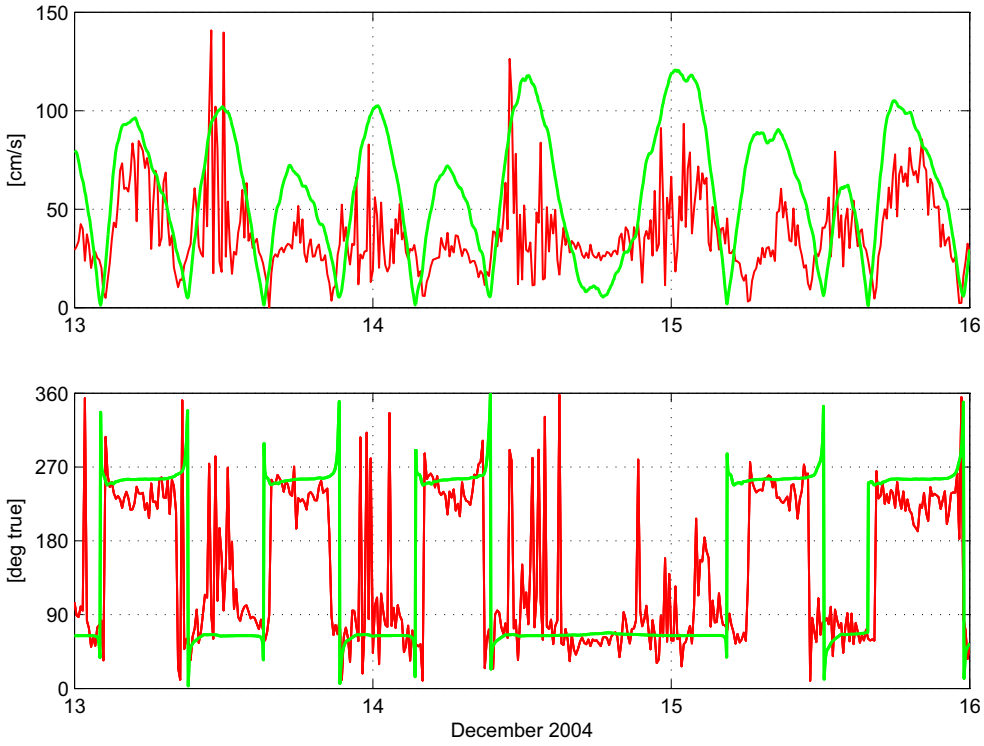

Figure 16: Case I: Comparison between modeled (green) and observed (red) current at station St2, in Ballstadstraumen. Upper panel: Current speed. Lower panel: Current direction (degree True).

Ballstadstraumen. Generally the model is able to reproduce the main features of the current variation, but the model over-predicts the current strength. For Case I (Fig. 16) the model predicts well the eastward current where the storm surge current dominates the tidal current on 14 December and prevent the reversal of the current. Similarly in Case II on 22 December (Fig. 17). For Case II on 23 December the model also shows that the period with westward current is prolonged compared to the tidal period in agreement with observations. The model does not show the high frequency oscillations which are dominant in the observations, but these oscillations may be due to mooring oscillations as discussed above.

7 Concluding remarks

This study demonstrates clearly the complex flow features of the tidal and the storm surge driven currents in a narrow channel connecting two separate fjord systems. Two storm surge events from December 2004 have been studied in details.

During the storm surge events the large scale external surge introduced an additional sea level difference between the northern and southern entrance of the Tjeldsund channel.

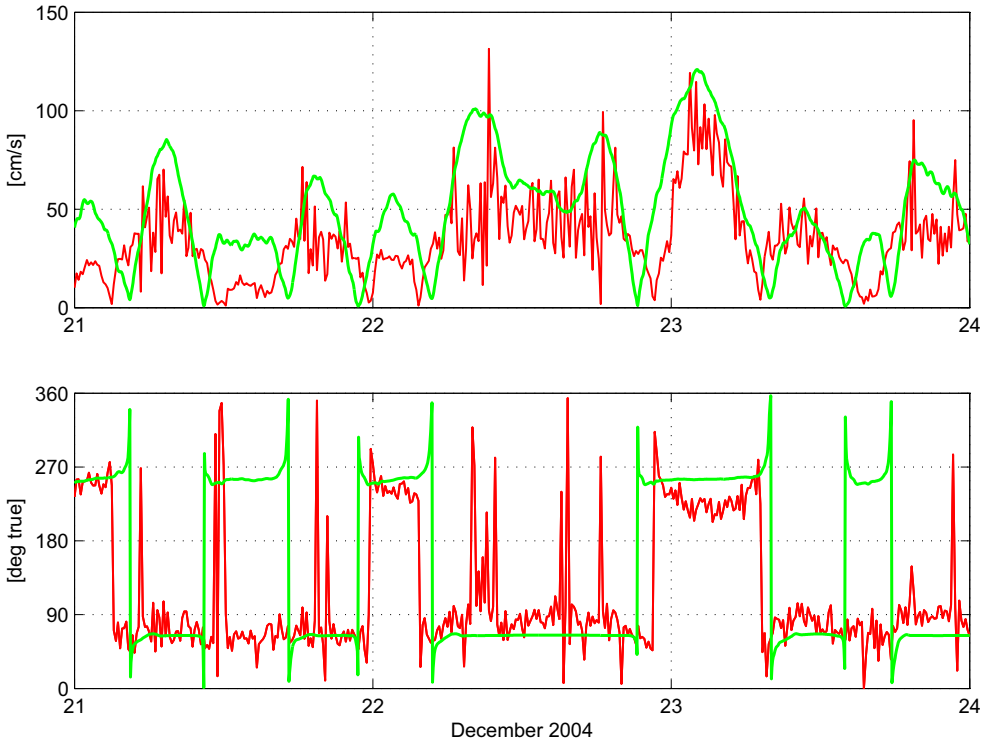

Figure 17: Case II : Comparison between modeled (green) and observed (red) current at station St2, in Ballstadstraumen 21-23 December 2004. Upper panel: Current speed. Lower panel: Current direction (degree True).

This lead to a storm surge current that was found to intensify or reduce the tidal current and also reverse the direction of the current. The non-linear interaction between the tide and the surge is evident in the mean tidal current and the mean storm surge current through a cross-section of the channel. For the mean current through the channel the non-linear bottom friction is found to be the main source of the tide-surge interaction. This is in accordance with the results by Prandle and Wolf (1978) and Tang et al. (1996).

Although the non-linear advective terms have minor influence on the interaction displayed by the mean current, they influence the eddy formation and flow separation and therefore locally have a strong effect on the over-harmonic current components, as also demonstrated by Jones and Davies (2008). They discuss the modification of M_2, M_4 and M_6 by the tide-surge interaction with different wind forcing in a very shallow area in the eastern Irish Sea. They found that there are significant non-linear effects which influence both the computed tidal elevation and tidal current distribution. In our experiments the non-linear advective terms are found to be important for the formation of eddies. The eddies that appear in simulations with the non-linear advective terms do not appear in simulations without these terms. The non-linear advective terms are also found to be important for the generation of the over-harmonic M_4 constituent. This was demonstrated by comparing the tide only forced current with and without the non-linear advective terms

where the M_4 constituent is not present in tidal simulations without the non-linear advective terms

Time series of the tide only forced current and the total current, forced by tide+surge at the open boundaries, from six locations in Ballstadstraumen have been harmonic analysed and compared. The analyses show that the tidal constituent M_2 and the corresponding over-harmonics are clearly modified during the storm surge by the interaction between the tidal current and the storm surge current. The analyses also show spatial variations in how much the tidal constituents are modified depending on the depth at the location and the strength of the current. Especially the results from the harmonic analyses suggest that the non-linear bottom friction is an important factor for the modification of the tidal M_2 component.

The over-harmonic components are calculated by harmonic analysis of relatively short time series including a transient storm surge of duration of about 24 hours. The harmonic analysis of the estimated surge used as boundary input shows that higher harmonics remain in the surge signal. Since this storm surge signal introduced in this way contains over-harmonics this may influence the calculations. A different approach would be to investigate a steady state situation similar to Jones and Davies (2008). This could be done by applying a constant sea level difference (corresponding to a storm surge) between the southern and northern entrances of the Tjeldsundet channel in addition to sea level difference due to tide. After a steady state has been attained harmonic analyses of the time series could be done in order to see how the over-harmonic components depend on the state of tide relative to the surge. So far we have not had time to do this, and have left it for a future investigation.

The study clearly shows that in a narrow and shallow channel like the Tjeldsund channel a tide-surge interaction will occur during storm surge events. The modification of the constituent M_2 and its over-harmonics shows that tide-surge interaction leads to modification of the tide. Consequently a "classical" de-tiding procedure will result in tidal energy being left in the surge signal as pointed out by Jones and Davies (2008). Hence when modeling the current during a storm surge event, it will be necessary to model the total current during the storm surge.

In this study we have forced the storm surge current in the channel system by the observed sea level difference between the ends of the channel and neglected the local wind stress and atmospheric pressure differences. Comparison with observations indicates that this approach is justified and may be useful for future modeling in similar cases.

Acknowledgment

The modeling work has been supported by The Norwegian Defense Research Establishment (FFI), Kjeller under a grant FFI-0352. FFI has in cooperation with The Norwegian Hydrographic Service (NHS), Stavanger, executed a field campaign for recoding current data. NHS provided depth matrix and sea level data both from permanent and temporary stations within the area.

References

Bobanovic, J., Thompson, K. R., Desjardins, S., and Ritchie, H. (2006). Forecasting storm surges along the east coast of Canada and the north-eastern United States: The storm of 21 january 2000. *Atmosphere-ocean*, 44(2):151–161.

Davies, A. M., Jones, J. E., and Xing, J. (1997a). Review of recent developments in tidal hydrodynamic modeling. 1: Spectral models. *Journal of Hydraulic Engineering*, 123(4):278–292.

Davies, A. M., Jones, J. E., and Xing, J. (1997b). Review of recent developments in tidal hydrodynamic modeling. 2: Turbulence energy models. *Journal of Hydraulic Engineering*, 123(4):293–302.

Gjevik, B., Hareide, D., Lynge, B. K., Ommundsen, A., Skailand, J., and Urheim, H. (2006). Implementation of high resolution tidal current fields in electronic charts systems. *Journal of Marine Geodesy*, 29(1):1–17.

Gjevik, B., Moe, H., and Ommundsen, A. (1997). Sources of the Maelstrom. *Nature*, 388(6645):837–838.

Hjelmervik, K., Lynge, B., Ommundsen, A., and Gjevik, B. (2009). Modelling of tides and storm surges in the Tjeldsund channel in northern Norway. *In PhD Thesis Hjelmervik: Wave-current interactions in coastal tidal currents. Faculty of Mathermatics and Natural Sciences, University of Oslo.*

Hjelmervik, K., Ommundsen, A., and Gjevik, B. (2005). Implementation of non-linear advection terms in a high resolution tidal model. Technical report, Preprint Series, No. 1, Dept. Math. University of Oslo, Norway, ISSN 0809-4403.

Hjelmervik, K. B. and Trulsen, K. (2009). Freak wave statistics on collinear currents. *Journal of Fluid Mechanics*, 637:267–284.

Horsburgh, K. J. and Wilson, C. (2007). Tide-surge interaction and its role in the distribution of surge residuals in the North Sea. *J. Geophys. Res.*, 112:C08003, doi:10.1029/2006JC004033.

Johns, B., Rao, A. D., DubeE, S. K., and Sinha, P. C. (1985). Numerical modeling of tide surge interaction in the Bay of Bengal. *Phil. Trans. Roy. Soc.London, Ser. A*, 313(1526):507–535.

Jones, J. E. and Davies, A. M. (2007). Influence of non-linear effects upon surge elevations along the west coast of Britain. *Ocean Dynamics*, 57(4-5):401–416.

Jones, J. E. and Davies, A. M. (2008). On the modification of tides in shallow water regions by wind effects. *Journal of Geophysical Research-oceans*, 113(C5):C05014, doi:10.1029/2007JC004310.

Martinsen, E. A. and Engedahl, H. (1987). Implementation and testing of a lateral boundary scheme as an open boundary-condition in a barotropic ocean model. *Coastal Engineering*, 11(5-6):603–627.

Mesinger, F. and Arakawa, A. (1976). Numerical methods used in atmospheric models. *Garp Publication Series No 17*, WMO-ICSU.

Moe, H., Ommundsen, A., and Gjevik, B. (2002). A high resolution tidal model for the area around The Lofoten Islands, northern Norway. *Continental Shelf Research*, 22(3):485–504.

Pawlowicz, R., Beardsley, B., and Lentz, S. (2002). Classical tidal harmonic analysis including error estimates in Matlab using T-TIDE. *Computers & Geosciences*, 28(8):929–937.

Prandle, D. and Wolf, J. (1978). The interaction of surge and tide in North sea and River Thames. *Geophys. J. R. astr. Soc.*, 55(1):203–216.

Smagorinsky, J. (1963). General circulation experiments with the primitive equations. *Monthly Weather Review*, 91(3):99–164.

Sutherland, G., Garrett, C., and Foreman, M. (2005). Tidal resonance in Juan de Fuca Strait and the Strait of Georgia. *Journal of Physical Oceanography*, 35(7):1279–1286.

Tang, Y. M., Grimshaw, R., Sanderson, B., and Holland, G. (1996). A numerical study of storm surges and tides, with application to the North Queensland coast. *Journal of Physical Oceanography*, 26(12):2700–2711.

Paper III

ADCP measurements off the Lofoten headland and comparison with high resolution tidal current models

ADCP measurements off the Lofoten headland and comparison with high resolution tidal current models

B. K. Lynge[1,2]

Abstract

Detailed measurements of the tidal current fields off the Lofoten headland have been executed with a ship-mounted Acoustic Doppler Current Profiler (ADCP) March 2009. Two numerical tidal models; a depth integrated model and a three dimensional model with horizontal grid resolution of 100 m have been used for comparison with the ADCP measurements

1 Introduction

In coastal areas with complex bottom topography and obstacles like shallow rocks and small islands the tidal current flow fields can exhibit large horizontal variations and small-scale flow features. Mapping of the spatial structures of the velocity field in these areas can be of considerable value for environmental purposes. Geyer and Signell (1990) used a shipboard Acoustic Doppler Current Profiler (ADCP) to measure the tidal flow around the headland Gay Head in Vineyard Sound, Massachusetts. Several studies have also been carried out with numerical models to study the dynamics and spatial structures of tidal current around headlands, e.g. Maddock and Pingree (1978); Pingree and Maddock (1979); Signell and Geyer (1991); Geyer (1993); Davies (1995).

During a survey with the research vessel G.O. Sars March 2009 detailed measurements were executed with a ADCP in the Moskstraumen Maelstrom off the Lofoten headland on the northern coast of Norway (Fig. 1). Measurements of the current have earlier been performed in the area at four locations with RCM current recorder, described in Moe et al. (2002), but no systematic measurements with ADCP are available from this area to establish the horizontal structures of the velocity field.

Moskstraumen is situated on the shallow ridge between the island Værøy and the Lofoten headland (Lofotodden), see Fig. 2. The shallow area contains a complex topography and numerous small islands and rocks. Tidal currents dominate wind driven currents in the area. The significant difference in tidal range in Vestfjorden and the shelf outside Lofoten combined with complex topography causes strong tidal currents running with total strength up to $5\,\mathrm{ms}^{-1}$ according to the Norwegian Hydrographic Service (NHS, 2001). No current records are available for estimates of these extremes.

Moskstraumen is well known for its strong currents and whirlpool, and the power and strength of the Maelstrom has inspired the authors Jules Verne and Edgar Allen Poe to fantasize the description of the energetic currents. A review of historical literature about the Maelstrom can be found in Gjevik et al. (1997) and Gjevik (1998). More modern studies describing the large-scale dynamics of the phenomenon can be found in Moe et al.

[1]Department of Mathematics, University of Oslo, P.O.Box 1053, Blindern, 0316 Oslo, Norway.
[2]The Norwegian Hydrographic Service, Stavanger, Norway.

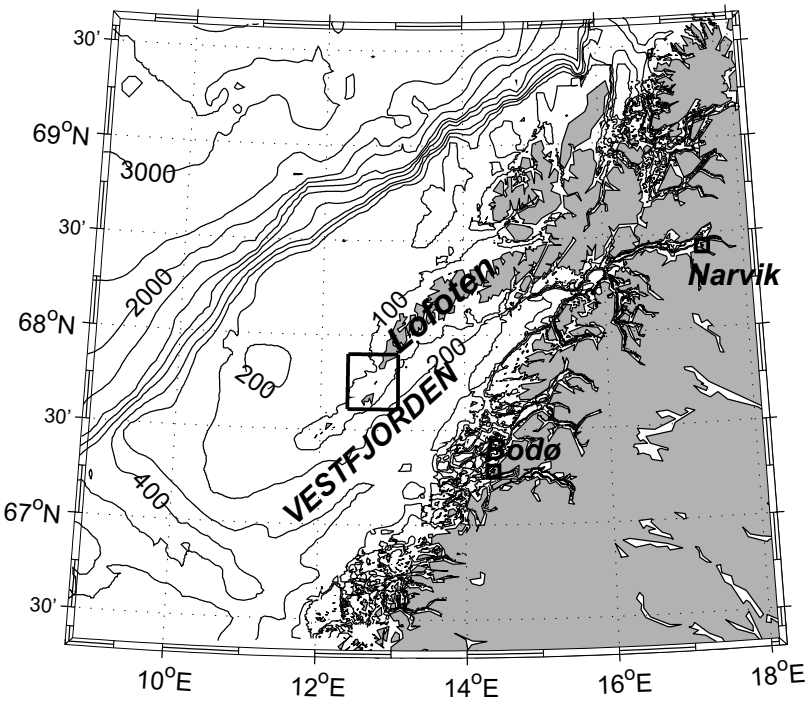

Figure 1: Location of the model domain on the northern coast of Norway. The model domain is marked with a square box in the Lofoten area. Contour lines show the bottom topography in the area with depth in meters.

(2002), where a depth integrated numerical model with grid resolution 500 m has been used for tidal simulations of Moskstraumen and the adjacent areas.

In order to study the horizontal structures of the flow field off the Lofoten headland, the ADCP measurements from the survey March 2009 have been compared to numerical simulations of the tidal flow through Moskstraumen. For the comparison presented in this report two numerical tidal models have been used for calculations of the flow field, a depth integrated model from the University of Oslo (Hjelmervik et al., 2005) and a three dimensional σ-coordinate model (Berntsen, 2004). The experiments are run with a horizontal grid resolution of 50 and 100 meters. Numerical simulations of the tidal current in the area reveal a complex flow field with small scale features and formation of eddies in the wake of the Lofoten headland and Mosken and the small islands north of Mosken. By applying two different tidal models for the area we are able to compare the models and study the consistency of the model predictions. The two models applied for these experiments both resolve the main features of the flow field as revealed by the ADCP measurements. For the small-scale dynamics of the flow field the simulated flow fields reveal some discrepancy between the two models, and also in comparison with the measurements. A comparison of the simulated flow fields with field measurements is important for the validation of the numerical models. The comparison can also be valuable for further model and observational studies of the dynamics of the flow field off the Lofoten headland.

2 Numerical models

Two ocean models have been applied in the present studies to investigate the tidal current in Moskstraumen. Experiments have been carried out with a depth integrated tidal model (University of Oslo) and a three dimensional σ-coordinate ocean model (Bergen Ocean Model).

2.1 Depth integrated tidal model

The depth integrated tidal model developed at the University of Oslo has earlier been used for several studies of tidal current, e.g. Gjevik et al. (1997), Moe et al. (2002), and Gjevik et al. (2006). Here we have applied an upgraded version of the model, described in Hjelmervik et al. (2005). The depth-integrated shallow water equations in a Cartesian coordinate system (x, y, z) with the x- and y-axis horizontal in the level of the undisturbed surface, are given by:

$$\frac{\partial \eta}{\partial t} = -\frac{\partial U}{\partial x} - \frac{\partial V}{\partial y} \tag{1}$$

$$\frac{\partial U}{\partial t} + \frac{\partial}{\partial x}\left(\frac{U^2}{H}\right) + \frac{\partial}{\partial y}\left(\frac{UV}{H}\right) - fV = -gH\frac{\partial \eta}{\partial x} + F^x + A^x \tag{2}$$

$$\frac{\partial V}{\partial t} + \frac{\partial}{\partial x}\left(\frac{UV}{H}\right) + \frac{\partial}{\partial y}\left(\frac{V^2}{H}\right) + fU = -gH\frac{\partial \eta}{\partial y} + F^y + A^y \tag{3}$$

where t is the time, (U, V) are the components of volume flux vector per unit length in the horizontal plane, η the vertical displacement of the sea surface from the mean sea level, $H = H_0 + \eta$ the total depth, H_0 the mean depth, g the acceleration of gravity, and f the Coriolis parameter. The bottom friction terms, F^x and F^y, are given by:

$$F^{x,y} = -c_D \frac{(U, V)}{H} \frac{\sqrt{U^2 + V^2}}{H} \tag{4}$$

where c_D is the drag coefficient of the quadratic bottom shear stress. The horizontal eddy viscosity terms, A^x and A^y, are parameterized by a simple Large Eddy Simulation (LES) model:

$$A^{x,y} = \nu \frac{\partial^2}{\partial x^2}(U, V) + \nu \frac{\partial^2}{\partial y^2}(U, V) \tag{5}$$

or

$$A^{x,y} = \frac{\partial}{\partial x}\left(\nu \frac{\partial}{\partial x}(U, V)\right) + \frac{\partial}{\partial y}\left(\nu \frac{\partial}{\partial y}(U, V)\right), \tag{6}$$

where ν is the eddy viscosity coefficient of the horizontal shear stress. For most of the simulations Eq. 6 has been used for calculations of the horizontal eddy viscosity. Tests have also been run with the expression in Eq. 5. The eddy viscosity coefficient is expressed according to Smagorinsky (1963), by:

$$\nu = ql^2 \left[\left(\frac{\partial \overline{u}}{\partial x}\right)^2 + \frac{1}{2}\left(\frac{\partial \overline{u}}{\partial y} + \frac{\partial \overline{v}}{\partial x}\right)^2 + \left(\frac{\partial \overline{v}}{\partial y}\right)^2 \right]^{\frac{1}{2}} \tag{7}$$

where q is a constant, l is a length scale which is set equal to the grid size, and $(\overline{u}, \overline{v})$ denote the components of the depth mean current velocity defined to the first order by:

$$\overline{u} = \frac{U}{H}, \qquad \overline{v} = \frac{V}{H}$$

With q=3.5, a grid size of 100 meters, and a current speed of the order 1 ms^{-1}, Eq. 7 leads to an eddy viscosity coefficient of the order 350 m^2s^{-1}.

The model equations 1–3 are discretized on a quadratic C-grid (Mesinger and Arakawa, 1976) with a finite difference numerical scheme centered in space and forwarded in time. The advection terms are estimated with an extrapolation routine for the grid points near the coastal boundaries in order to avoid one-sided differences. Further details on how the numerical scheme is designed and its performance for this particular application, can be found in Hjelmervik et al. (2005).

The CFL-stability criterion satisfied by the numerical time step, Δt, is:

$$\Delta t \leq \frac{\Delta x}{2\sqrt{2gH_{max}}}$$

where H_{max} is the maximum depth of the model domain.

2.1.1 Model setup

In order to check the sensitivity of the solutions to different values of the eddy viscosity coefficient (Eq. 7) and the bottom drag coefficient (Eq. 4) series of separate simulations have been performed, see sec. 5 for more details. In the experiments presented here we have used the parameter q=0.5 for calculations of the horizontal eddy viscosity with the expression in Eq. 5, and q=3.5 for calculations with the expression in Eq. 6, in order to ensure stability. The latter choise of q is similiar with that used for C_{h2d} in the Bergen Ocean Model, see below (sec. 2.2.1). In the shallowest areas of the model domain we had difficulties in achieving stability with the chosen values of q. According to Crean et al. (1988) the bottom shear stress dominates the horizontal eddy viscosity near the coast. Instead of increasing the eddy viscosity coefficient we, like described in Hjelmervik et al. (2005), have increased the bottom shear stress in the shallow coastal area by assuming a drag coefficient dependent on the depth:

$$c_D = c_D^0\left(1 + ae^{\frac{H^2}{H_m^2}}\right) \tag{8}$$

where H is the water depth, H_m is a characteristic water depth in the coastal zone, c_D^0=0.005 is the value of the coefficient in deep water ($H \gg H_m$), and a is a positive scaling factor greater than unity. In these experiments a suitable value of a was found to be $a = 5.0$ to ensure stability.

All simulations started from rest (U, V and η equal zero) with increasing boundary forcing in time according to a ramping function, $(1 - \exp(-\sigma t))$. A value of $\sigma = 4.6 \times 10^{-5}s^{-1}$ has been used. This implies full driving effect of the boundary conditions after about 12 hours.

A 24 hours spin up time is found to be sufficient to obtain an acceptable steady state. After 48 hours, complete fields for current and elevation data are stored every hour. Data for surface elevation, current strength and direction from selected stations (grid nodes) were stored with 180 s sampling for later processing.

2.2 Bergen Ocean Model -a σ-coordinate model

The other model applied in the present studies is a three dimensional (x, y, z) σ-coordinate ocean model (Bergen Ocean Model) described in Berntsen (2004) where x and y are the horizontal Cartesian coordinates and z the vertical coordinate. The model applies the Boussinesq approximation and is here applied in a hydrostatic form. The model code is

available from www.math.uib.no/BOM/. The model has recently been used for idealized studies of internal wave generation and mixing of flow over sills (Berntsen et al., 2008, 2009), and studies of dispersion due to tidal flow in Moskstraumen (Lynge et al., 2010). The governing equations are:

The continuity equation,

$$\vec{\nabla} \cdot \vec{u} + \frac{\partial w}{\partial z} = 0, \tag{9}$$

and the Reynolds momentum equations,

$$\frac{\partial u}{\partial t} + \vec{u} \cdot \vec{\nabla} u + w\frac{\partial u}{\partial z} - fv = -\frac{1}{\rho_0}\frac{\partial p}{\partial x} + \frac{\partial}{\partial z}(A_v \frac{\partial u}{\partial z}) + F_x, \tag{10}$$

$$\frac{\partial v}{\partial t} + \vec{u} \cdot \vec{\nabla} v + w\frac{\partial v}{\partial z} + fu = -\frac{1}{\rho_0}\frac{\partial p}{\partial y} + \frac{\partial}{\partial z}(A_v \frac{\partial v}{\partial z}) + F_y, \tag{11}$$

$$\rho g = -\frac{\partial p}{\partial z}. \tag{12}$$

In the equations above $\vec{u} = (u, v)$ is the horizontal velocity field, w the vertical velocity, t the time, f Coriolis parameter, g is gravity, ρ is the density, ρ_0 is the reference density, p is pressure, and A_v vertical eddy viscosity. The conservation equations for temperature T and salinity S is given by

$$\frac{\partial (T,S)}{\partial t} + \vec{u} \cdot \vec{\nabla}(T,S) + w\frac{\partial (T,S)}{\partial z} = \frac{\partial}{\partial z}(K_v \frac{\partial (T,S)}{\partial z}) + F_{T,S}, \tag{13}$$

where K_v is the vertical eddy diffusivity. The horizontal eddy viscosity terms F_x and F_y and the horizontal diffusivity terms F_T and F_S are given by

$$F_{x,y} = \frac{\partial}{\partial x}(A_h \frac{\partial (u,v)}{\partial x}) + \frac{\partial}{\partial y}(A_h \frac{\partial (u,v)}{\partial y}), \tag{14}$$

$$F_{S,T} = \frac{\partial}{\partial x}(K_h \frac{\partial (S,T)}{\partial x}) + \frac{\partial}{\partial y}(K_h \frac{\partial (S,T)}{\partial y}), \tag{15}$$

where A_h is the horizontal eddy viscosity and K_h the horizontal diffusivity. The horizontal eddy viscosity terms F_x and F_y can also be given by the formulation found in Mellor and Blumberg (1985); Mellor et al. (1998); Mellor (2004). The routine gives unstable solutions for the experiments carried out for this report and was applied only for test simulations.

The total pressure P is given by the pressure due to the free surface elevation η and the internal pressure, $P = g\rho_0\eta + g\int_z^0 \rho(\acute{z})d\acute{z}$. The internal pressure is neglected for simulations with homogeneous conditions.

The variables are discretized on a C-grid. In the vertical, the standard σ-transformation, $\sigma = \frac{z-\eta}{H+\eta}$, where H is the bottom depth, is applied. For advection of momentum and density a Total Variance Diminishing (TVD)-scheme with a superbee limiter described in Yang and Przekwas (1992) is applied in the present studies. The standard second order Princeton Ocean Model (POM) method is applied to estimate the internal pressure gradients (Blumberg and Mellor, 1987; Mellor, 1996). The model is mode split with a method similar to the splitting described in Berntsen et al. (1981) and Kowalik and Murty (1993).

The time steps are performed with a predictor-corrector method both in the internal time steps and in the external time steps. The leapfrog method is used as the predictor and the fully implicit method is used as the corrector.

2.2.1 Model setup

The experiments are performed with constant values of vertical eddy viscosity $A_v = 2 \cdot 10^{-3}\,\mathrm{m^2\,s^{-1}}$ and vertical eddy diffusivity $K_v = 10^{-7}\,\mathrm{m^2\,s^{-1}}$. The horizontal eddy viscosity A_h is computed according to Smagorinsky (1963), by

$$A_h = C_h \Delta x \Delta y \frac{1}{2}\left[(\frac{\partial u}{\partial x})^2 + \frac{1}{2}(\frac{\partial v}{\partial x} + \frac{\partial u}{\partial y})^2 + (\frac{\partial v}{\partial y})^2\right]^{\frac{1}{2}}, \tag{16}$$

where C_h is a constant. In the mode split model, the horizontal velocity components u and v are split according to $u = \bar{u} + u'$ and $v = \bar{v} + v'$ where $\bar{u}$ and $\bar{v}$ are the depth averaged values and u' and v' the corresponding deviations. The viscosity A_h is acting on u' and v'. The same expression as (16), with $\bar{u}$ and $\bar{v}$ replacing u and v and C_{h2d} replacing C_h, is used to compute the horizontal eddy viscosity A_{h2d} acting on the $\bar{u}$ and $\bar{v}$. In our experiments $C_h = 0.25$ and $C_{h2d} = 2.0$. The coefficients C_{h2d} acting on the depth averaged flow need to be larger than C_h due to the strong tidal inflow which primarily forces the depth averaged velocity components. The horizontal diffusivity K_h is chosen to be zero, see the discussion below.

In studies like the present, unique optimal values of the viscosities and diffusivities may not be obtained. However, there are some general guidelines that we have tried to follow. For instance, the values must be large enough to filter out the grid scale noise and at the same time small enough to allow a best possible representation of the physical processes with the chosen grid size. The horizontal viscosity may be related to the horizontal shear and this is often achieved by using some version of the Smagorinsky scheme given above, see also Haidvogel and Beckmann (1999). To allow the representation of internal motion, the diffusivities are kept at a minimum level or zero. The mixing then becomes primarily controlled by the mixing associated with the TVD-scheme. The vertical viscosity is often computed with the Mellor and Yamada (1982) scheme or some other Richardson number dependent scheme. With the grid sizes used here, the vertical velocity shear may become strong. The Richardson numbers may accordingly become smaller than the critical value and the mixing may become excessive even if the grid size is too coarse to represent overturning. A small and constant value of A_v is accordingly chosen in our experiments. It may also be noted that in experiments like the present the numerical viscosity and diffusivity may be substantial and of the same order of magnitude as the specified values, see Burchard and Rennau (2008) and Rennau and Burchard (2009). For further discussions see Xing and Davies (2006), Berntsen et al. (2008), and Berntsen et al. (2009).

In the experiments, the bottom stress vector $\vec{\tau_b}(x,t)$ is specified by

$$\vec{\tau_b}(x,t) = \rho_0 C_D \sqrt{u_b^2 + v_b^2}\,\vec{u_b}(x,t), \tag{17}$$

where $\vec{u_b} = (u_b, v_b)$ and u_b and v_b are the velocity components in the lowermost grid cells in the x and y direction respectively. The drag coefficient C_D is given by

$$C_D = \max[0.0025, \frac{\kappa^2}{(ln(z_b/z_0))^2}], \tag{18}$$

where z_b is the distance of the nearest grid point to the bottom. The von Karman constant κ is 0.4 and the bottom roughness parameter is chosen to be $z_0 = 0.01\,\mathrm{m}$, see Blumberg and Mellor (1987).

There is no flow through the sea bed or the closed lateral boundaries. Free slip boundary conditions are applied at the lateral boundaries in computing the non-linear momentum advection term. Initially the water elevation is zero, and there is no flow.

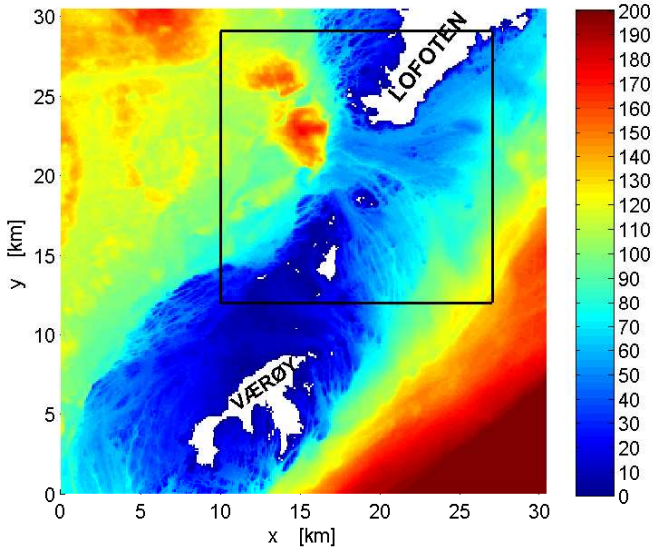

Figure 2: Bottom topography for the model area with the island Værøy in southwest, the headland of Lofoten in the north and the island Mosken in between. The domain marked with a square is used for presentation of flow fields in Figs. 6 -11. Colour bar is depth in meters.

Horizontally the grid applied is equidistant. In the vertical five equidistant σ-layers are used in the experiments. In the experiments the internal time step used is 6 seconds, and 30 external time steps are used for each internal step. The simulations presented here are carried out with homogenous conditions. The Coriolis frequency f is equal to $1.3 \cdot 10^{-4}$ s^{-1}.

2.3 Model setup and boundary conditions

The numerical models have been set up for the domain depicted in Figs. 1 and 2. The domain cover Moskstraumen with the headland of Lofoten in the northern part of the domain and the island Værøy in the southern part. The total extent of the domain is 30.5×30.5 km. The southwesterly corner of the domain has coordinates $x = 388500$ and $y = 7502000$ (given to WGS84-UTM zone 33). The coordinate axis (x, y) are orientated west-east and south-north respectively. The domain has four open boundaries.

High resolution bottom topography based mainly on multibeam bathymetric data from Norwegian Hydrographic Service (NHS) is used to generate the bottom matrices. The topography is shown in Fig. 2. Depths are related to Mean Sea Level (MSL) which differs from Chart Datum (CD) as used in nautical charts, and depths are mapped to datum WGS84-UTM zone 33. Horizontally, the grids applied are equidistant and the experiments are run with horizontal grid size $\Delta x = \Delta y$ equal to 50 and 100 meters.

As a driving force tidal elevation is forced into the model domain through the open boundaries. Amplitude and phase interpolated from a 500 m grid from Moe et al. (2002) are specified in every grid cell at the boundaries, and the tidal elevation is calculated and given for every time step. The tidal elevation is mainly represented by the two main semi-diurnal constituents M_2 and S_2. Simulations have also been carried out with the addition

of the elliptical-lunar constituent N_2 and the main diurnal constituent K_1.

At the open boundaries the flow relaxation scheme (*FRS*) (Martinsen and Engedahl, 1987) has been used to impose the boundary conditions. In the flow relaxation zone the surface elevation is updated in every time step according to

$$\phi = (1 - \alpha)\phi_{int} + \alpha\phi_{ext}, \tag{19}$$

where ϕ_{int} contains the unrelaxed values computed by the model, and ϕ_{ext} is a specified external value. The relaxation parameter α varies smoothly from 1 at the open boundary to 0 at the innermost cell of the boundary zone, see Martinsen and Engedahl (1987). The rationale behind this scheme is to soften the transition from an exterior solution to an interior solution by use of a grid zone where the two solutions dominate at each ends respectively. The width of the zone is taken to be ten grid cells in the experiments presented here.

3 Field measurements

A survey was carried out with the research vessel G.O. Sars (Institute of Marine Research, Bergen, Norway) the 14. March 2009 during a spring tide in the area off the Lofoten headland. Current measurements were performed using a ship-mounted broadband 150 kHz ADCP (Acoustic Doppler Current Profiler, RD-Instruments – http://www.rdinstruments.com/surveyor.aspx). RDI's data acquisition software VmDas (RD-Instruments, 2004) was used for data collection, and data were displayed and exported by the RDI software WinADCP (RD-Instruments, 2001). The ADCP was configured to record vertical structures of currents with a vertical resolution of 6 m (bin size 6 m). The first bin starts at 13.3 m depth and the maximum depth range was 193.3 m (i.e. 30 bins). The instrument transmitted data to a shipboard computer every 2 second, and the acquisition program made 1 and 5 minute averages of the velocity data. Bottom tracking was used to measure the ship's velocity relative to the bottom. The ship's speed during the survey varied between 2.0 and 3.5 ms^{-1}, and hence the horizontal spatial resolution of the velocity profiles varied between 120 and 210 m for the 1 minute averages, and between 600 and 1050 m for the 5 minutes averages. The weather conditions during the survey were calm, with air pressure of about 1010 hPa and wind speed of about 3 ms^{-1}.

The ADCP measurements were made along 12 sections in Moskstraumen starting at location A at 14:55 (UT) and ending at location C_1 at 23:29 (UT) (Fig. 5). The measurements contain a strong reflection signal from the bottom which dominates the measured values in the bins closest to the bottom. The measurements closest to the bottom thereby contain unrealistic values and have been removed from the data.

CTD measurements were taken with a CTD - SBE-911plus at two locations, C_1 in the western part of Moskstraumen and C_3 in the eastern part of Moskstraumen, see Fig. 3. CTD measurements were also planned at location C_2, but could not be carried out due to strong current. Profiles of salinity, temperature and density from stations C_1 and C_3 are shown in Fig. 4. The CTD profile at station C_1 was taken at 19:11 (UT) (about 40 minutes before low water) and shows a well mixed water column. At the time the recording was made the current was about to turn eastward. The CTD profile at station C_3 was taken at 20:47 (UT) (about one hour after low water), at time with strong eastward current. There is a weak stratification at station C_3. The profiles at C_3 show less saline water and lower temperature than at station C_1, especially in the upper layer. At the bottom layer the salinity and temperature at C_3 are comparable to those at station C_1.

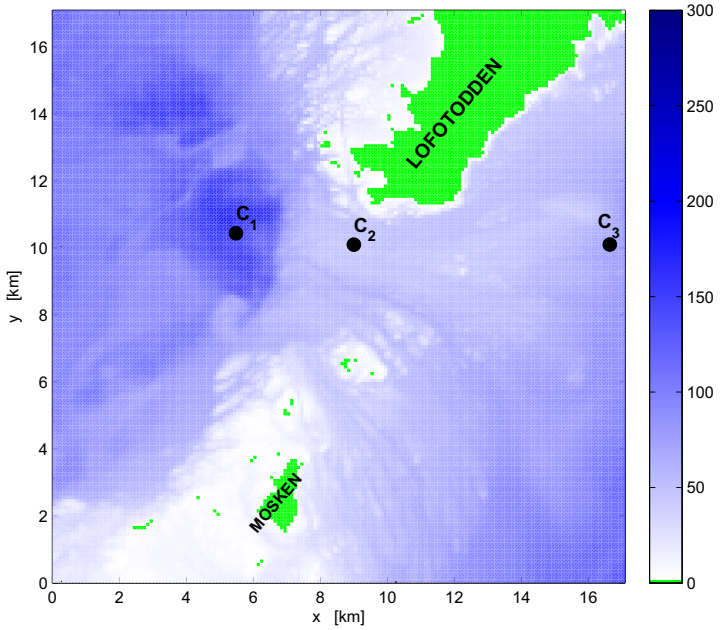

Figure 3: Bottom topography for the area of Moskstraumen presented in Figs. 6 -11. The Lofoten headland (Lofotodden) in the north and the island Mosken in the south of the domain. Position for CTD stations C_1-C_3 are marked. Colour bar is depth in meters.

4 ADCP measurements

4.1 Comparison of ADCP-data and modeled flow fields

Model simulations have been performed with the two numerical models described in sec. 2 for the area of Moskstraumen in the sound between the headland of Lofoten and the islands Mosken and Værøy for the same period as the survey 14 March 2009. For comparison with the model simulations the 1 minute averages from the current recordings are vertically averaged over the number of bins recorded in the 1 minute averaged value. The depth averaged current from the ADCP measurements are presented in Figs. 6 -11 c and d together with the corresponding flow fields from the depth integrated model (Figs. 6 -11 a and b) and the depth integrated current from the σ-coordinate model (Figs. 6 -11 e and f). The model simulations presented are run with a horizontal grid resolution of 100 m and the tidal constituents M_2 and S_2 are used for the boundary forcing (sec. 2.3). Current fields from the models are stored every hour, and the flow fields presented are chosen to make the best correspondence in time with the observations. The flow fields are presented in the 17×17 km area shown in Fig. 3, and the flow is given for every fifth grid cell. Hence the comparisons are made between simulated flow fields with a horizontal resolution of 500 m and ADCP measurements with a horizontal resolution of 120 to 210 m depending on the speed of the vessel. The maximum flow through the sound is from tidal simulations expected to occur about 1 hour and 15 minutes after time of High- and Low Water, see table 2 and 3, and sec. 5 for more details.

The first observations taken from A to B (Fig. 6 c) show northward and northeastward

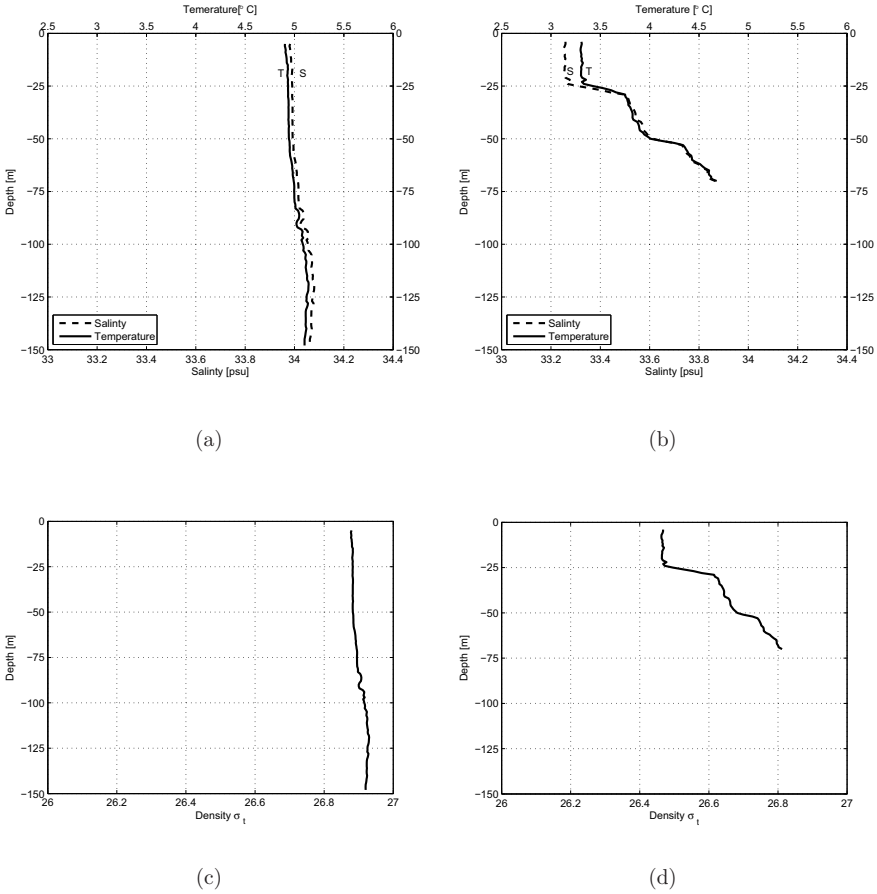

Figure 4: Salinity (- -) and temperature (–) from CTD stations a) C_1 and b) C_3 taken during survey with G.O. Sars 14. March 2009. Corresponding density profiles at c) station C_1 and d) station C_3.

current along the section, like also shown in the flow fields from both models at 15:00 (UT) and 16:00 (UT). In the northern part of the section, close to the Lofoten headland, the observed depth averaged current had a weak northwesterly direction while the flow fields from the two models depict a weak southwesterly direction of the current. The two models seam to underestimate the current speed at the time of the measurements.

At section B-C_1 (Fig. 6 d) the observations show a strong westward current. The current was most energetic in the middle of the sound and had a northwesterly direction at the western part of the section. The flow fields from the models at 16:00 (UT) capture these features.

In section C_1-D (Fig. 7 c) there was a strong northwestward current in the southern part of the section. In the northern part of the section the strength of the current was less intense, and following the section from south to north we see that the current changed direction from northwestward through southwestward to southeastward and finally southward at location D. Both the numerical models show two eddies west of the Lofoten headland in the flow fields at 17:00 (UT), one on the northern side of the westward jet through

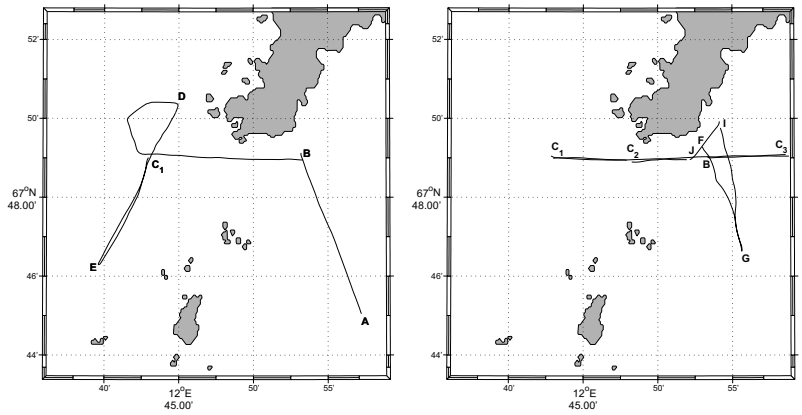

(a) (b)

Figure 5: ADCP measurements where made along 12 sections the 14 March 2009 starting at A at 14:55 (Ut) and ending at C_1 at 22:39 (UT). Sections A-B, B-C_1, C_1-D, D-E, and E-C_1 are shown in Fig. a, and sections C_1-C_2, C_2-C_3, C_3-B, F-G, G-I, I-J, and J-C_1 are shown in Fig. b.

the sound and one on the southern side, but there is a large discrepancy between the two models in extension of the northern eddy. The observation of southward current in the northeastern part of the section confirms the modeled southward current associated with the northern eddy in both the numerical models. The information from the measurements made in section C_1-D and the model simulations indicate that there is an eddy west of the Lofoten headland on the northern side of the jet when the main jet through the sound is westward. For further information about the extension of the eddy several ADCP measurements are required.

Section D-E (Fig. 7 d) shows southward current at location D as also depicted in the model simulations at 17:00 and 18:00 (UT) (Fig. 7). Following the section southward, we see that the current turned west, northwest, north, northeast, and finally east at location E. The flow fields at 18:00 (UT) show that the main flow through the sound was about to turn eastward, while there still was a westward jet in the western part of the sound. The eddies on the northern and southern side of the main westerly jet are also revealed in the flow fields at 18:00 (UT) for simulations with both models. The change in direction seen in the ADCP data from westerly to easterly current can be associated with the southern eddy in the simulated flow fields. The flow fields from both models show northeastward current at location E while the observations show a more eastern direction. West of the section the simulated flow field from BOM (Fig. 7 f) shows a more eastern direction.

In section E-C_1 (Fig. 8 c) the measured mean current was eastward at E and became stronger and more northeastward further north in the section. At location C_1 the current had a northwesterly direction. The modeled flow fields at 19:00 (UT) show that the flow through Mokstraumen had turned eastward at the time of the observation, while the two eddies depicted in the flow fields at 17:00 and 18:00 (UT) (Fig. 7) still where present west of the sound. The northern part of the ADCP section is located inside the simulated southern eddy. The observed northwestward direction of the current at C_1 can be associated with the northwestward current in the northern part of the southern eddy, though the location

of the northwestward current is not consistent in the two models and the observation.

Section C_1-C_2 was taken from west to east from 19:23 (UT) to 19:44 (UT) (Fig. 8 d). The current was northward in the western part of the section and strongly eastward in the eastern part of the section. At location C_2 the current was measured to about 1.5 ms^{-1}. The northward current observed in the western part of the section can be associated with the northward current in the southern eddy depicted in the flow fields at 19:00 (UT) (Figs. 8 a and e). The strong eastward current in the eastern part of the section is captured in both models at 20:00 (UT) (Figs. 8 b and f), but the models seam to underestimate the velocity of the current.

In section C_2-C_3 (Fig. 9 c) the measurements show strong eastward current with strength of up to 1.5 ms^{-1} in the western part of the section, and weaker eastward current east in the section at location C_3. The simulated flow fields at 20:00 (UT) capture the strong eastward current. Flow fields at 21:00 (UT) show stronger current and might be closer to the observations made from 19:52 to 20:40 (UT).

In section C_3-B (Fig. 9 d) the ADCP measurements show southeastward current at location C_3 east in the section, and strong eastward current in the western part of the section. Neither of the simulated flow fields show southeastward current at C_3 at 21:00 (UT), but both shows strong eastward current at B, and less intense towards C_3.

Section F-G was taken from north to south from 21:31 to 22:00 (UT) (Fig. 10 c). The current was mostly eastward and southeastward along the section as captured in the model simulations at 21:00 (UT) and 22:00 (UT), though the models seam to underestimate the strength of the current somewhat. At longitude about N 67°48.5' the current was reduced and the direction was more southerly than the samples before and after. West of this sample there is a shallow rock called Herjeskallen with depth 9.6 m (H in Fig. 10 c and d). The change in the current east of Herjeskallen is most likely caused by this shallow rock. The observed change in direction of the current can not be seen in the model simulations. The shallow rock is not properly resolved in the depth matrix where the grid cell closest to Herjeskallen has a depth of 18.9 m, and can be one explanation of why this change in direction is not captured in the modeled flow fields. At location G the measured current was eastward, while it is southeastward in the model simulations.

Section G-I (Fig. 10 d) from south to north shows a northeastward current at G. The observed current turned northward and southeastward just north of location G before getting a weak southeastern direction further north. The models capture the main east- and southeastward flow. The model simulations at 21:00 and 22:00 (UT) reveal eddies east of the island Mosken and the small islands north of Mosken (Figs. 10). The features are different in the flow fields from the two numerical models, and neither of them capture the observed northeast going current at location G. The shallow rocks called Svarvskallan (S in Fig. 10 c and d) with depths 2-4 m are located north of the group of small islands north of Mosken. These rocks are not properly resolved in the depth matrix where grid cells are about 20-30 m in the area where the rocks are located. The observed northeastward current north of location G during the survey suggest a non-linearity in the flow field which can be associated with the eddy formation east of the group of small islands and the Svarvskallen rocks revealed by the numerical models. The numerical models are with the model setup and grid resolution applied in the experiments not able to capture these features properly.

As also measured in the south going section (F-G) there was a change in the current east of Herjeskallen (H) in the measured vertically averaged current in the north going section (G-I). The current was weaker east of H than the samples before and after. The modeled flow fields do not capture this change. In the northern part of the section the observed current turned southward and had a southwesterly direction along the Lofoten headland at location I, while there was still quite strong eastward current through Moskstraumen

(Fig 10 d). In section I-J the measurements also show southwestward and southward current along the Lofoten headland while there still was an eastward current at location J (Figs. 11 c and 12 b). The modeled flow fields at 22:00 and 23:00 (UT) (Figs. 10 b and f and 11 a and e) show an eddy east of the Lofoten headland. Again there is a discrepancy in extension of the eddy between the two models. The observed southward and southwestward current confirm the south going current along the headland associated with the modeled eddy east of the headland. The observed eastward flow at location J is also captured in the modeled flow fields at 23:00 (UT).

At section J-C_1 (Fig. 11 d) from east to west the observed current was southeasterly at the eastern part of the section and was measured southward and weaker at the western part of the section. The simulated flow fields at 23:00 and 00:00 (UT) capture the main feature of the observed current (Fig. 11). The southward current observed at the western part of the section confirms the southern current captured in both models.

4.2 Cross sections of ADCP measurements

In the previous section we have studied the horizontal structures of the flow field by comparing the depth averaged ADCP measured current with simulated tidal flow fields. In the following the vertical structures of the measured current will be presented for some of the sections. The vertical structures of the magnitude of the current are shown in the cross sections shown in Figs. 13 and 14 for section B-C_1, C_1-C_2, C_2-C_3, and C_3-B. At the time section B-C_1 was taken the current had a westward direction (Fig. 6). Fig. 13 a shows that the current speed was quite uniform through the depth except at the location with maximum speed. Maximum speed of 1.7 ms^{-1} was observed in the upper layer on the western part of the shallow area of the sound.

At the time section C_1-C_2, C_2-C_2, and C_1-B was taken the current was mostly eastward. The current had just turned eastward in the sound when starting the section at location C_1, while the flow was northward at the western part of the section, see sec. 4.1 and Figs. 8 and 9. The cross sections of section C_1-C_2 and C_2-C_3 (Fig. 13 b and c) show that the current was at its strongest in the shallowest part of the sound at the eastern part of section C_1-C_2 and the western part of section C_2-C_3 with speed up to 1.5 ms^{-1}. At the eastern part of section C_2-C_3 the current speed was larger in the deeper layer than in the upper layer. This can indicate that the east going current flow under the less dense water in Vestfjorden. This is also indicated in the density profile at station C_3 (Fig. 4) where there was a weak stratification and where the bottom water has about the same density as at station C_1 on the western side of the sound.

During the survey of section C_2-C_3 the ship passed location B at 20:11 (UT) and the current speed was measured to about 1.1 ms^{-1} (Fig. 13 c). The cross section from C_3 to B (Fig. 14) shows that the current speed at the western part of the section intesified to 1.5 ms^{-1} near location B about one hour later (21:20 (UT)). The current speed at location B was largest in the upper layer, while in the eastern part of section C_3-B the current speed was still largest in the deepest layer.

5 Sensitivity study of the tidal models

In order to investigate the sensitivity of the numerical models a number of different simulations have been performed. For the depth integrated model (sec. 2.1) a systematic study of the sensitivity of the model due to different parameters have been performed. The results are presented in this section. Several simulations have also been run for the σ-coordinate

Table 1: Parameter choices for sensitivity tests. Experiments where carried out with a varying c_D while keeping a fixed value for q, with a varying value of q while keeping c_D fixed, and with different numbers of tidal constituents included as boundary forcing. The horizontal eddy viscosity terms ($A^{x,y}$) have been calculated either with the expression in Eq. 5 or Eq. 6.

Run number	c_D	q	*Tidal constituents*	$A^{x,y}$
1	0.003*	3.5	$M_2 + S_2$	Eq. 6
2	0.004	3.5	$M_2 + S_2$	Eq. 6
3	0.005	3.5	$M_2 + S_2$	Eq. 6
4	0.0075	3.5	$M_2 + S_2$	Eq. 6
5	0.01	3.5	$M_2 + S_2$	Eq. 6
6	0.005	3.0*	$M_2 + S_2$	Eq. 6
7	0.005	5.0	$M_2 + S_2$	Eq. 6
8	0.005	10.0	$M_2 + S_2$	Eq. 6
9	0.005	3.5	M_2	Eq. 6
10	0.005	3.5	$M_2 + S_2 + N_2 + K_1$	Eq. 6
11	0.005	0.5	$M_2 + S_2$	Eq. 5

* gives unstable solution

model (BOM - sec 2.2) in order to test different choices of parameters and settings. A systematic sensitivity study has not been performed for BOM for this report, but the test simulations carried out show similar behavior as for the depth integrated model.

The sensitivity of eddy formation and strength of the current to bottom friction and horizontal eddy viscosity has been investigated respectively by running the depth integrated model with different values of the bottom drag coefficient c_D (Eq. 4), and different values of the constant q (Eq. 7) in calculations of the horizontal eddy viscosity coefficient. The simulations have mainly been made with elevation from the two main semi-diurnal tidal constituents M_2 and S_2 as boundary forcing. In addition we have included the effect of the main diurnal constituent K_1 and the elliptical-lunar constituent N_2 during the spring tide 14 March 2009 for comparison. Simulations have also been performed with only the main semi-diurnal M_2. The parameters for the simulations presented in this report are given in table 1. For the comparison of model simulations with ADCP measurements in sec. 4.1 run number 3 in table 1 was used.

For calculations of the horizontal shear stress the horizontal eddy viscosity terms A^x and A^y are parameterized by a simple Large Eddy Simulation (LES) model with two different approximations given in Eqs. 5 and 6. Experiments have been carried out with both the expressions, and the u and v component of the simulated current are shown in Fig. 16 for location P2, P3 and P4 in Moskstraumen (Fig. 15). The u component of the current at the three locations (Fig. 16) shows that there is a small phase lag of up to one hour between the two different simulations. The phase lag is somewhat different at the three different locations, and the phase lag also has different magnitude and positive or negative sign depending on the direction and phase of the flow. At eastward flow the strength of the current is largest at the three locations when the expression in Eq. 5 was applied for the calculations (Fig.16). At location P2 the expression in Eq. 5 also gives the strongest current at westward flow, while at location P3 and P4 the two expressions gives about the same strength of the current at westward flow. The strength of the current varies across the sound, and there is some discrepancy in this variation between the two approximations applied for calculations of the horizontal eddy viscosity terms. For simulations where the

expression in Eq. 5 was applied the largest velocity occur north in the sound at location P2, while when Eq. 6 was applied the largest velocity occur more centered in the sound, at location P2 and P3. The v components of the current (Fig. 16) show that for simulations where the expression in Eq. 6 was applied for the calculations the south-north component of the current is more uniform than when the expression in Eq. 5 was applied.

Differences in the horizontal structures of the flow field between the two different approximations can also be revealed by the flow fields displayed in Fig. 17 at 13:00 (UT), 16:00 (UT), and 22:00 (UT). At 13:00 (UT) the current has just turned westward, and the flow fields show that the current is strongest in the northern part of the sound close to the headland in both simulations. The current is strongest close to the headland in simulations where Eq. 5 was applied, as also shown by the u component (Fig. 16). The flow fields at 13:00 (UT) also show that the variation in strength of the current across the sound is larger for simulations where Eq. 5 was applied than when Eq. 6 was applied. At 16:00 (UT) (Fig. 17 c and d) the flow is strong westward. The flow fields display that the westward flow is more like a jet (more focused) when the expression in Eq. 6 was applied than with Eq. 5. The flow fields also reveal some discrepancy in eddy formation between the two approximations. At 16:00 (UT) with westward flow the flow fields reveal eddies west of the Lofoten headland on the northern and southern side of the flow. In the simulations with Eq. 5 the northern eddy is small and close to the headland, while in simulations where Eq. 6 was used the northern eddy is larger and more pronounced. The flow fields at 22:00 (UT) at eastward flow are shown in Fig. 17 e and f. At eastward flow the simulations reveal eddies east of Mosken and the islands north of Mosken. The flow fields show that these are revealed different with the two different approximations. There is also a small discrepancy between the two different simulations for the eddy east of the Lofoten headland. In the following comparison the expression in Eq. 6 has been used for the calculations of the horizontal eddy viscosity terms.

The effect of the change in the horizontal eddy viscosity on the flow field was studied by simulations with different values of the constant q (table 1) for calculations of the horizontal eddy viscosity coefficient. To ensure a stable solution q have to be 3.5 or larger with the drag coefficient fixed to 0.005. The u and v component of the current for location P2, P3, and P4 are shown in Fig. 18. For the locations presented here the effect of the change in the constant q is only seen at locations P2, which is the northern of the locations. At this location the solution is damped, the strength of the current is reduced with an increased horizontal eddy viscosity. The change of the constant q has only minor effect on the horizontal structures of the flow field. The eddy formation is slightly affected as shown in the flow fields at 23:00 (UT) (Fig. 19).

To investigate the effect of the bottom friction on the flow simulations where performed with different values of the bottom drag coefficient (Eq. 4), see table 1. Simulation with a c_D of 0.003 gives unstable solution, and to ensure stability we have to choose c_D=0.004 or larger when q is fixed to 3.5. The u and v component of the current for location P2, P3, and P4 (Fig. 20) show that the strength of the current is reduced when the bottom drag coefficient is increased. The increase of the drag coefficient and the reduction of the current strength do not change the horizontal structures of the flow field considerably, though the eddy formation is to some extent affected due to change in the strength of the current.

The tidal signal contains a number of tidal constituents and its over harmonics. The tidal constituents at a location are found by harmonic analysis of time series of sea level measurements or current recordings. For tidal modeling we simplify by applying just the main semi-diurnal and diurnal contributions of the tidal signal as boundary forcing. For the sensitivity study the tidal model has been run with a varying number of tidal constituents included for the boundary forcing (sec. 2.3) during the spring tide 14 March 2009 in order to

Table 2: Time of High Water (HW) and Low Water (LW) at location L (Fig.15) for simulations with a different number of tidal constituents included as boundary forcing, compared to time of HW and LW from the NHS tidal predictions at the tide gauge in Bodø +10 minutes, where 44 tidal constituents are included for the predictions. Times are given in UT.

Location	*Tidal constituents*	*HW*	*LW*	*HW*	*LW*
Bodø + 10 minutes	44 constituents	01:24	07:26	13:35	19:50
L	M_2	01:30	07:45	13:57	20:12
L	M_2+S_2	01:13	07:27	13:33	19:46
L	M_2+S_2+N_2+K_1	01:39	07:45	13:46	20:04

study the effect of this variation on the tidal flow field. The simulations have mainly been carried out with the main semi-diurnal lunar constituent M_2 and the main semi-diurnal solar constituent S_2 as boundary forcing. For comparison the model has been run with only M_2 included as boundary forcing, and with M_2, S_2, the semi-diurnal elliptical-lunar constituent N_2, and the main diurnal constituent K_1 included as boundary forcing.

Table 2 gives High Water (HW) and Low Water (LW) at location L (Fig. 15) from the three simulations, and for comparison tidal predicted HW and LW extrapolated from Bodø (Bodø +10 minutes), where all available tidal constituents from the tide gauge in Bodø are used for the predictions (NHS). The table shows that for 14 March 2009 the time of HW and LW from the simulations with M_2+S_2 included as boundary forcing is closest to the time of HW and LW extrapolated from Bodø with 1 to 11 minutes in time difference. For simulations with only M_2 and with M_2+S_2+N_2+K_1 included as boundary forcing the time difference between simulated HW and LW at location L and the extrapolated HW and LW from Bodø varies from 6 to 22 minutes. The u and v component of the depth mean current for the locations P2, P3, and P4 are shown in Fig. 21. The effect of the change in boundary forcing is nearly the same at the three locations. When comparing the simulations with M_2 as boundary forcing with the simulation with M_2+S_2 we find that the strength of the current is increased with about 10-20 % from simulation with only M_2 forcing to the simulation with M_2+S_2 forcing. There is also a difference in phase between these two simulations. The maximum westward and eastward flow occur about 30 minutes earlier with M_2+S_2 as boundary forcing than with only M_2 (table 3). In simulations with the four main tidal constituents M_2, S_2, N_2, and K_1 the u component of the current, as expected, shows a daily inequality where the westward flow 14 March 2009 is at its strongest at about 03:00 (UT) and the eastward flow is at its strongest at about 21:00 (UT). The strength of the current is only slightly increased (about 5 %) by the addition of N_2 and K_1 for the boundary forcing. There is also a phase lag of the maximum flow between simulations with M_2+S_2 as boundary forcing and the simulations with the addition of N_2 and K_1. The maximum flow occur about 10 to 25 minutes later in simulations with M_2+S_2+N_2+K_1 than with only M_2+S_2 as boundary forcing (table 3).

For the three simulations the maximum westward flow occur about 1 hour and 15 minutes after the respective HW at location P2, and maximum eastward flow occur about 50 minutes after the respective LW. At location P3 the maximum westward flow occur about 1 h 10 min after the respective HW, and the maximum eastward flow occur about 1 h 15 min after the respective LW. The simulations performed for the comparison show that the number of constituents included for the boundary forcing affects the phase and strength of the current, but has only minor effect on the horizontal structures of the flow field (flow fields not shown).

Table 3: Maximum magnitude of the westward and eastward flow at location P2 and P3 (Fig. 15) for simulations with a different number of tidal constituents included as boundary forcing.

Location	*Tidal constituents*	*Westward*	*Eastward*	*Westward*	*Eastward*
P2	M_2	02:48	08:42	15:13	21:07
P2	M_2+S_2	02:24	08:16	14:45	20:37
P2	M_2+S_2+N_2+K_1	02:49	08:40	14:54	20:49
P3	M_2	02:45	09:06	15:10	21:31
P3	M_2+S_2	02:21	08:42	14:43	21:03
P3	M_2+S_2+N_2+K_1	02:45	09:01	14:55	21:16

6 Summary and discussion

The ADCP measurements off the Lofoten headland reveal strong currents and small-scale features in the horizontal structures of the flow field in the wake of the headland and islands in the area. The two numerical tidal current models applied for comparison with the ADCP data capture the main features of the flow field as revealed in the measurements. The simulations reveal a complex tidal flow field with small-scale features and formation of eddies in the wake of the Lofoten headland, Mosken and the numerous small islands in the area. When the main flow through the sound is westerly, the simulated flow fields reveal two eddies west of the headland, one on the northern side of the main flow and one on the southern side. When the direction of the main flow is easterly the simulations reveal an eddy in the wake of the Lofoten headland and also eddies in the wake of Mosken and the small islands north of Mosken. The ADCP measurements confirm that the flow field contains non-linear flow features (wakes, eddies, etc.) as shown in the simulations. Though there is a good correspondence between observations and simulations, the locations of the simulated features are not consistent with the observations for all features. For example the observations reveal an irregularity in the flow field near location G (Fig. 10 d), while the simulated flow fields reveal wake effect south and west of location G (Fig. 10 b and f). The feature in the simulated flow fields can be associated with the observation at location G, but they are not consistent. There are also observed flow features which are not resolved by the models, for example the feature seen in the observations east off Herjeskallen at easterly flow is not revealed in the simulated flow fields.

There is numerous small islands, skerries and shallow rocks in the shallow area west and north of Værøy. For the experiments NHS provided us with detailed bottom topography based mainly on multibeam bathymetric data. With grid resolution of 50 and 100 m we are able to resolve much of the fine scale features of the bottom topography, but we are still not able to resolve all the shallow rocks and small islands in the area, e.g. the shallow rocks Herjeskallane and Svarvskallan as described in sec. 4.1. To be able to simulate the flow features connected to these irregularities in the bottom topography an even finer resolution of the horizontal grid is required.

Also the vertical cross sections of the ADCP measurements reveal valuable information about the structures of the flow field. The sections show mostly quite uniform current through the depth in the sound, but with maximum speed observed in the upper layer. The maximum speed was measured to $1.7\,\mathrm{ms}^{-1}$ in the upper layer at west going flow. At east going flow the ADCP measurements and the density profiles indicate that the water masses from outside the sound flow under the less dense water in Vestfjorden.

The measurements are made along 12 sections for a period of 8.5 hours, i.e. less than one M_2 period, and hence only reveal a limited part of the flow field. The 12 sections were

carefully planned from simulated flow fields, and made along tracklines with expected flow features and horizontally variability of the flow field. Hence the measurements from 14 March 2009 gives valuable information about the horizontal structures of the flow field. For a better and more detailed validation of the numerical models, several sections with ADCP measurements would have been valuable. For example an additional ADCP section further west of section C_1-D would reveal more of the horizontal structures of flow field west of the Lofoten headland where there is a huge discrepancy between the two numerical models in how they reveal the northern eddy.

The main flow features of the tidal flow are revealed quite similar in simulations with the two tidal models applied for the experiments. But there are also some discrepancies between the models, especially seen for the eddy formation in the wake of the headland and islands. There is also a difference in the strength of the current between the two models. At location P3 in the middle of the sound of Mosken the depth integrated model gives a maximum depth integrated speed of $1.2\,\mathrm{ms}^{-1}$ while the σ-coordinate model gives a maximum speed of $1.6\,\mathrm{ms}^{-1}$ in the surface layer and $1.2\,\mathrm{ms}^{-1}$ in the bottom layer. That means that with the σ-coordinate model we are able to calculated current that correspond in strength to the observations in the sound of Mosken, while the depth integrated model underestimate the strength some. From the available ADCP measurements we are not able to tell which one of the models that has the best correspondence for the horizontal structures of the flow field. For the further validation of the models several ADCP measurements are required.

The survey was carried out during calm weather conditions with litte wind. Since the tidal current dominates the wind driven current in the area the conditions for comparison of observed current to simulated tidal current should be good. For the tidal modeling we simplify by applying only the main tidal constituents as boundary forcing. For the comparison in this report the simulations have mainly been carried out with the two main semi-diurnal tidal constituents M_2 and S_2 as boundary forcing. In addition the depth integrated model was run with the addition of N_2 and K_1 as boundary forcing, and also only with the main constituent M_2 as forcing.

Comparison of simulations with only M_2, with M_2 and S_2, and with M_2+S_2+N_2+K_1 imposed at the open boundaries show some small deviations. The difference in strength of the current is about 20 % from simulations with M_2 as boundary forcing to simulations with M_2+S_2+N_2+K_1 as boundary forcing, where the last one gives results closest to the observations. There is also some difference in phase between the three different simulations. The difference in phase of the current is varying during the period of 24 hours the analyses where made for. For the 14. March 2009 the simulation with M_2+S_2 imposed as boundary force gave best correspondence in time of HW and LW with the extrapolation of HW and LW from Bodø (table 2). The situation in another period could be different. From the ADCP measurements we are not able to tell which one of the approximations has the best correspondence to the observations. The ADCP measurements taken along the 12 sections gives information about the horizontal and vertical structures of the flow field at the time the observations were made. For more detailed comparison of the flow during several days time series of both current observations and modeled current, and harmonic analyses of these are required.

Also sensitivity due to different parameters and settings was studied for the depth integrated model. The experiments show that the flow is sensitive to the choice of bottom drag coefficient in the model. The strength of the current is reduced with the increase of the drag coefficient, but the horizontal structures of the flow field was not considerably affected. For the three locations presented in the report only the northern location (P2) showed sensitivity to change in the constant q for calculations of the horizontal eddy viscosity coefficient. The largest variation between the tidal simulations was found due

to use of the expression in Eq. 5 or Eq. 6 for calculation of the horizontal eddy viscosity terms. The effect of use of the two different expressions was found to be largest at the northern location (P2), but also the other locations show a difference in strength of the current and in the phase. Also the flow fields show that there is a difference between the two expressions applied for the calculations. It seems like the effect is most pronounced in the shear zones.

To conclude the models in general capture the main features of the measured current, though there are some features that the models do not capture, and there are discrepancies between the two models. These inconsistencies between the models and observations and between the two models are especially associated with eddies and wakes behind the headland and the islands, and with the rocks which are not resolved by the depth matrix. It could be of interest to do tidal simulations with a finer horizontal grid resolution to study the effect of a better resolution of the bottom topography. The depth integrated model has for the experiments also been run with a 50 m horizontal grid resolution for comparison, but did not reveal much difference from simulations with 100 m grid resolution. In Lynge et al. (2010) horizontal relative dispersion in Moskstraumen due to horizontal grid resolution was studied with horizontal grid from 50 to 800 m. The study showed only small differences in dispersion between simulations with 50 and 100 m grid resolution. To study the effect of the complex structures of the bottom topography on the flow field an even finer grid is required for the model simulations. Knowledge about and understanding of the tidal model is important to be able to make accurate model prediction of the tidal flow. For further studies of tidal current modeling off the Lofoten headland a more detailed study of separation and eddy formation due to bottom friction and shear stress would be of interest. The simulations with the σ-coordinate model where carried out with homogenous conditions. For further studies the model could be run with stratified conditions. Studies of the horizontal relative dispersion (Lynge et al., 2010) showed only small differences between simulations with stratification and homogenous condition, but the effect of stratification may be more important with a finer grid resolution. In future studies with a finer grid resolution also the effect of non-hydrostatic pressure may be necessary to include for the simulations.

Acknowledgment

I would like to thank the Institue of Marine Research (Bergen, Norway) for the possibility to participate on the survey with the research vessel G.O. Sars March 2009. Particular thanks to Henrik Søiland, Kjell Arne Mork, and Asgeir Steinsland for help and instructions of the ADCP instruments. Also a greatful thanks to the Norwegian Hydrographic Service who has provided us high resolution bottom topography for the area.

References

Berntsen, H., Kowalik, Z., Sælid, S., and Sørli, K. (1981). Efficient numerical-simulation of ocean hydrodynamics by a splitting procedure. *Modeling Identification and Control*, 2(4):181–199.

Berntsen, J. (2004). Users guide for a modesplit σ-coordinate numerical ocen model. Version 4.1. Technical report, Technical Report 135, Department of Applied Mathematics, University of Bergen, Johs. Bruns gt.12, N-5008 Bergen, Norway. p.54.

Berntsen, J., Xing, J. X., and Davies, A. M. (2008). Numerical studies of internal waves

at a sill: Sensitivity to horizontal grid size and subgrid scale closure. *Continental Shelf Research*, 28(10-11):1376–1393.

Berntsen, J., Xing, J. X., and Davies, A. M. (2009). Numerical studies of flow over a sill: sensitivity of the non-hydrostatic effects to the grid size. *Ocean Dynamics*, 59(6):1043–1059.

Blumberg, A. F. and Mellor, G. L. (1987). A description of a three-dimensional coastal ocean circulation model. *Heaps, N. S. (ed.). Coastal and Estuarine Sciences, 4. Three-dimensional Coastal Ocean Models. Xi+208p. American Geophysical Union: Washington, D.c., Usa. Illus*, pages 1–16.

Burchard, H. and Rennau, H. (2008). Comparative quantification of physically and numerically induced mixing in ocean models. *Ocean Modelling*, 20(3):293–311.

Crean, P., Murty, T., and J.A., S. (1988). *Mathematical Modelling of Tides and Estuarine Circulation*. Springer-Verlag, N.Y.

Davies, P. (1995). Eddy formation behind a coastal headland. *Journal of Coastal Research*, 11:154–167.

Geyer, W. R. (1993). Three-dimensional tidal flow around headlands. *Journal of Geophysical Research*, 98, NO. C1:955–966.

Geyer, W. R. and Signell, R. (1990). Measurements of tidal flow around a headland with a shipboard acoustic doppler current profiler. *Journal of Geophysical Research*, 95 NO.C3:3189–3197.

Gjevik, B. (1998). Moskstraumen myter, diktning og virklighet. *Annual proceeding of The Norwegian Academy of Science end Letters, Oslo, Norway*.

Gjevik, B., Hareide, D., Lynge, B. K., Ommundsen, A., Skailand, J., and Urheim, H. (2006). Implementation of high resolution tidal current fields in electronic charts systems. *Journal of Marine Geodesy*, 29(1):1–17.

Gjevik, B., Moe, H., and Ommundsen, A. (1997). Sources of the Maelstrom. *Nature*, 388(6645):837–838.

Haidvogel, D. and Beckmann, A. (1999). *Numerical ocean circulation modeling*, page 318. Imperial College Press, Series on Environmental Science and Management, 2.

Hjelmervik, K., Ommundsen, A., and Gjevik, B. (2005). Implementation of non-linear advection terms in a high resolution tidal model. Technical report, Preprint Series, No. 1, Dept. Math. University of Oslo, Norway, ISSN 0809-4403.

Kowalik, Z. and Murty, T. S. (1993). *Numerical Modeling of Ocean Dynamics, volume 5 of Advanced Series on Ocean Engineering*. World Scientific.

Lynge, B. K., Berntsen, J., and Gjevik, B. (2010). Numerical studies of dispersion due to tidal flow through Moskstraumen, northern Norway. *Ocean Dynamics*, 60:907–920.

Maddock, L. and Pingree, R. D. (1978). Numerical simulation of the Portland tidal eddies. *Estuarine and Coastal Marine Science*, 6:353–363.

Martinsen, E. A. and Engedahl, H. (1987). Implementation and testing of a lateral boundary scheme as an open boundary-condition in a barotropic ocean model. *Coastal Engineering*, 11(5-6):603–627.

Mellor, G. (1996). User guide for three-dimensional, primitive equation, numerical ocean model. Technical report, Technical report, Princeton University.

Mellor, G. (2004). User guide for three-dimensional, primitive equation, numerical ocean model. Technical report, Technical report, Princeton University.

Mellor, G. and Blumberg, A. F. (1985). Modelling vertical and horizontal diffisivities in the sigma coordinate system. *Monthly Weather Review*, 113:1379–1383.

Mellor, G. L., Oey, L.-Y., and Ezer, T. (1998). Sigma coordinate pressure gradient errors and the seamount problem. *Journal of Atmospheric and Oceanic Technology*, 15(5):1122–1131.

Mellor, G. L. and Yamada, T. (1982). Development of a turbulence closure-model for geophysical fluid problems. *Reviews of Geophysics*, 20:851–875.

Mesinger, F. and Arakawa, A. (1976). Numerical methods used in atmospheric models. *Garp Publication Series No 17*, WMO-ICSU.

Moe, H., Ommundsen, A., and Gjevik, B. (2002). A high resolution tidal model for the area around The Lofoten Islands, northern Norway. *Continental Shelf Research*, 22(3):485–504.

NHS (2001). *Pilots books for the Norwegian coast, 6th Edition. Number 5 in Den Norske Los*. Norwegian Hydrographic Service, Stavanger, Norway; ISBN 82-90653-17-4.

Pingree, R. and Maddock, L. (1979). The tidal physics of headland flows and offshore tidal bank formation. *Marine Geology*, 32:269–289.

RD-Instruments (2001). Winadcp user's guide. *RD-Instruments, Acoustic Doppler Solutions. Available at http://www.rdinstruments.com/cc_documents.html*.

RD-Instruments (2004). Wmdas user's guide. *RD-Instruments, Acoustic Doppler Solutions. Available at http://www.rdinstruments.com/cc_documents.html*.

Rennau, H. and Burchard, H. (2009). Quantitative analysis of numerically induced mixing in a coastal model application. *Ocean Dynamics*, 59(5):671–687.

Signell, R. P. and Geyer, W. R. (1991). Transient eddy formation around headlands. *Journal of Geophysical Research-oceans*, 96(C2):2561–2575.

Smagorinsky, J. (1963). General circulation experiments with the primitive equations. *Monthly Weather Review*, 91(3):99–164.

Xing, J. and Davies, A. (2006). Processes influencing tidal mixing in the region of sills. *Geophysical Research Letters*, 33(4):L04603 doi:10.1029/2005GL025226.

Yang, H. Q. and Przekwas, A. J. (1992). A comparative-study of advanced Shock-capturing schemes applied to Burgers-equation. *Journal of Computational Physics*, 102(1):139–159.

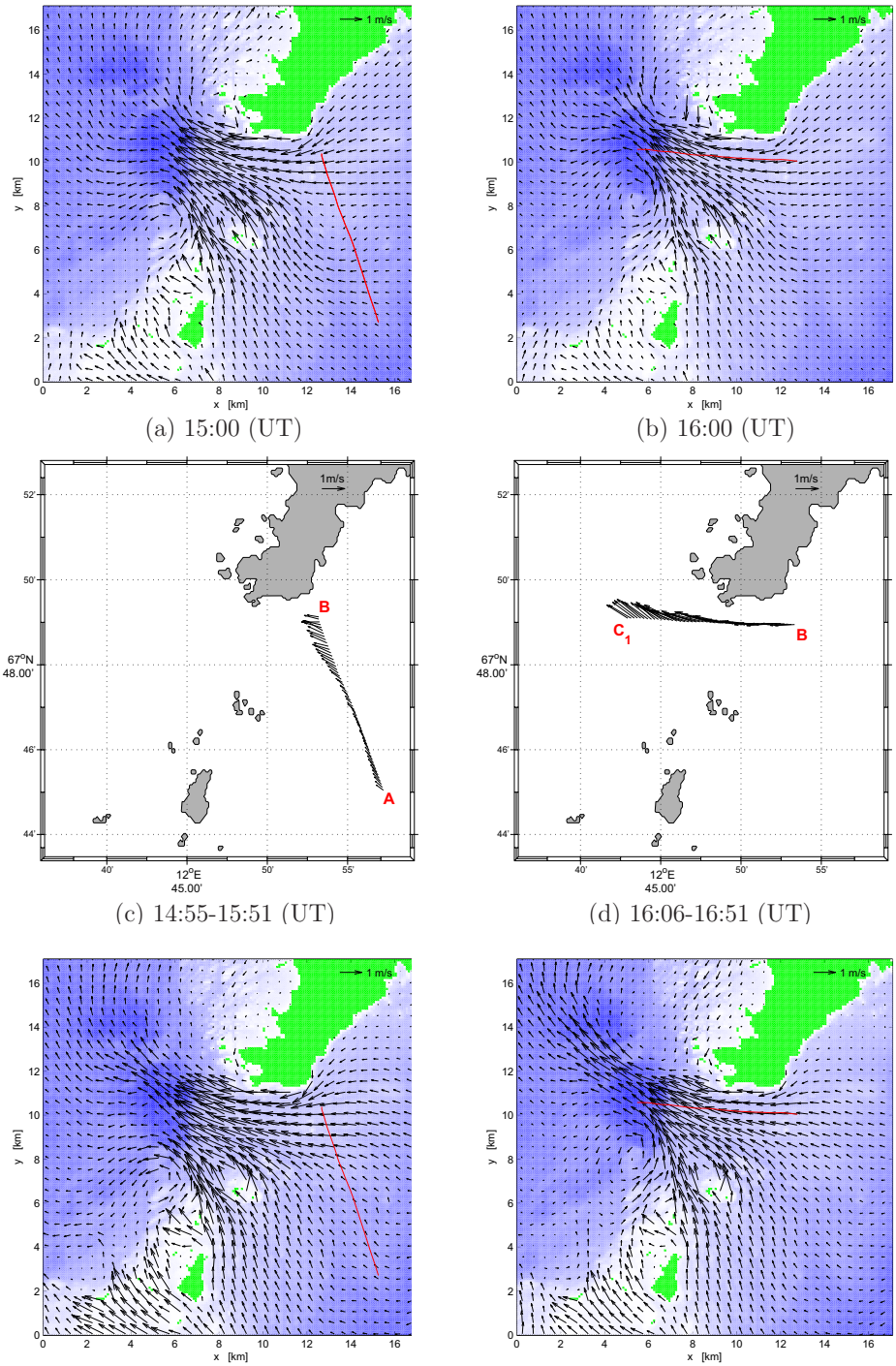

(a) 15:00 (UT)

(b) 16:00 (UT)

(c) 14:55-15:51 (UT)

(d) 16:06-16:51 (UT)

(e) 15:00 (UT)

(f) 16:00 (UT)

Figure 6: ADCP measured depth mean current from survey with RV G.O. Sars 14. March 2009 for sections (c) A-B and (d) B-C_1, together with corresponding flow fields of the depth averaged current from the depth integrated model (a and b) and the σ-coordinate model (e and f).

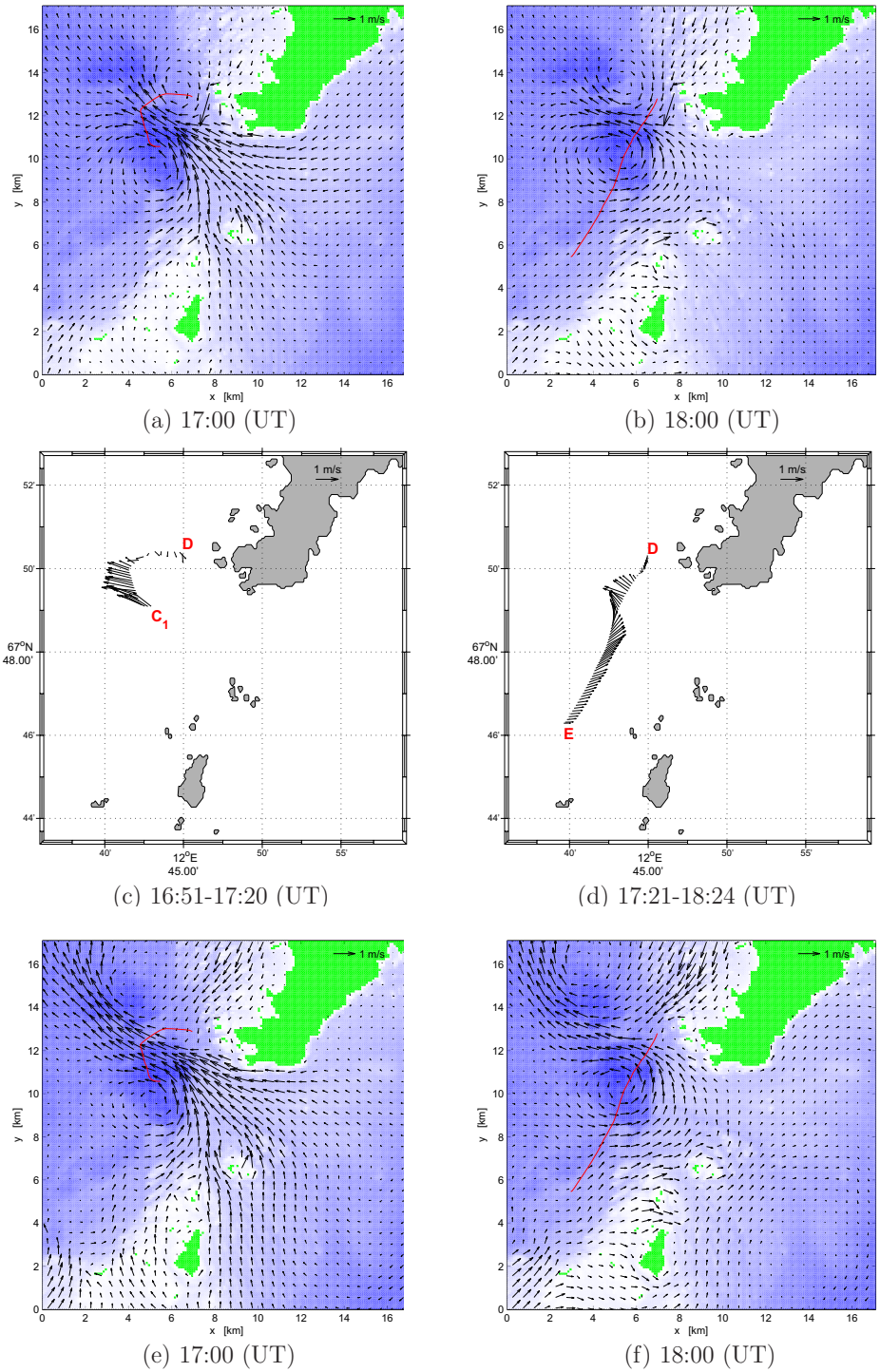

(a) 17:00 (UT)

(b) 18:00 (UT)

(c) 16:51-17:20 (UT)

(d) 17:21-18:24 (UT)

(e) 17:00 (UT)

(f) 18:00 (UT)

Figure 7: ADCP measured depth mean current from survey with RV G.O. Sars 14. March 2009 for sections (c) C_1-D and (d) D-E, together with corresponding flow fields of the depth averaged current from the depth integrated model (a and b) and the σ-coordinate model (e and f).

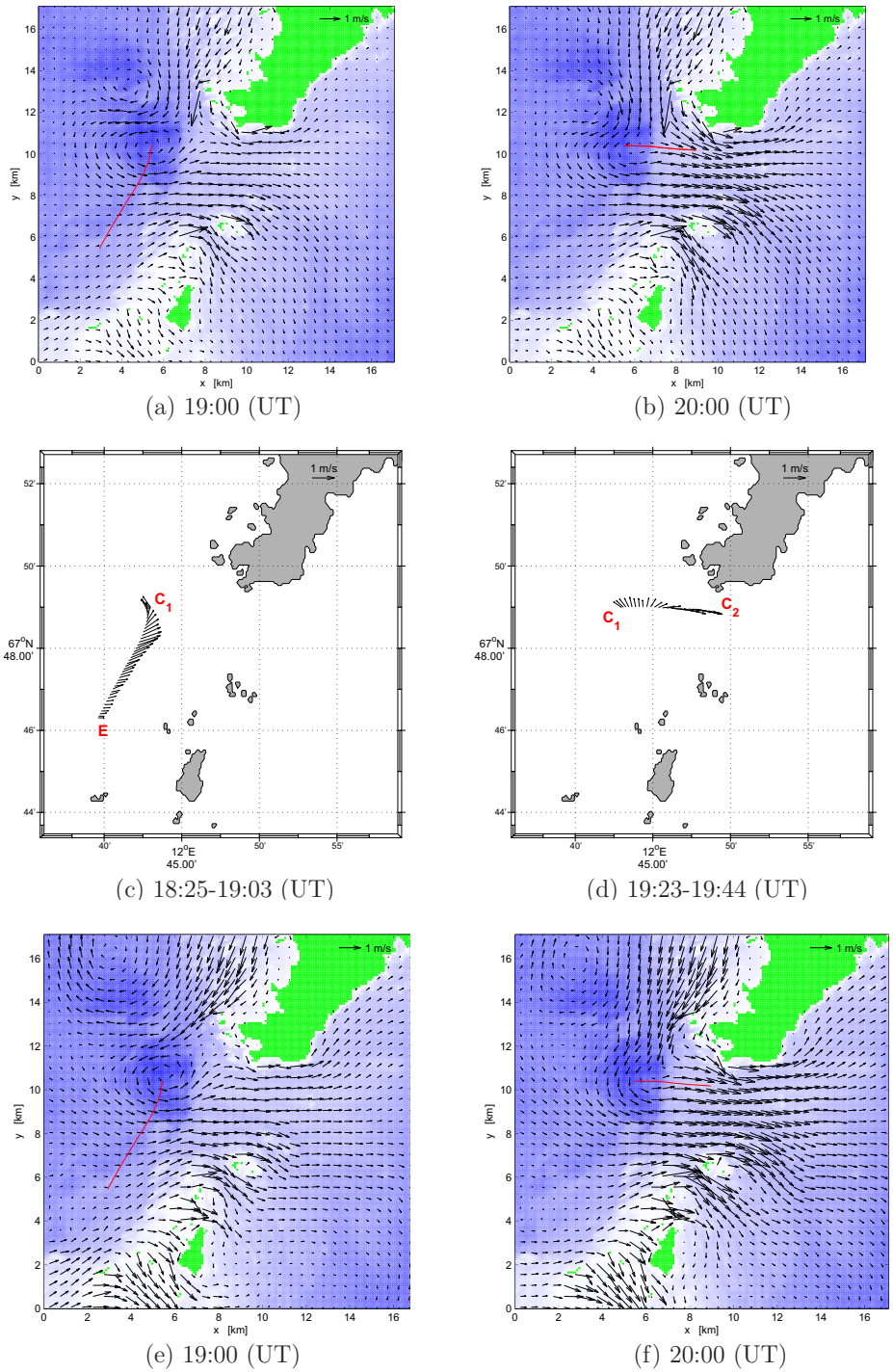

(a) 19:00 (UT)

(b) 20:00 (UT)

(c) 18:25-19:03 (UT)

(d) 19:23-19:44 (UT)

(e) 19:00 (UT)

(f) 20:00 (UT)

Figure 8: ADCP measured depth mean current from survey with RV G.O. Sars 14. March 2009 for sections (c) E-C_1 and (d) C_1-C_2, together with corresponding flow fields of the depth averaged current from the depth integrated model (a and b) and the σ-coordinate model (e and f).

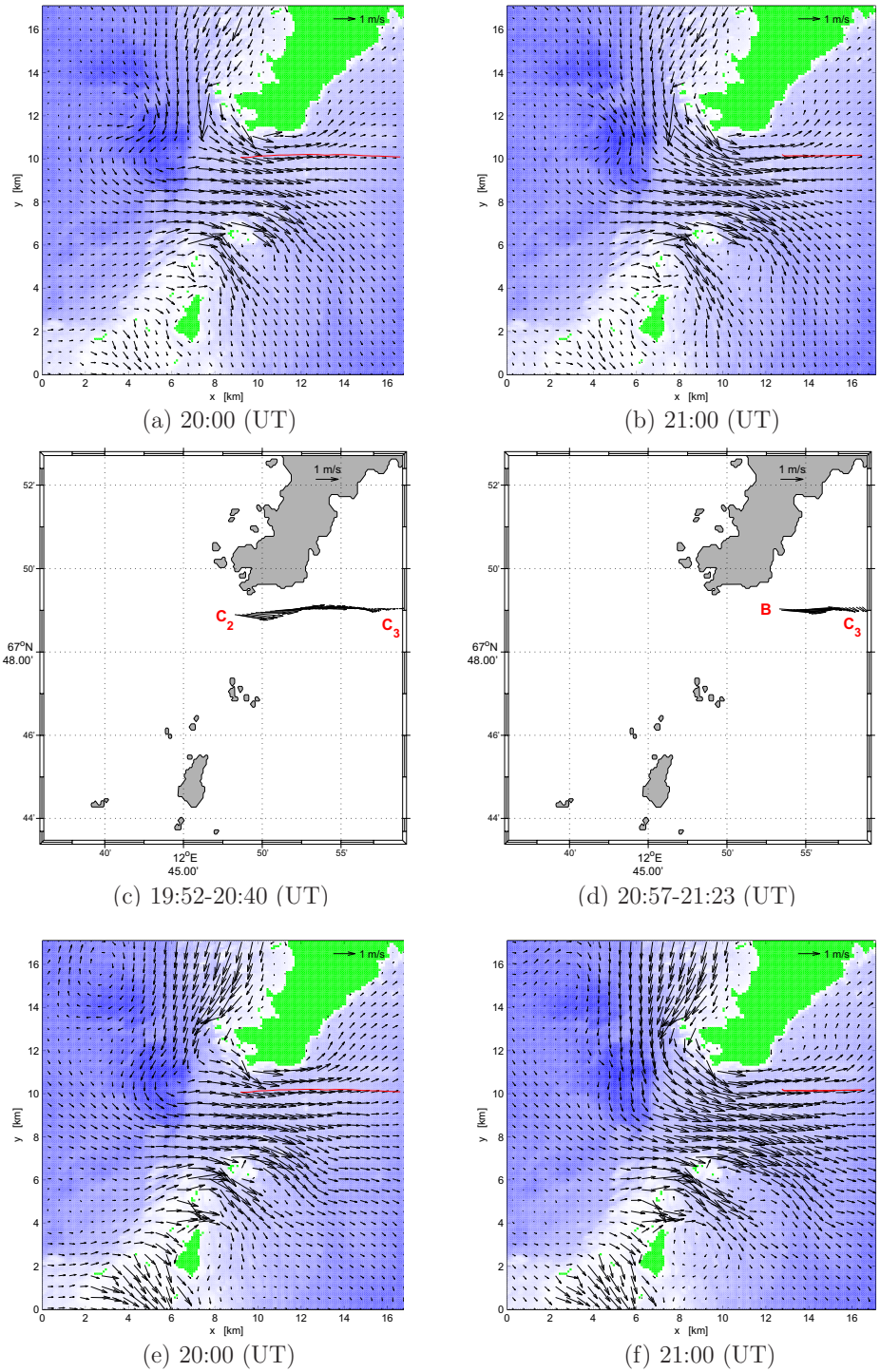

(a) 20:00 (UT)

(b) 21:00 (UT)

(c) 19:52-20:40 (UT)

(d) 20:57-21:23 (UT)

(e) 20:00 (UT)

(f) 21:00 (UT)

Figure 9: ADCP measured depth mean current from survey with RV G.O. Sars 14. March 2009 for sections (c) C_2-C_3 and (d) C_3-B, together with corresponding flow fields of the depth averaged current from the depth integrated model (a and b) and the σ-coordinate model (e and f).

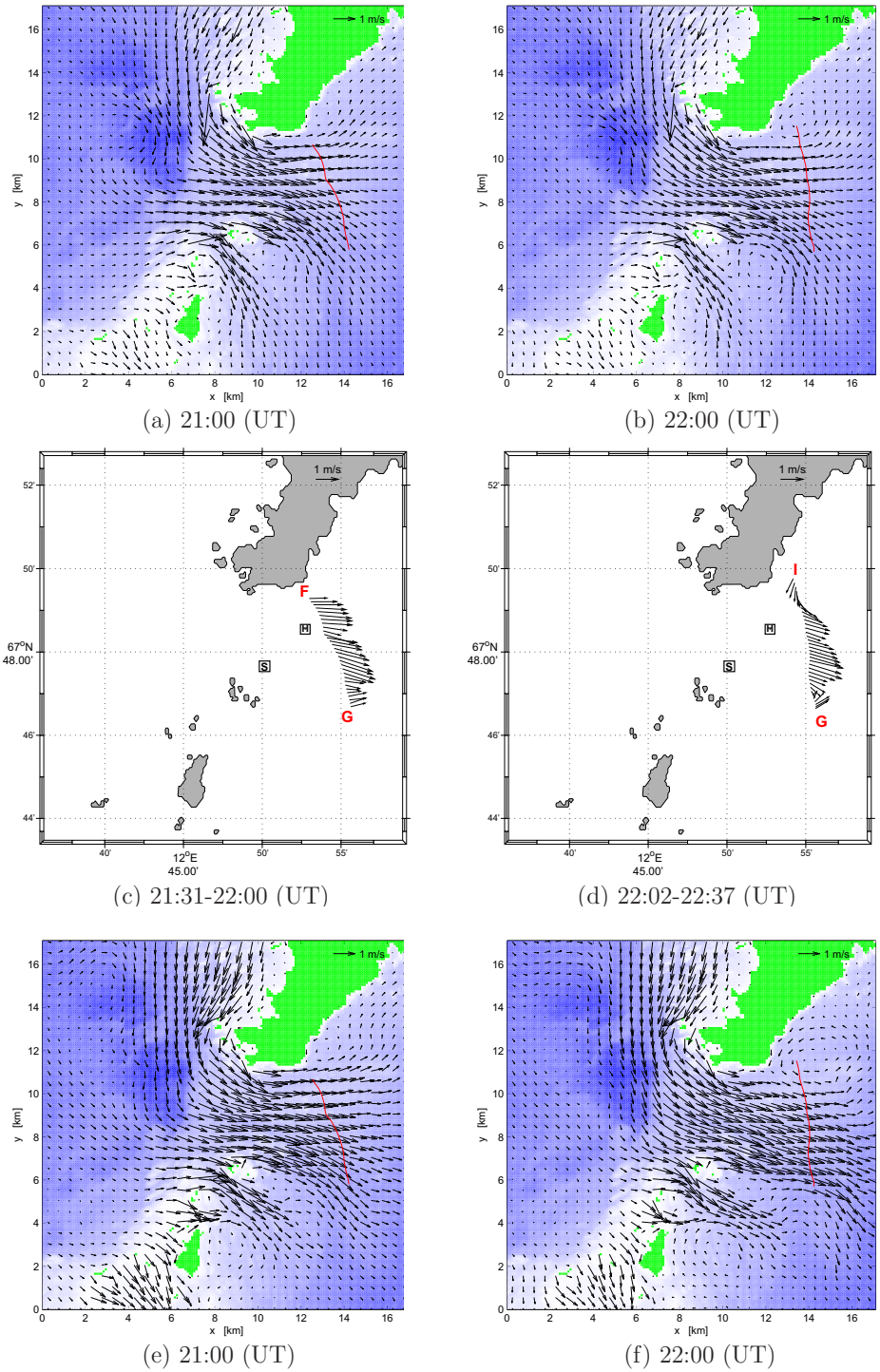

(a) 21:00 (UT)

(b) 22:00 (UT)

(c) 21:31-22:00 (UT)

(d) 22:02-22:37 (UT)

(e) 21:00 (UT)

(f) 22:00 (UT)

Figure 10: ADCP measured depth mean current from survey with RV G.O. Sars 14. March 2009 for sections (c) F-G and (d) G-I, together with corresponding flow fields of the depth averaged current from the depth integrated model (a and b) and the σ-coordinate model (e and f).

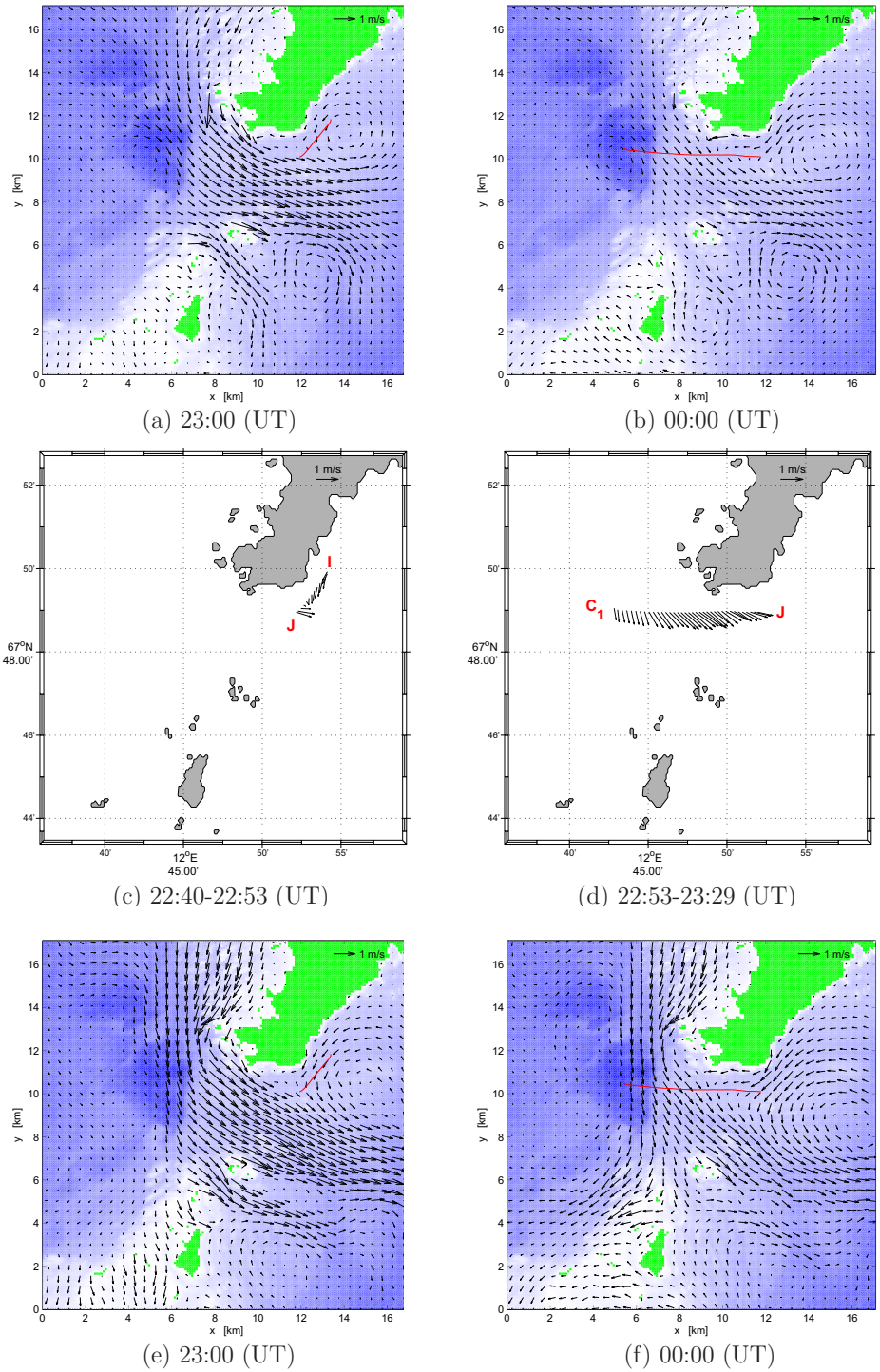

(a) 23:00 (UT)

(b) 00:00 (UT)

(c) 22:40-22:53 (UT)

(d) 22:53-23:29 (UT)

(e) 23:00 (UT)

(f) 00:00 (UT)

Figure 11: ADCP measured depth mean current from survey with RV G.O. Sars 14. March 2009 for sections (c) I-J and (d) J-C_1, together with corresponding flow fields of the depth averaged current from the depth integrated model (a and b) and the σ-coordinate model (e and f).

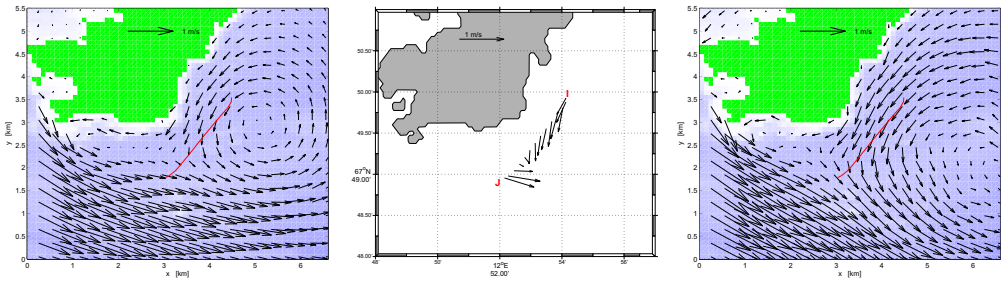

(a) 23:00 (UT) (b) 22:40-22:53 (UT) (c) 23:00 (UT)

Figure 12: ADCP measured depth mean current from survey with RV G.O. Sars 14. March 2009 for section I-J (b), together with corresponding flow fields of the depth averaged current from the depth integrated model (a) and the σ-coordinate model (c).

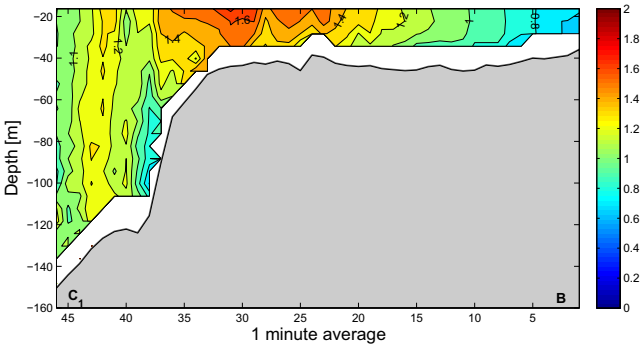

(a) Section B-C_1 – 16:06-16:51 (UT)

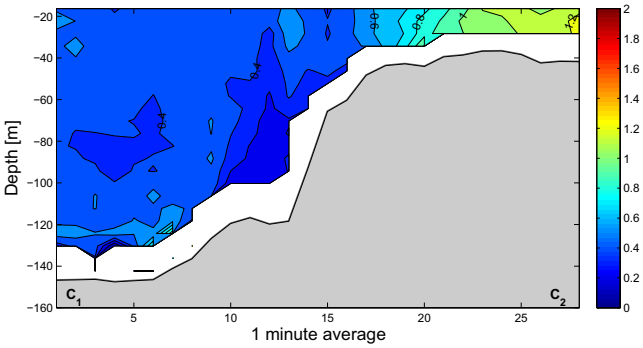

(b) Section C_1-C_2 – 19:23-19:44 (UT)

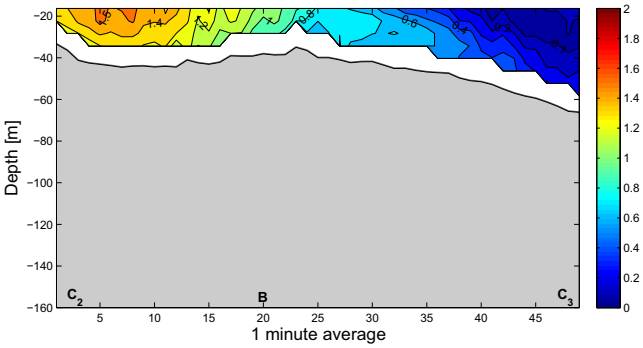

(c) Section C_2-C_3 – 19:52-20:40 (UT)

Figure 13: The cross sections of the magnitude of the ADCP measured 1 minute averaged current [ms^{-1}] are shown for a) section B-C_1, b) section C_1-C_2, and c) section C_2-C_3 (Fig. 5). The vertical axis shows depth in meters from 16.3 m depth (the midpoint of the uppermost bin), and horizontal axis is given in number of 1 minute averaged measurements. Easterly direction is to the right.

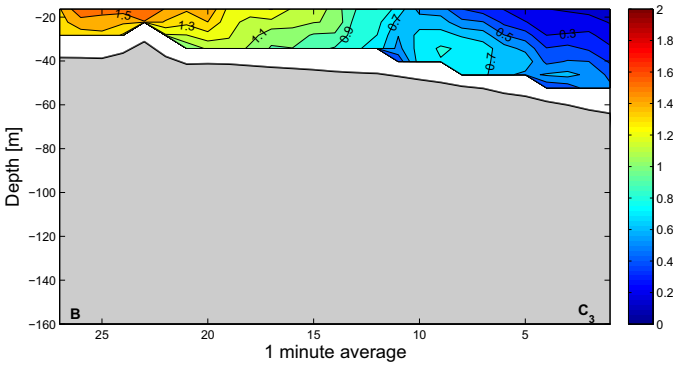

(a) Section C_3-B – 20:57-21:23 (UT)

Figure 14: The cross section of the magnitude of the ADCP measured 1 minute averaged current [ms^{-1}] are shown for section C_3-B (Fig. 5). The vertical axis shows depth in meters from 16.3 m depth (the midpoint of the uppermost bin), and horizontal axis is given in number of 1 minute averaged measurements. Easterly direction is to the right.

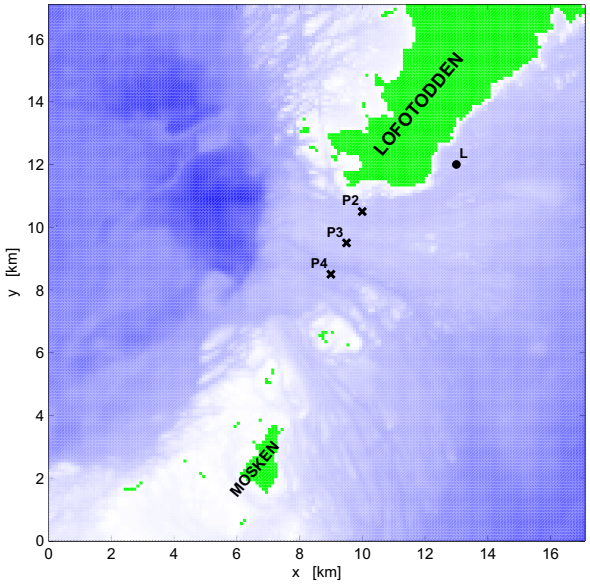

Figure 15: Locations P2, P3, and P4 for comparison of east-west and north-south current components in sensitivity studies, and location L for comparison of High- and Low Water in sensitivity studies.

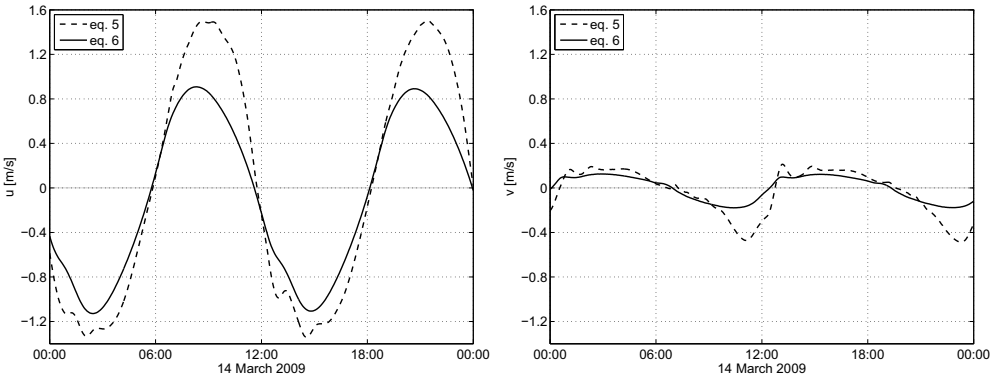

(a) P2

(b) P2

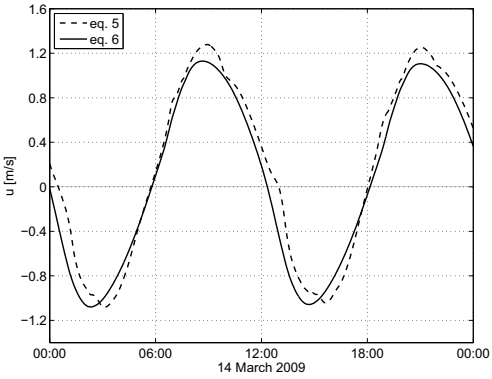

(c) P3

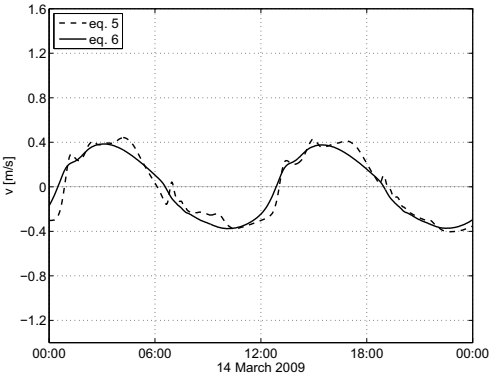

(d) P3

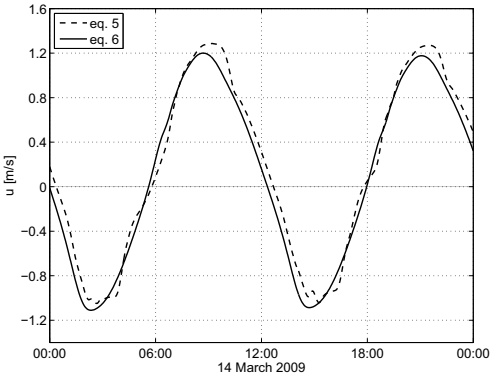

(e) P4

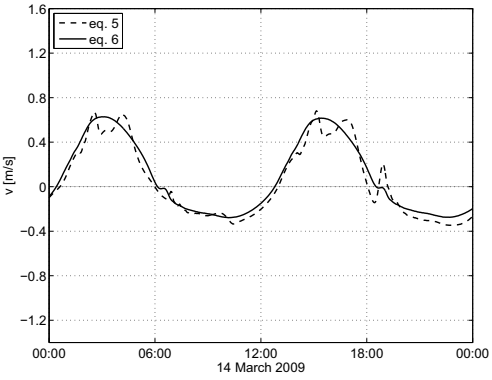

(f) P4

Figure 16: The u and v component of the depth mean current at location P2, P3 and P4 shown in Fig. 15. East is positive direction for u and north is positive direction for v.

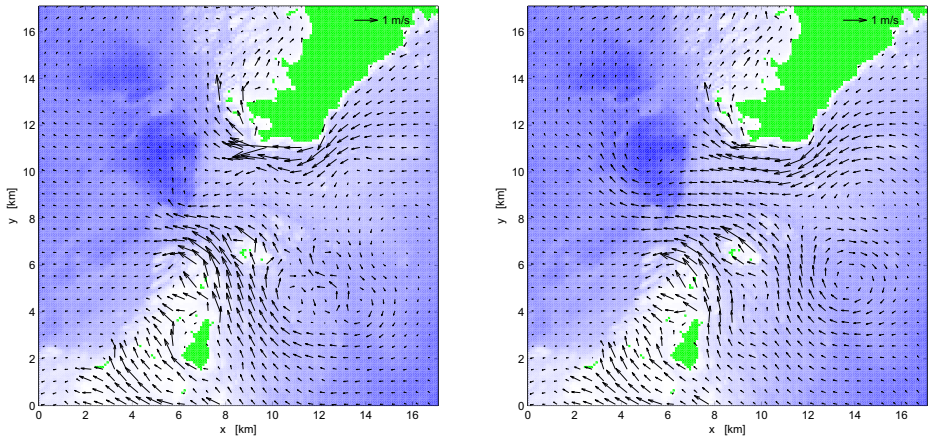

(a) 13:00 (UT), Eq. 5

(b) 13:00 (UT), Eq. 6

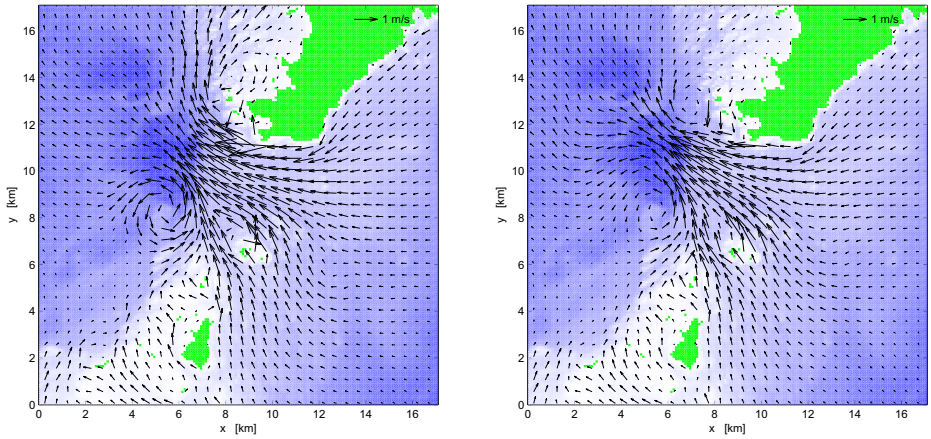

(c) 16:00 (UT), Eq. 5

(d) 16:00 (UT), Eq. 6

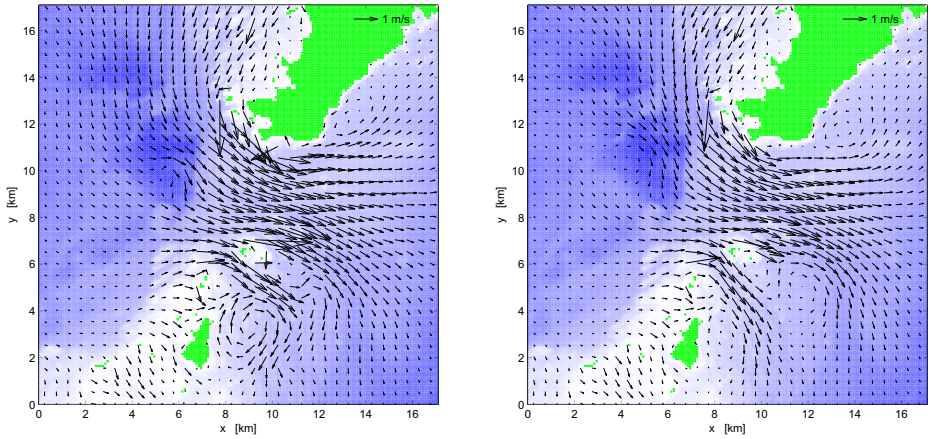

(e) 22:00 (UT), Eq. 5

(f) 22:00 (UT), Eq. 6

Figure 17: Depth mean current from the depth integrated model for comparison of model simulations where the expression in Eq. 5 or Eq. 6 has been applied for the calculations of the horizontal eddy viscosity terms.

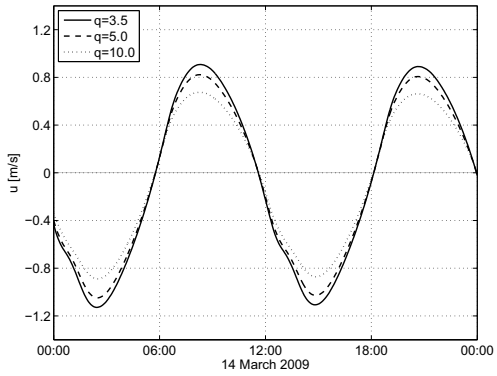

(a) P2

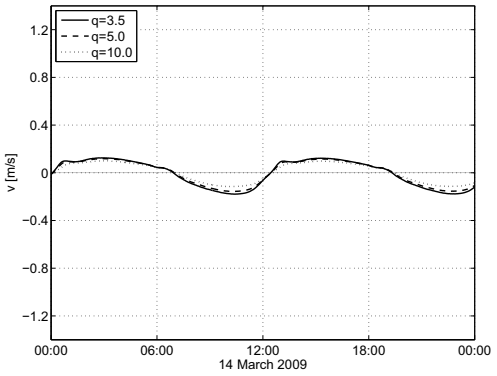

(b) P2

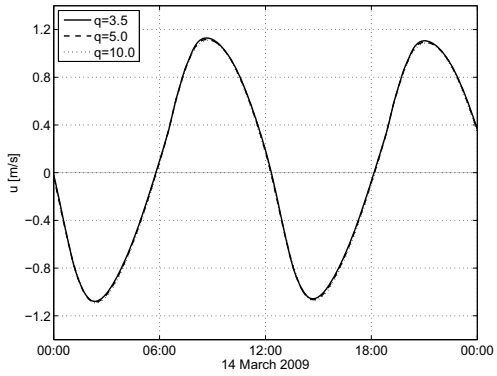

(c) P3

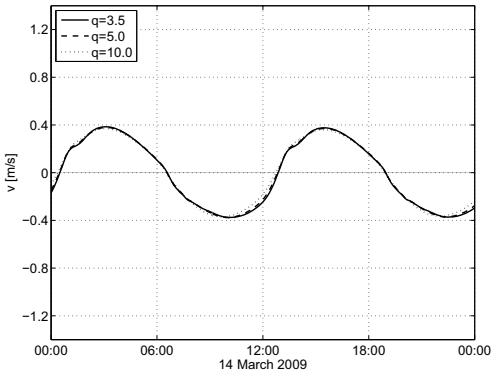

(d) P3

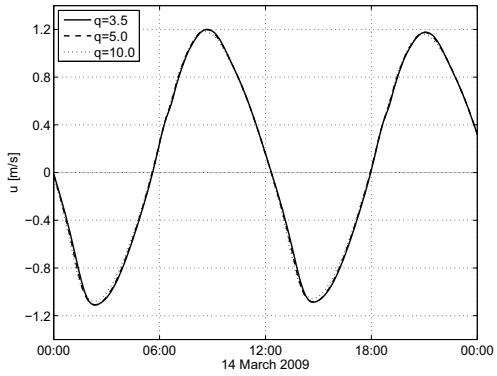

(e) P4

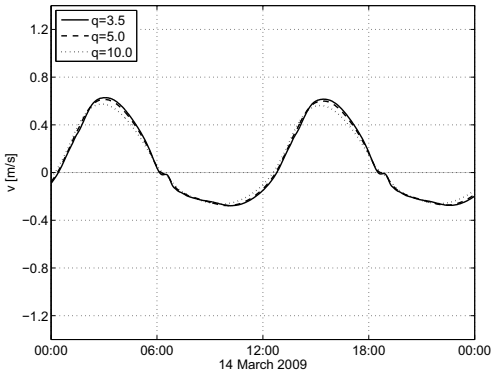

(f) P4

Figure 18: The u and v component of the depth mean current at location P2, P3 and P4 shown in Fig. 15. East is positive direction for u and north is positive direction for v.

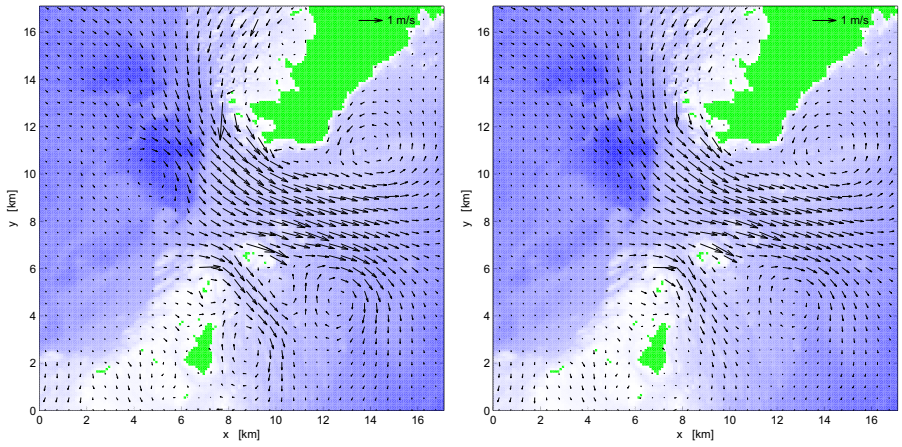

(a) 23:00 (UT), q=3.5

(b) 23:00 (UT), q=10.0

Figure 19: Depth mean current from the depth integrated model for comparison of model simulations with different values of the constant q in calculations of the eddy viscosity coefficient (Eq. 7).

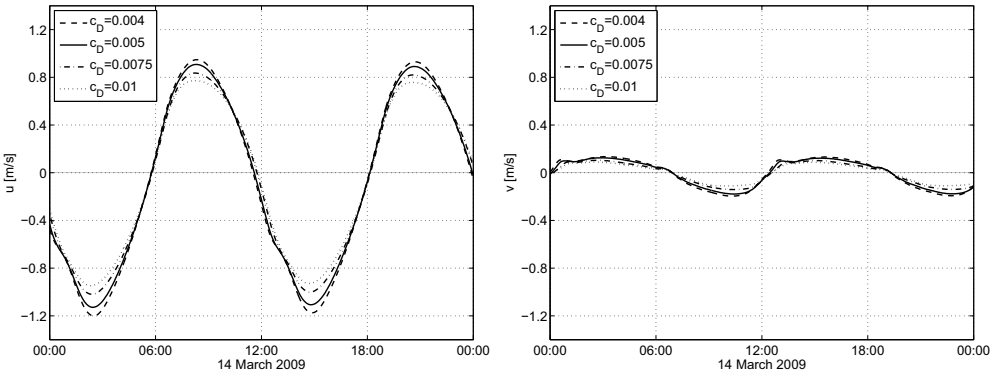

(a) P2 (b) P2

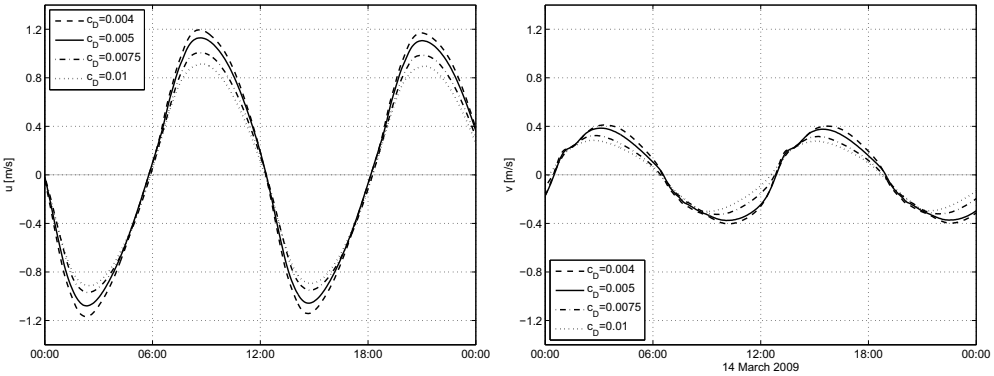

(c) P3 (d) P3

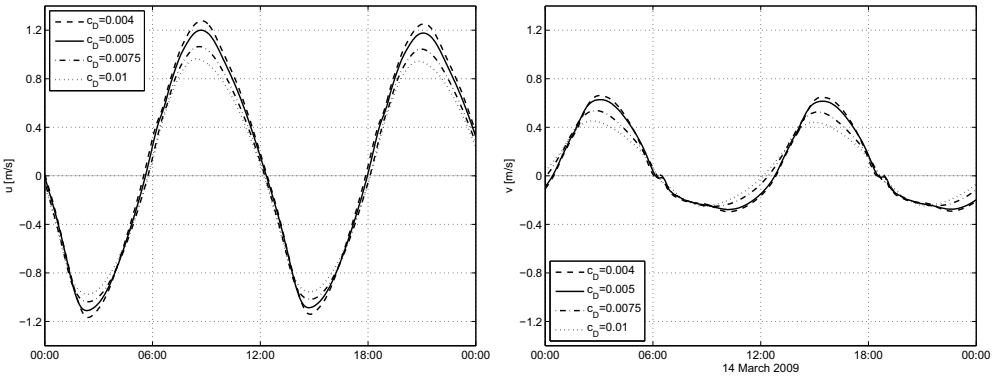

(e) P4 (f) P4

Figure 20: The u and v component of the depth mean current at location P2, P3 and P4 shown in Fig. 15. East is positive direction for u and north is positive direction for v.

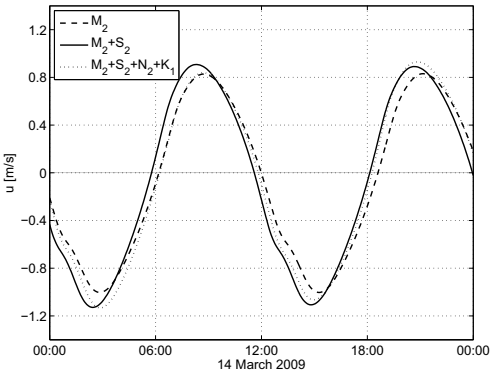

(a) P2

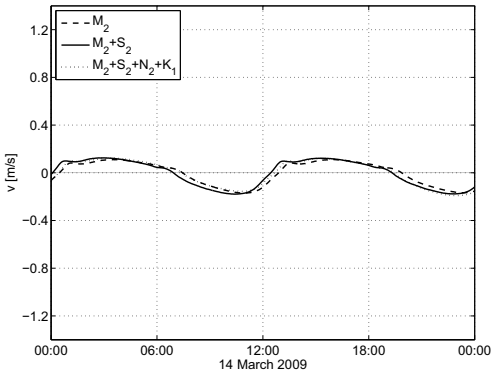

(b) P2

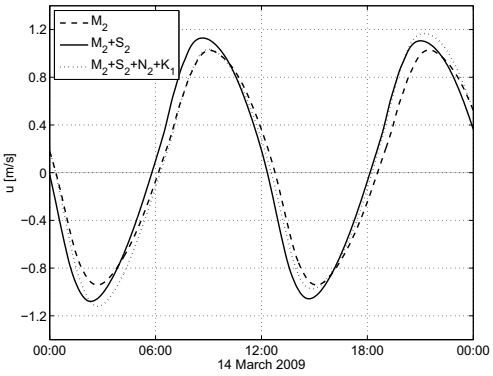

(c) P3

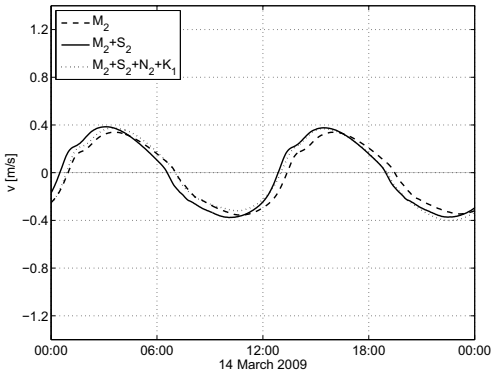

(d) P3

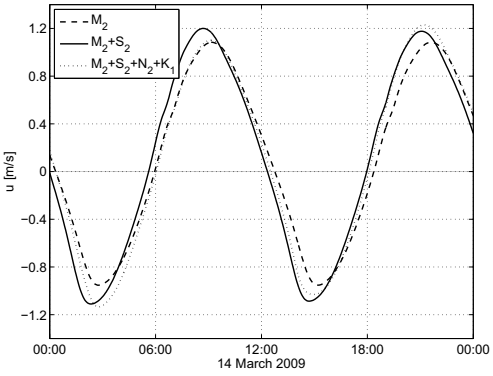

(e) P4

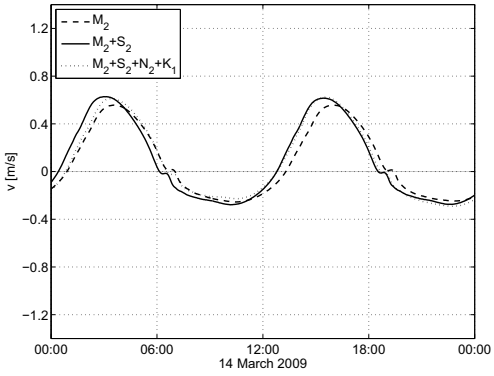

(f) P4

Figure 21: The u and v component of the depth mean current at location P2, P3 and P4 shown in Fig. 15. East is positive direction for u and north is positive direction for v.

Paper IV

Numerical studies of dispersion due to tidal flow through Moskstraumen, northern Norway